Loop Formation and Contact Problems in Elastic Rods

Ridouan Chaouki

A thesis submitted in partial fulfillment of the

requirements of London South Bank University

for the degree of Doctor of Philosophy

April 2019

School of Engineering

London South Bank University

Abstract

This thesis examines two problems involving the equilibrium configurations of intrinsically straight and intrinsically curved, long elastic rods. In both cases the rod is in a planar configuration and is clamped at one end and has a load applied at its free end. The first problem concerns intrinsically curved rods, which undergo very large deformations such that they may be pulled nearly straight, or may form a loop, or are bent in such a way that their curvature is of the opposite sign to their intrinsic curvature. Using a combination of experiments, numerical simulations and analysis, the aforementioned configurations are considered from a global qualitative perspective. The thesis gives the critical conditions for loop formation and critical points at which a rod may jump from one configuration to another. The second problem examines the equilibrium configurations of an intrinsically straight rod that is pressed against an inclined wall. The critical point at which tip contact changes to line contact is given, where we again find excellent correlation between experiments, numerics and analysis. Overall, the thesis contributes to our understanding of the mechanics of rods with applications in a variety of real world scenarios - from structural design, to cable laying problems, and the mechanics of animal vibrissae.

Contents

List of Figures

List of Tables

Acknowledgements

First and foremost I would like to thank my supervisor Dr. G. Goss for his continual advice, criticism and patience. I have always looked forward to our meetings with enthusiasm. Secondly I thank Dr. P. Singh in the same way - I have benefited greatly from our discussions. Also thanks goes to Prof. T. Sattar, Prof. M. Tokhi, Dr. O. Oumar, Dr A. Rasheed, Dr. A. Paspali, and the technicians: P. Elsdon, K. Bellingham, M. Zahir and G. Bird. I must also thank my parents, brothers and sisters for their patience.

Nomenclature

symbol	definition	units	nondimensional symbol
α	Angle of inclined force	radians	
B	Flexural rigidity	Nm^2	
B_p	Length of contact region	m	b
D	End displacement of rod	m	d
E	Complete elliptic integral of the second kind		
$\mathbf{i}$, $\mathbf{j}$, $\mathbf{k}$	Basis for Coordinate system		
Γ	Curvature	m^{-1}	κ
K	Complete elliptic integral of the first kind.		
L	Length of rod	m	l
M	Bending moment	Nm	m
N	Normal force	N	n
p	Elliptic modulus		
F	Resultant force	N	f
S	Arc length	m	s
T	Axial load	N	t
ϕ	Slope of deformed rod	radians	

Chapter 1

Introduction

The problem of an intrinsically straight rod whose ends are clamped and free (clamp-free) with a compressive load applied at the latter end, has a long history. It was solved by Leonhard Euler in the eighteenth-century, see [1], [2], [3] and [4]. The solution i.e., the equations denoting the force and coordinates are well-known and readily available, see for example the books [5] and [6]. In his paper Euler [7] solved the problem using a power series.

A plethora of research is available on large planar deformation of rods. Some of this is purely theoretical and some is applied. However, there is a marked absence of experimental research. This thesis examines the large deflections of clamped-free rods that either have large intrinsic constant curvature or straight in their unstressed state. Our work encompasses experiments, numerics and analysis. The two main platforms for comparing results of these are equilibrium loading diagrams and deformed shapes.

In the first part of this thesis, we report on the large deflections of clamped-free rods that have intrinsic constant curvature in their unstressed state. The rods are deformed by displacing the tip of the free end or applying load at the free end. Those types of loading procedures are known as rigid and dead loading respectively [8]. Theoretical studies on rods that have small values of intrinsic constant curvature have been examined before in [6], [9], [10], [11], [12] and [13].

The second problem in this thesis reports on the large deflections of an initially straight rod that has a flat, rigid plate pressed against its tip. This problem was inspired by whiskers/vibrissae and can be applied in the field of robotics. Robots and autonomous vehicles that operate in harsh and/or opaque conditions require sensor input to make decisions. In such environmental conditions, traditional sensors may not be useful. To provide an alternative, researchers are inspired by the animal world to develop contact sensors. Researchers have developed mathematical models to try and simulate the forces and bending moments acting at the base of whiskers. Generally, two kinds of mathematical models are used to analyse the mechanical response of whiskers. Those models are rigid body models and continuum models. In rigid body models, the whisker is represented as a series of rigid bodies that are connected to one another by springs [14], [15] and [16]. In continuum models the whisker is represented as one flexible element [17], [18] and [19]. The elastica (a nonlinear model) and beam theory (a linear model) are examples of the latter.

1.1 Contribution to knowledge

In chapter 3 of this thesis we report on the large deflections of intrinsically, constantly curved rods that are either deformed in a rigid or dead loading manner. The contributions of this work in the area are given below.

1. We found that upon loading an intrinsically, uniformly curved clamped-free rod (in a rigid loading manner), loop formation can occur. Loop formation occurs at critical values of intrinsic curvature. Those values are found experimentally, and then verified numerically and analytically. We use the planar theory and find a good match with the experiments. This work is also reported in our paper, see [20].

2. In addition to verifying the previous [6] and [10] we found that there are solutions that are always inflectional. The experimental loading paths (obtained under dead loading) are compared with the numerical and analytical results. Furthermore, we report on critical (instability) points that occur during those experiments. The critical points that we find mathematically are in good agreement with the numerics and experiments. The work we have described, i.e., inflectional solutions and the critical unstable points, are previously unreported and a journal publication is in preparation.

In chapter 4 the loading paths and deformed shapes of an initially straight rod that has a plate pressed at the tip are computed. This work has applications in biomimetics and robotics. Previously published work have focused on linear theory and have not considered point and line contact, i.e., situations whereby the rods tip is in contact and a section of the rods length is in contact, respectively. This work has also been published in our paper, see [21].

1.2 Overview of the thesis

The structure of this thesis is outlined below:

1. In chapter 2 we formulate the mathematical model. The model reflects the experimental set-up and procedure as closely as possible. First, we give a derivation of the model and this is broken down into three parts, namely: the geometry of deformation, the fundamental mechanical laws and the constitutive equation. We then describe the loading procedure and the boundary condition at one end of the rod from an experimental point of view. In the penultimate section we describe the numerical technique that is adopted in the computer software AUTO, and in the last section we give the equations along with the boundary conditions in non-dimensional form.

   We also describe the experimental set-up, experimental procedure and the numerical technique that is used by the software AUTO.

2. In chapter 3 we report on the large deflections of uniformly curved rods. This chapter is split into the following two sections:

   - In §3.3 we report on uniformly curved rods that are deformed under rigid loading. Upon loading, the curvature in the rod is always the same sign as the intrinsic curvature. These configurations can be inflectional and noninflectional. In §3.3.1 we examine the conditions for loop formation.

   - In §3.4 we examine rods that have an interior inflectional point, i.e., inflectional type rods. We present the experimental, numerical and analytical solutions, and then in §3.4.1 we compute the points that are associated with instability.

3. In chapter 4 we give solutions to a rod that has a rigid, frictionless plate pressed at the free end.

4. In chapter 5 we give a conclusion on our findings and discuss future research.

Note, we conduct a literature survey in the introduction sections of chapters $2, 3$ and 4.

Chapter 2

Mathematical model & methodologies

2.1 Introduction

The purpose of this chapter is to present the mathematical model that governs the planar deformation of slender, inextensible and unshearable rods. We apply the model, a boundary value problem (BVP) to physical rods of circular and rectangular cross sections. The model encompasses the planar deformation of nitinol rods which are either uniformly curved or straight in their reference configuration. The model consists of a system of first order ordinary differential equations (ODEs) and boundary conditions. These are then solved using either numerical computation (computer software: AUTO) or analysis and then compared to data obtained from experiments.

A plethora of literature has appeared over the last thirty years with respect to the large deflection in rods. Some of the earliest work has been purely analytical [6], [11], [22] while some of the more recent work has relied upon numerical computation [13], [23], [24]. Experimental studies on the other hand have not received the same magnitude of attention.

One of the earliest experimental studies on large deflection rod theory was conducted in [25]. Although the equations were known as early as the eighteenth-century, the deformed shapes had not been experimentally determined until the author presented their PhD thesis [25]. The author performed experiments on rods of rectangular cross-sections (strips) and considered the clamped-clamped, clamped-pinned and clamped-free boundary conditions. The author discovered that a rod that was clamped at both ends was always stable when no inflection points exist (non-inflectional), where in contrast a rod with the same boundary conditions that has inflection points (inflectional), tends to buckle out of the plane. The author used rods of rectangular dimensions in the experiments (of dimensions: 0.5mm and 0.25mm). The author remarked that "these strips clearly behave as planar rods".

The author of [4] obtained experimental data and compared the data with analysis and numerical computation. In the experiments the author used rods that have both rectangular and circular cross-sections. The author used the three-dimensional rod model and determined an analytical expression for the out of plane bifurcation that develops in the clamped-clamped rod [26]. The author also, in [4] conducted experiments whereby twist was varied, and this led to writhing and loop formation in rods.

The experimental work by the authors in [25] and [4] was accomplished by varying the end load and end displacement respectively. We should also add that neither [4] nor [25] consider naturally curved rods or any external constraints. In our work, we perform experiments on rods that are deformed in a rigid and dead loading manner. Note, that for our experiments we follow the experimental procedure in [4]. Deforming a rod and obtaining solutions in an experiment may not always give the full account to the solution. For example the paper by the author of [27] presented the loading path of a clamped-pinned rod. The author reports that solutions that are obtained under a dead load become unstable. The loading diagram that is obtained under this type of loading (dead loading) has a different loading diagram to the case where the same rod is deformed under rigid load. If one is concerned with the stability of such structures, then the loading procedure of the rod becomes important, see [8].

Experiments are a major theme in this work and one of the challenges in performing useful experiments is to find a material which is "rod-like" (elastic) over a sufficiently large range of (measurable) loads. Real physical rods can kink i.e., they have a finite 'elastic domain' and when that domain is exceeded they undergo plastic deformation. However, successful experiments have been undertaken using nickel titanium alloy rods in [4], which, as discussed in Section 2.4.1, is the material selected for our experiments.

2.2 The geometry of deformation

A rod is a slender elastic structure that has the distinctive property whereby one dimension i.e., the length L, is much greater than the other two. We make use of this property and parameterise the rod by a single variable: the arc length S, where $S \in [0, L]$. The experimental rig, along with an unstressed (straight)

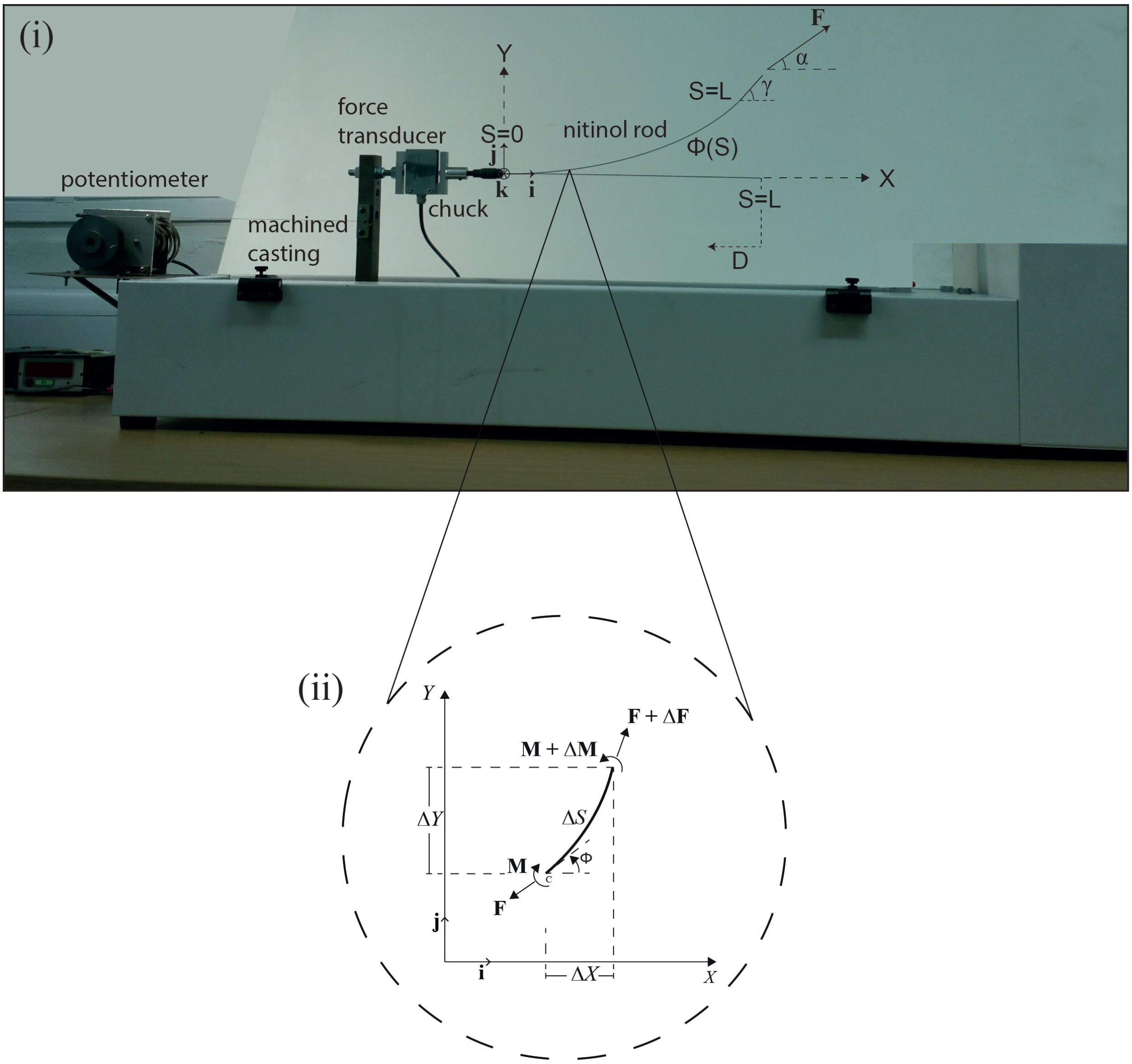

Figure 2.1: (i)The experimental rig with a rod of length L deflected under input of end displacement D. In its unstressed reference state the rod lies along the X axis. (ii) A free body diagram of an element ΔS of deformed rod.

and deformed nitinol rod is presented in Figure 2.1(i). We define a right-handed orthonormal cartesian co-ordinate system X, Y, Z with basis $\{\mathbf{i}, \mathbf{j}, \mathbf{k}\}$ and place it at $S = 0$. The unstressed rod lies in XY plane and upon deformation the rod remains in that plane. The deformed rod is described by $\phi(S)$, the angle between the horizontal X-axis and the tangent to the deformed rod at S. The angle $\phi(S)$ is measured anti-clockwise from that axis and this is defined to be positive. The Cartesian coordinates X, Y at a point S are recovered from the following differential equations:

$$\frac{\mathrm{d}X}{\mathrm{d}S} = \cos(\phi), \tag{2.1}$$

$$\frac{\mathrm{d}Y}{\mathrm{d}S} = \sin(\phi). \tag{2.2}$$

In the case of the unstressed straight rod (zero intrinsic curvature), the rod lies along the X axis such that $S(L) = X(L)$.

The curvature of the rod Γ, is defined as:

$$\frac{\mathrm{d}\phi}{\mathrm{d}S} = \Gamma. \tag{2.3}$$

2.3 Equilibrium of forces and moments

A force $\boldsymbol{F}$ is exerted on the rod at the tip (or $S = L$) and is applied at an angle α. The angle, α is measured from the X axis in the anti-clockwise direction and this is defined to be positive, see Figure 2.1(i). Note, that we neglect the self-weight of the the rod. The force $\boldsymbol{F}$ acts in the XY plane, and the bending moment $\boldsymbol{M}$ acts about an axis normal to that plane, i.e., the Z-axis. The force is represented in terms of its components $T\mathbf{i}$ and $N\mathbf{j}$, an axial and normal force respectively. We refer to [1] and take the summation of moments about the point 'C' as follows:

$$\sum \boldsymbol{M}_c = \boldsymbol{0}, \tag{2.4}$$

$$\boldsymbol{M} + \Delta\boldsymbol{M} + \Delta\boldsymbol{R} \times (\boldsymbol{F} + \Delta\boldsymbol{F}) - \boldsymbol{M} = \boldsymbol{0}, \tag{2.5}$$

where"$\times$" denotes a vector (cross) product and where,

$$\Delta\boldsymbol{R} = \Delta X\mathbf{i} + \Delta Y\mathbf{j}, \tag{2.6}$$

and

$$\boldsymbol{F} = T\mathbf{i} + N\mathbf{j}, \quad \Delta\boldsymbol{F} = \Delta T\mathbf{i} + \Delta N\mathbf{j}. \tag{2.7}$$

Internal moments $\boldsymbol{M}$, act in the anti-clockwise direction and are defined to be positive. We substitute Eqs. 2.7 and 2.6 into Eq. 2.5, and ignore terms of $\mathcal{O}(\Delta^2)$,

$$\Delta\boldsymbol{M} + (\Delta X\mathbf{i} + \Delta Y\mathbf{j}) \times (T\mathbf{i} + N\mathbf{j}) = \boldsymbol{0}, \tag{2.8}$$

$$\Delta M\mathbf{k} - T\Delta Y\mathbf{k} + N\Delta X\mathbf{k} = 0\mathbf{k}. \tag{2.9}$$

For any static equilibrium configuration the forces and moments acting on an element ΔS must be zero. Dividing Eq. 2.9 through by ΔS gives,

$$\frac{\Delta M}{\Delta S} - T\frac{\Delta Y}{\Delta S} + N\frac{\Delta X}{\Delta S} = 0, \tag{2.10}$$

and taking the limit $\Delta S \to 0$,

$$\frac{\mathrm{d}M}{\mathrm{d}S} - T\frac{\mathrm{d}Y}{\mathrm{d}S} + N\frac{\mathrm{d}X}{\mathrm{d}S} = 0. \tag{2.11}$$

Substituting Eqs. 2.1 and 2.2 into Eq. 2.11 gives,

$$\frac{\mathrm{d}M}{\mathrm{d}S} - T\sin(\phi) + N\cos(\phi) = 0. \tag{2.12}$$

Applying the condition of force equilibrium along the rod, i.e.,

$$\sum \boldsymbol{F} = \boldsymbol{0},$$

$$\boldsymbol{F} + \Delta\boldsymbol{F} - \boldsymbol{F} = \boldsymbol{0}. \tag{2.13}$$

Dividing Eq. 2.13 by ΔS gives:

$$\frac{\Delta\boldsymbol{F}}{\Delta S} = \boldsymbol{0}, \tag{2.14}$$

and taking the limit $\Delta S \to 0$,

$$\frac{\mathrm{d}\boldsymbol{F}}{\mathrm{d}S} = \boldsymbol{0}. \tag{2.15}$$

Substituting the first expression of Eq. 2.7 into Eq. 2.15 gives:

$$\frac{\mathrm{d}}{\mathrm{d}S}\left(T\mathbf{i}+N\mathbf{j}\right) = \boldsymbol{0}, \tag{2.16}$$

from which it follows:

$$\frac{\mathrm{d}T}{\mathrm{d}S} = 0, \tag{2.17}$$

$$\frac{\mathrm{d}N}{\mathrm{d}S} = 0. \tag{2.18}$$

The forces T and N are given as follows:

$$T = F\cos\left(\alpha\right), \tag{2.19}$$

$$N = F\sin\left(\alpha\right). \tag{2.20}$$

Accordingly, $T(S)$ and $N(S)$ are conserved quantities.

2.4 The constitutive relation

We seek a linear constitutive relation between the bending moment and curvature that is applicable over the range of loads used in the experiments. That constant of proportionality is the flexural rigidity B, and in the case of a linear relationship this is expressed as follows:

$$M = B\left(\frac{\mathrm{d}\phi}{\mathrm{d}S} - \Gamma_i\right), \tag{2.21}$$

where Γ_i is the initial curvature. For initially straight and uniformly curved rods, $\Gamma_i = 0$ and $\Gamma_i \neq 0$ respectively, see Figure 2.5. The constitutive relation, Eq. 2.21 links Eq. 2.12 with Eq. 2.3. We take the derivative of Eq. 2.21 with respect to S and combine it with Eq. 2.12. This leads to the governing nonlinear elastica equation:

$$B\,\frac{\mathrm{d}^2\phi}{\mathrm{d}S^2} - F\cos(\alpha)\sin(\phi) + F\sin(\alpha)\cos(\phi) = 0, \tag{2.22}$$

$$B\,\frac{\mathrm{d}^2\phi}{\mathrm{d}S^2} - F\sin(\phi-\alpha) = 0. \tag{2.23}$$

2.4.1 Flexural rigidity

We perform the experiments using nickel-titanium (nitinol) rods of circular and rectangular cross-sections of length L. Nitinol, an alloy made up from nickel and titanium (55% Ni and 45% Ti) exhibits unique material properties, namely superelasticity and shape memory effects [28]. That unique superelastic property has made it a preferred choice in biomedical applications [29]. Nitinol with shape memory properties, has the ability to undergo deformation at one temperature, and then return to the undeformed shape when heated. Nitinol with superelastic properties has the ability to deform and return to their natural state providing the elastic limit is not reached. The elasitc limit is reported as 1650MPa, see [30]. With this in mind, superelastic nitinol rods of circular (radius = 0.5mm) and rectangular cross-sections (length $\times$ width = 3mm$\times$0.25mm) are chosen. We select rods of lengths in the range $250-400$mm and assume, with good justification (as discussed below), the samples chosen are isotropic and homogeneous. We also assume that the unstressed state is straight and that during experiments the rods suffer no appreciable extension or transverse shear. Since suppliers advise that these properties may vary (due to manufacturing), we establish them directly by conducting simple cantilever experiments. From cantilever experiments we determine the value of B using the the following formula [31]:

$$\delta_n = \frac{NL^3}{3B} \tag{2.24}$$

where δ_n is the deflection at the free end due to the applied normal load N at the tip. This experiment gives the same result in any lateral direction, i.e., isotropy. The value of B is determined for both circular and rectangular cross sectional rods, see Figure 2.2(a) and (b) respectively.

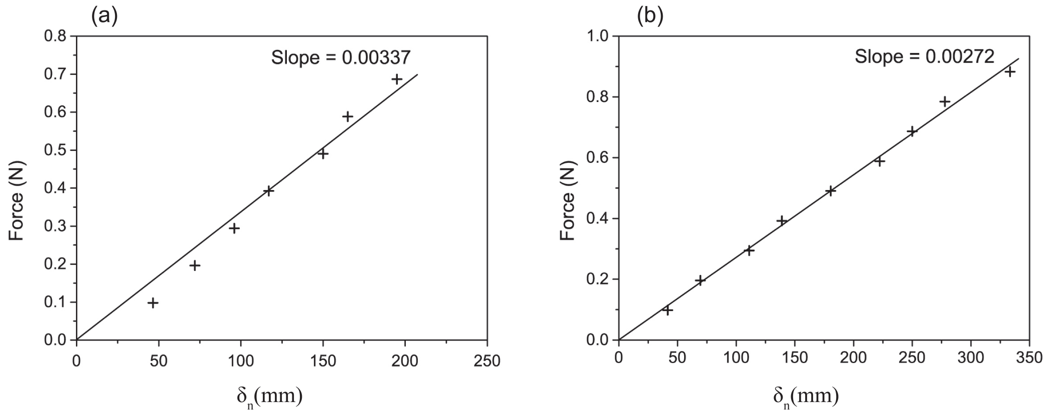

Figure 2.2: Line of best fit to experimental data for the determination of flexural rigidity B, for (a) 1mm diameter nitinol circular rod and (b) 3mm $\times$ 1mm nitinol strip.

2.4.2 Initial curvature

Rods with circular cross sections have disadvantages for experimental investigations into the effects of initial curvature because they tend to undergo out-of-plane deformations under loading, see for example [4] and [25]. Furthermore, since rods are generally supplied as intrinsically straight, initial curvature has to be induced and that is difficult with circular rods, for similar reasons. We induce constant curvature by wrapping and clamping the nitinol tightly around circular steel bars of diameters 8,12,15 and 30mm, see Figure 2.3. During that deformation the

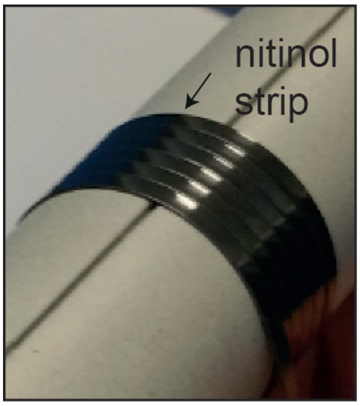

Figure 2.3: Experimental procedure for inducing intrinsic curvature

rod exceeds its elastic limit, such that when the rod is released from its clamps it adopts the form of a circle (of larger radius than the circular steel bar about which it was clamped). That new circular form becomes the natural unstressed state of the rod. In this state, there is residual stress [32] however, we assume that in any subsequent loading or unloading processes that the rod undergoes during experiments, the rod is completely elastic. We remark here that the rod has not been subjected to any heat treatment.

2.5 Experimental procedure and boundary conditions

The rig consists of a chuck, force transducer, machined casting and a potentiometer. The potentiometer and force transducer record the end displacement and force respectively and are attached to the machined casting on the rig (see the left hand side of Figure 2.1). In this section the boundary conditions, with reference to the experimental apparatus are specified.

2.5.1 Clamped-end

The boundary conditions at the clamped end are given as follows:

$$X(0) = 0, \tag{2.25}$$

$$Y(0) = 0, \tag{2.26}$$

$$\phi(0) = 0. \tag{2.27}$$

The chuck pictured in Figure 2.4 clamps the rod such that the conditions in Eqs. 2.25 – 2.27 are satisfied.

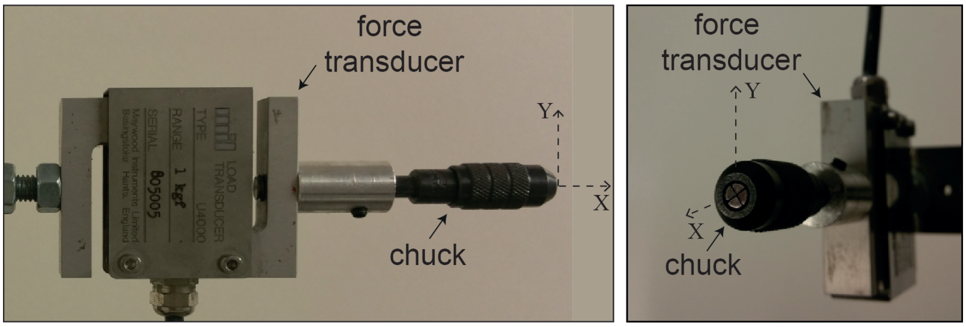

Figure 2.4: The experimental set-up at the clamped end of the rod ($S = 0$) satisfying the boundary conditions Eqs. 2.25 – 2.27. Here the rod is gripped in the in exactly the same way a drill bit is gripped.

2.5.2 Free-end

In all the problems investigated in this work, the following boundary condition holds at the tip:

$$\frac{\mathrm{d}\phi}{\mathrm{d}S}(L) = \Gamma_i. \tag{2.28}$$

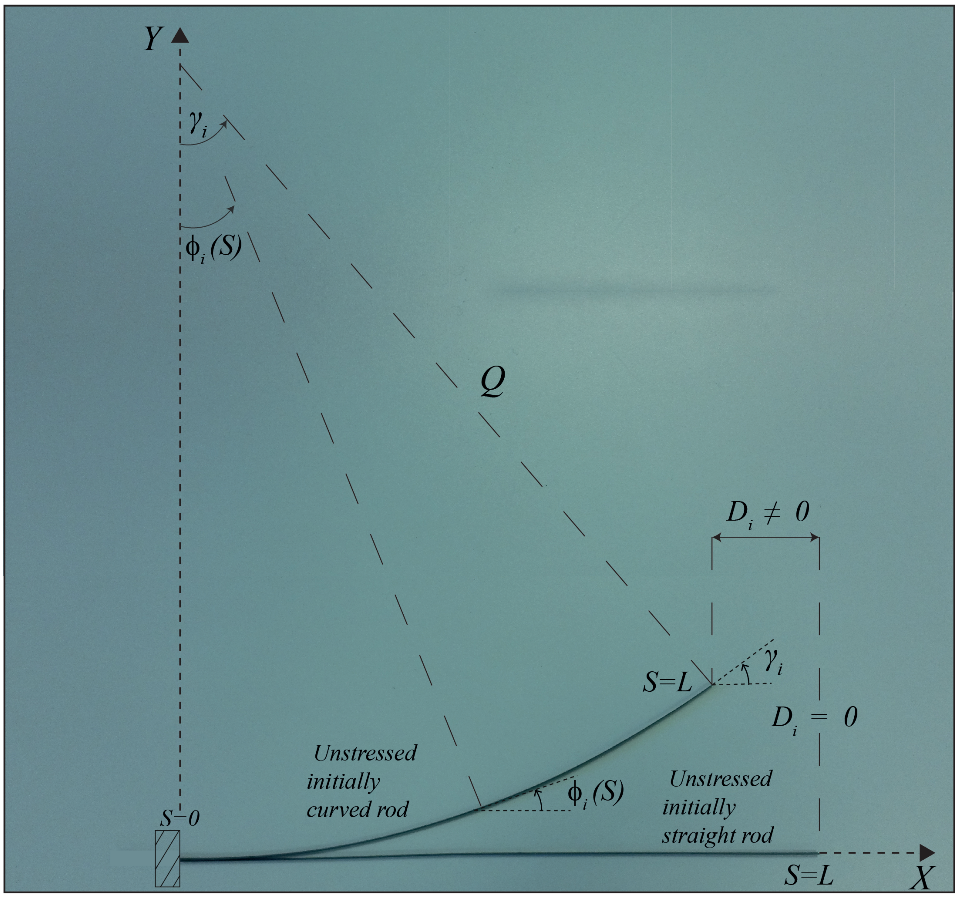

Figure 2.5: The reference states for a straight rod and a uniformly curved rod. Note the definitions of D_i; for the straight rod $D_i = 0$ and for the intrinsically curved rod $D_i \neq 0$

Experiments may proceed under two different procedures:

1. Loading the free end by a weight i.e.,

$$F(L) = \pm\Lambda. \tag{2.29}$$

   In this case, the rod is inserted in the chuck ($S = 0$) and the weights (of weight Λ) are applied at the free end ($S = L$). The weights are loaded on to the hanger (of mass 10g) and attached to the rod at $S = L$ via a wire clamp. After each incremental load is applied, we record the corresponding position $X(L)$ and determine D (from Eq. 2.30). The weights were designed and constructed from polymethyl methacrylate (acrylic) by the author and each free weight is $\approx$ 012N (1.3g), see Figure 2.6.

2. Displacement of the free end in a straight line parallel with the X axis, by amount D either away from or towards the clamped end $X(0)$. In this case we specify the following boundary condition:

$$X(L) = L - D_i \pm D. \tag{2.30}$$

The position of the tip of the unstressed straight and uniformly curved rod, D_i (see Figure 2.5) is defined respectively, as follows:

$$D_i = 0 \tag{2.31}$$

$$D_i = L\left(1 - \frac{1}{\gamma_i}\sin(\gamma_i)\right). \tag{2.32}$$

The experiment is set-up such that the transducer records values of F every $D = 0.1$mm. The force transducer facilitates the recording of both negative and positive values, i.e., a compressive and tensile force respectively. For the case of the two problems analysed in this research project, an experiment under rigid loading conditions involves attaching a clamp-slider and using a plate against the tip of the rod, see Figures 3.1 and 4.3 respectively.

Those two procedures are referred to as 'dead' and 'rigid' loading, see [8].

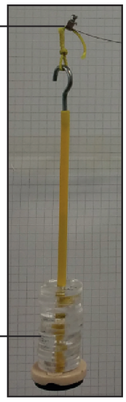

Figure 2.6: Experimental procedure for dead loading. The rod is loaded at the tip with free weights (mass of each is 1.3g).

2.6 Numerical methods

The system of ODEs Eqs. 2.1 − 2.3, Eq. 2.17, Eq 2.18 and Eq. 2.22 (or Eq. 2.23) and the corresponding boundary conditions Eqs. 2.25 − 2.29, constitute a well posed BVP. In this work our main forum for studying solutions is through equilibrium loading paths and XY deformed shapes. The equilibrium diagrams are used to compare the theory with experimental data. Experiments proceed under continuation of either F or D, as 'continuation parameters'. The solution to our BVP can be obtained by direct integration and expressed in terms of elliptic functions, see [6], [4]. However, in the case of initial curvature, there are complications that make the solutions difficult to interpret, which are discussed in §2.8.2.1. Consequently, we integrate the BVP system of ODEs directly under parameter continuation of F (dead loading) and D (rigid loading).

There are various numerical methods for achieving this. For example, the finite element (FEM) (see [33] and [34]), the shooting method (see [35]) and MATLAB's bvp4c (see [4]). FEMs employing Riks arclength continuation can also produce equilibrium paths where no bifurcation exists [36]. However MATLAB's bvp4c can struggle as it does not use the previous solutions to find new solutions and due to the nonlinearlity of the ODEs, they can struggle to compute an equilibrium loading path.

The software package AUTO [37] is based on numerical continuation. The basic aim of a continuation method is to find solutions corresponding to particular values of a defined continuation parameter, i.e., D or F for rigid or dead loading respectively. Given an initial solution, a continuation method computes the solution path by first changing the value of the parameter and then using a root finder to locate the point on the solution curve. The computation of solutions when the parameter is varied is a procedure known as numerical continuation, or path following. The most popular continuation techniques are those based on predictor-corrector schemes and AUTO-07p is an example of this. The general idea of such schemes is to follow (according to the user defined step size) follow the solution curve incrementally. Each incremental update is achieved in two steps:

- The first step generates an approximation to the solution using previous information (predictor step) and
- the second step uses this prediction as an initial guess for an iterative nonlinear solver i.e., Newton's method (the corrector step).

At turning points and bifurcation points, Newton's method fails during parameter continuation [38]. The solution to this problem is to introduce a pseudoarclength. In pseudoarclength continuation, the "ideal" parameterisation of the solution curve is its arclength. Pseudoarclength is an approximation of the arclength in the tangent space of the curve, see Figure 2.7 (a) and (b) for pseudoarclength and parameter continuation respectively. The resulting continuation, takes a step in pseudo-arclength (rather than the natural step in the parameter space). Newton's method is then used to locate the solution at that given pseudo-arclength, which requires adjoining an additional constraint (the pseudoarclength constraint), see [39].

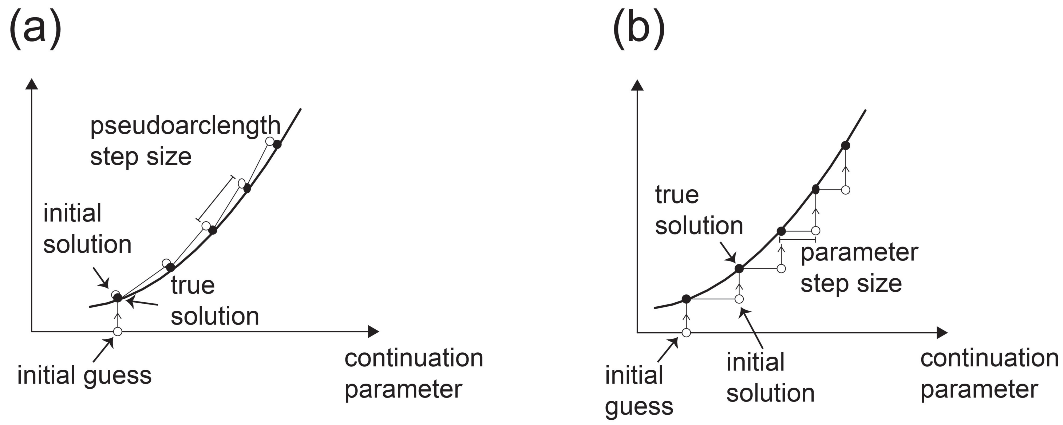

Figure 2.7: Graphical interpretation of (a) pseudo-arclength and (b) parameter continuation. In parameter continuation the solution at a particular value of the continuation parameter F or D, is used as the initial guess for the solution. If the step size is sufficiently small the iteration will converge. On the other hand, pseudo-arclength involves the step size along the arclength of the solution curve, rather than the continuation parameter.

AUTO does not rely on guess or interpolation functions and deals directly with the differential equations and boundary conditions. It computes solutions as the continuation parameter changes whereas some other numerical methods, for instance FEM rely on interpolation functions [34]. We choose to use AUTO for the following reasons:

1. AUTO explicitly identifies maximum and minimum points on the solution curve (limit points)

2. AUTO detects bifurcations i.e., the n^{th} buckling mode, where $n = 1, 2, 3, ..., \infty$.

3. AUTO computes solutions based on a continuation parameter. Additionally, it also allows the user to define further free parameters.

4. AUTO uses the solution of the previous step to find the solution of the next step. This is advantageous because it forces the program to stay on the solution curve.

We write the BVP in a text file using the computer language FORTRAN. AUTO requires the program file and a constants file. In the former, we define the equations and the boundary conditions only, and in the latter, we define, for example the number of iteration steps, parameter step size and number of free parameters. When the programme has computed the solutions to the BVP, the user can plot the deformed shape i.e., $x(s)$ and $y(s)$ and equilibrium loading diagrams.

2.7 Nondimensional system of equations

For the purpose of both experimental and numerical computation, it is convenient to re-write the equations in non-dimensional form. For this the following re-scalings are introduced:

$$s = \frac{S}{L}, \quad x = \frac{X}{L}, \quad y = \frac{Y}{L}, \quad d = \frac{D}{L}, \quad q = \frac{Q}{L}, \quad \kappa = \Gamma L, \tag{2.33}$$

$$t = \frac{TL^2}{EI}, \quad \lambda = \frac{\Lambda L^2}{EI}, \quad n = \frac{NL^2}{EI}, \quad f = \frac{FL^2}{EI}, \quad m = \frac{ML}{EI}. \tag{2.34}$$

2.7.1 Nondimensional system of first order ordinary differential equations & boundary conditions

The mathematical model consists of five first order ODEs. These are Eqs. 2.1−2.3 for the deformation of the geometry, Eqs. 2.17 and 2.18 for the force, along with Eq. 2.22 (or 2.23) for the curvature. In nondimensional form those are as follows:

$$\frac{\mathrm{d}x}{\mathrm{d}s} = \cos(\phi), \tag{2.35}$$

$$\frac{\mathrm{d}y}{\mathrm{d}s} = \sin(\phi), \tag{2.36}$$

$$\frac{\mathrm{d}\phi}{\mathrm{d}s} = \kappa, \tag{2.37}$$

$$\frac{\mathrm{d}\kappa}{\mathrm{d}s} = f\sin(\phi-\alpha), \tag{2.38}$$

$$\frac{\mathrm{d}f}{\mathrm{d}s} = 0. \tag{2.39}$$

The boundary conditions for this BVP are given in Eq. 2.25−2.27 at the clamped end, and Eq. 2.28 along with either Eq. 2.29 or Eq. 2.30 for dead and rigid loading respectively. The nondimensional boundary conditions are summarised in Table 2.1.

Boundary Conditions	
Clamped end:	
(1)	$x(0) = 0,$
(2)	$y(0) = 0,$
(3)	$\phi(0) = 0.$
Free end:	
(4)	$\mathrm{d}\phi/\mathrm{d}s(1) = \gamma_i.$
(5a)	$f(1) = \pm\lambda$
(5b)	$x(1) = 1 - d_i \pm d,$

Table 2.1: The nondimensional boundary conditions.

2.8 Analytical methods: some remarks

In this section we present the analytical solution for a straight rod that is deformed with a compressive axial force, i.e., $f = -t$ and $\alpha = 0$, [6]. We also present some preliminary analytical results for the case of an intrinsically, uniformly curved rod that is deformed with an axial force i.e., $f = \pm t$ and $\alpha = 0$. We then define the elliptic parameter for those cases (intrinsically straight and uniformly curved rod). The elliptic parameter plays a key role in distinguishing noninflectional and inflectional configurations.

2.8.1 Straight rod

An initially straight rod that is clamped at $s = 0$ and free at $s = 1$ is deformed with an axial compressive load (applied at the free end), see Figure 2.8. We refer back to Eqs. 2.37 − 2.38 and consider $\sin(\phi) \approx \phi$, $f = -t$ and $\alpha = 0$.

$$\frac{\mathrm{d}^2\phi}{\mathrm{d}s} + t\phi = 0. \tag{2.40}$$

The general solution to Eq. 2.40 is of the form:

$$\phi(s) = A \sin\left((t)^{1/2}\, s\right) + B \cos\left((t)^{1/2}\, s\right). \tag{2.41}$$

From boundary conditions (3) and (5), see Table 2.1, we find $B = 0$ and

$$\frac{\mathrm{d}\phi}{\mathrm{d}s}(1) = A t^{1/2} \cos\left((t)^{1/2}\right) = \gamma_i. \tag{2.42}$$

For the initially straight rod $\gamma_i = 0$ and it follows that Eq. 2.42 is satisfied at the following values of t:

$$(t)^{1/2} = (1+n)\,\frac{\pi}{2}, \qquad n = 0, 1, 2, 3, ..., \infty, \tag{2.43}$$

where $n = 0$ corresponds to the Euler buckling load and $n = 1, 2, 3, ..., \infty$ correspond to the existence of multiple buckling loads, see [4]. The general solution to Eq. 2.40 is of the form:

$$\phi(s) = A \sin\left((t)^{1/2}\, s\right). \tag{2.44}$$

We denote the Euler buckling load t_E as follows:

$$t_E = \frac{\pi^2}{4}. \tag{2.45}$$

Eq. 2.45 describes a change of state whereby the straight rod buckles and this was given by Euler (1707-1783), see [7]. This result is the first example of a formula depicting a *bifurcation* in a structural system. The term bifurcation comes from the Latin *furca*, to fork, and describes the loss of stability of one state and the emergence of two new stable states. The existence of two solutions illustrates the fact that at the critical load the rod can buckle to either side, see Figure 2.8 where the rod can either buckle into what we call the *upper* or the *lower half-plane*, UHP and LHP respectively. In the case of an initally straight rod, the UHP and LHP correspond to $\phi(s) > 0$ and $\phi(s) < 0$ respectively, and it follows that such solutions can be obtained by taking the positive or negative sign in Eq. 2.48 (or Eq. 2.48). Experimentally, the plane that the rod chooses to deflect in cannot be determined but will depend in practise on the presence of an imperfection of which initial curvature is an example.

The solution of a rod that is deformed under an axial load only, i.e., $\alpha = 0$ under large deflections is presented. Note that the equations we present are for a rod that is straight in its unstressed state i.e., $d_i = 0$, see [5]. We re-write Eqs. 2.37 and 2.38 in the form of a second order ODE,

$$\frac{\mathrm{d}^2\phi}{\mathrm{d}s^2} = t\sin(\phi). \tag{2.46}$$

We multiply Eq. 2.46 by $\frac{\mathrm{d}\phi}{\mathrm{d}s}$ and integrate as follows:

$$\frac{1}{2}\left(\frac{\mathrm{d}\phi}{\mathrm{d}s}\right)^2 = -t\cos(\phi) + C. \tag{2.47}$$

The constant of integration C is determined from condition 4 in Table 2.1. In the case of a straight rod the curvature is expressed as follows:

$$\begin{aligned}\frac{\mathrm{d}\phi}{\mathrm{d}s} &= \pm\left(2\,(-t)\left(\cos(\phi) - \cos(\gamma)\right)\right)^{1/2}, \\ &= \pm 2\,(-t)^{1/2}\left(\sin^2\left(\frac{\gamma}{2}\right) - \sin^2\left(\frac{\phi}{2}\right)\right)^{1/2}, \end{aligned} \tag{2.48}$$

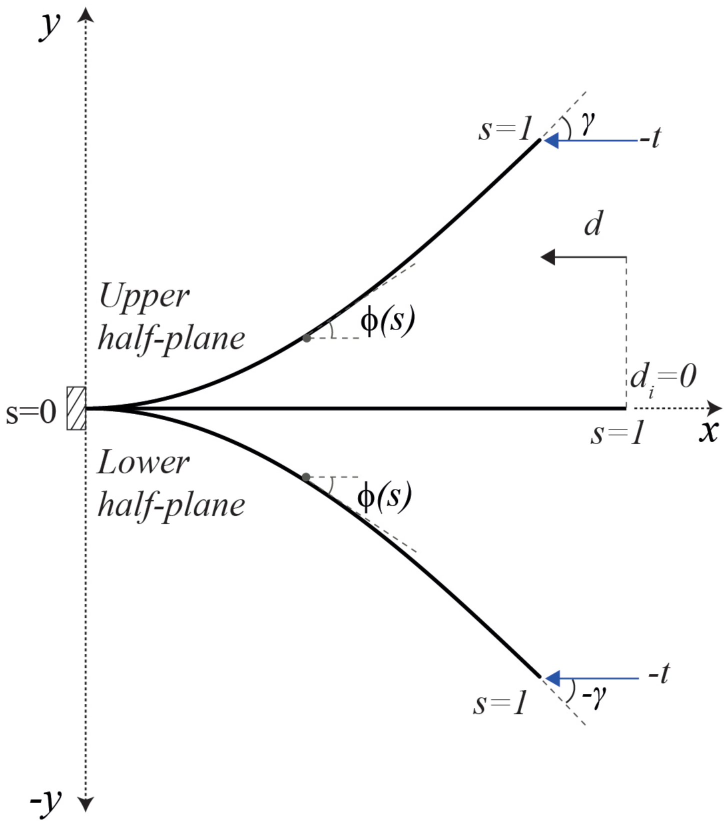

Figure 2.8: The configuration of a deformed rod in nondimensional coordinates, where the angles $\phi(s)$ and γ are measured anticlockwise from the horizontal axis at s and $s = 1$ respectively. An intrinsically straight rod will buckle at $f = t_E$ in either the UHP or LHP. In each case the configurations are symmetric about the x axis. Note that this symmetry does not apply to the initially curved rod, which we assume lies in the UHP in its unstressed state.

where $\cos(\phi) \equiv 1 - 2\sin^2(\frac{\phi}{2})$ and $-t$ refers to the magnitude of the force along the negative $\mathbf{i}$ direction. We drop the negative sign from Eq. 2.48 and split the equation as follows:

$$\int_0^s \mathrm{d}u = \frac{1}{2\,(-t)^{1/2}} \int_0^{\phi} \frac{\mathrm{d}\psi}{\left(\sin^2\left(\frac{\gamma}{2}\right) - \sin^2\left(\frac{\psi}{2}\right)\right)^{1/2}}. \tag{2.49}$$

The integral is simplified by introducing a new integration variable θ, given by

$$\theta = \arcsin\left(\frac{\sin\left(\frac{\psi}{2}\right)}{p}\right). \tag{2.50}$$

The elliptic modulus p is defined as follows:

$$p \quad = \quad \sin\left(\frac{\gamma}{2}\right). \tag{2.51}$$

It follows that the elliptic parameter, p^2 is defined in the range $0 \leq p^2 \leq 1$.

We differentiate Eq. 2.50 and obtain:

$$\mathrm{d}\psi = \mathrm{d}\theta \frac{2p\cos(\theta)}{(1 - p^2\sin^2(\theta))^{1/2}}. \tag{2.52}$$

We express Eq. 2.49 as follows:

$$s \quad = \quad \frac{1}{(-t)^{1/2}} \int_0^{\theta_\phi} \frac{\mathrm{d}\theta}{(1 - p^2\sin^2\theta)^{1/2}}, \tag{2.53}$$

The elliptic argument θ_ϕ is given by,

$$\theta_\phi \quad = \quad \arcsin\left(\frac{\sin\left(\frac{\phi}{2}\right)}{p}\right). \tag{2.54}$$

At the tip of the rod ($s = 1$), the angle is $\phi = \gamma$ and it follows that $\theta_\phi = \pi/2$. Therefore, we express Eq. 2.53 as follows:

$$1 \quad = \quad \frac{1}{(-t)^{1/2}} K\left(p\right), \tag{2.55}$$

where K is the complete elliptic integral of the first kind and is a function of p only. We determine values of t as follows:

$$t \quad = \quad -\left(K\left(p\right)\right)^2, \tag{2.56}$$

The equations for $x(s)$ and $y(s)$ are obtained by substituting Eq. 2.49 into Eqs. 2.35 and 2.36. We make use of the trigonometric identities, $\cos(\phi) \equiv 1 - 2\sin^2\left(\frac{\phi}{2}\right)$ and $\sin(\phi) \equiv 2\sin\left(\frac{\phi}{2}\right)\cos\left(\frac{\phi}{2}\right)$ and express the coordinates of the deformed rod as follows:

$$
\begin{aligned}
x(s) &= \frac{1}{(-t)^{1/2}} \int_0^{\theta_\phi} \frac{\mathrm{d}\theta}{\left(1-p^2\sin^2(\theta)\right)^{1/2}} \left(2\left(1-p^2\sin^2(\theta)\right)-1\right) \;, & (2.57)\\
x(1) &= \frac{1}{(-t)^{1/2}} \left(2E(p)-K(p)\right), & (2.58)\\
y(s) &= \frac{1}{(-t)^{1/2}} \int_0^{\theta_\phi} 2p\sin(\theta)\;\mathrm{d}\theta = \frac{2p}{(-t)^{1/2}} \left(1-\cos\left(\theta_\phi\right),\right) & (2.59)\\
y(1) &= \frac{2p}{(-t)^{1/2}}. & (2.60)
\end{aligned}
$$

Where $E(p)$ is the complete elliptic integral of the second kind. Eqs. 2.58 and 2.56 are used to compute td equilibrium diagrams, and Eqs. 2.57 and 2.59 are needed to compute the deformed shapes.

2.8.2 Intrinsically curved rod

The deformed shapes that correspond to large deflections in the UHP and LHP are depicted in Figure 2.9. We refer back to Eqs. 2.37 – 2.38, along with $\alpha = 0$ and it follows:

$$\frac{\mathrm{d}^2\phi}{\mathrm{d}s^2} = t\sin(\phi). \tag{2.61}$$

The force $f = t$ and corresponds to a compressive and tensile force, that is $t < 0$ and $t > 0$ respectively. We multiply Eq. 2.61 by $\frac{\mathrm{d}\phi}{\mathrm{d}s}$ and integrate as follows:

$$\frac{1}{2}\left(\frac{\mathrm{d}\phi}{\mathrm{d}s}\right)^2 = -t\cos(\phi) + \mathrm{C}. \tag{2.62}$$

The constant of integration C is determined by substituting condition 5 from Table 2.1,

$$\mathrm{C} = \frac{1}{2}\gamma_i^2 + t\cos(\gamma), \tag{2.63}$$

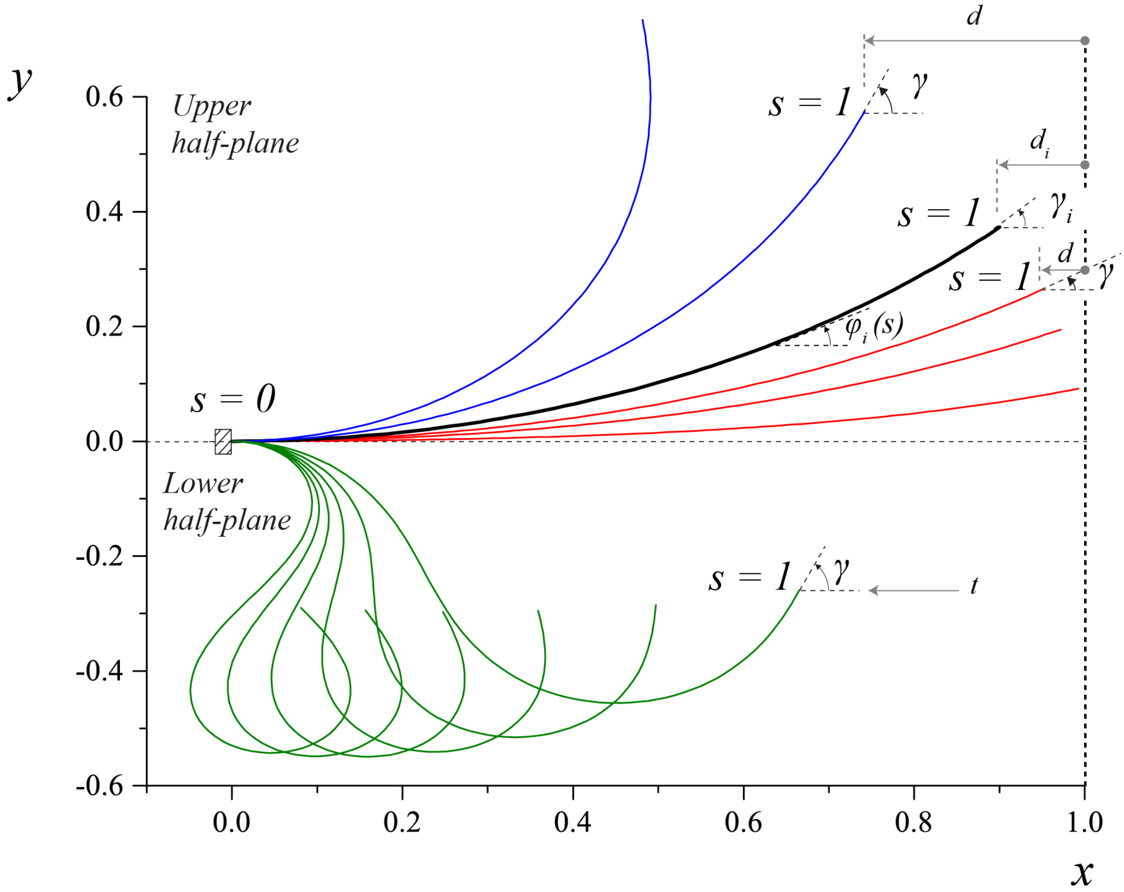

Figure 2.9: An unstressed, uniformly curved rod (shown in black) along with a rod that is held with a tensile ($t > 0$, deformed red shapes) and compressive ($t < 0$, deformed blue shapes) force in the UHP. The shapes in the LHP are shown in green and have at least one inflection point. Note that d is measured from the point $x = 1$ and for uniformly curved rods the position of the unstressed rod d_i is always > 0.

where γ_i and γ are the end angles of the unstressed and deformed rod respectively, see Figure 2.10. We substitute Eq. 2.63 into Eq. 2.62, and find:

$$\begin{aligned} \frac{\mathrm{d}\phi}{\mathrm{d}s} &= \pm\left(\gamma_i^2 - 2t\left(\cos\left(\phi\right) - \cos\left(\gamma\right)\right)\right)^{1/2}, \\ &= \pm\left(\gamma_i^2 - 4t\left(\sin^2\left(\frac{\gamma}{2}\right) - \sin^2\left(\frac{\phi}{2}\right)\right)\right)^{1/2}. \end{aligned} \tag{2.64}$$

The deformed shapes in the LHP have interior inflection points, see shapes shown in green in Figure 2.9, where the curvature along s changes sign. The deformed shapes in the UHP do not have any interior inflection points, see shapes shown in blue (for a rod deformed under a compressive force) and red (for a rod deformed under a tensile force) in Figure 2.9.

Deformed shapes in the UHP involve positive ϕ and it follows that $\frac{d\phi}{ds}$ is also positive in that plane for all the types of loading considered here viz., end displacement by d and dead loading with t. Consequently, we take the $+ve$ sign in Eq. 2.64 (or Eq. 2.64) for solutions in the UHP. However, solutions in the LHP can only be obtained by applying a clockwise moment. As that clockwise moment increases in magnitude, at some point the moment will cancel the intrinsic curvature, in which case the rod is aligned with the x axis. Upon further bending the rod deforms into the LHP such that the curvature changes sign i.e., there is an interior inflection point. Consequently, for solutions in the LHP we need to consider both $+ve$ and $-ve$ signs in Eqs 2.64 (or Eq. 2.64). In the case where $\gamma_i = 0$, i.e., the straight rod, the $+ve$ and $-ve$ signs yield solutions that are symmetric, see Figure 2.8. Similarly, in the case of uniformly curved rods there exist solutions that lie in both the UHP and LHP, however the deformed shapes in those planes are not symmetric.

We have noted that in the case of the straight rod solutions are symmetric about the x axis and whether we take the $+ve$ or $-ve$ sign in Eq. 2.64 (or Eq. 2.64) is irrelevant i.e. we just define curvature as $+ve$ or $-ve$ respectively. However, in the case of an initially curved rod, as mentioned above, that symmetry is lost and the differences are manifest in the sign of Eq. 2.64 (or Eq. 2.64). In this section we consider both cases and determine expressions for the elliptic parameter, which is a key parameter for defining solutions [6].

2.8.2.1 Case I: UHP

A nondimensional, unstressed, uniformly curved rod that is defined in the UHP is presented in black in Figure 2.10. The deformed rods, shown in blue and red correspond to $t < 0$ and $t > 0$ respectively. The curvature along the length of the rod does not change sign. Thus, we refer back to Eq. 2.64 and take the positive root:

$$\frac{\mathrm{d}\phi}{\mathrm{d}s} = \left(\gamma_i^2 + 4t\sin^2\left(\frac{\phi}{2}\right) - 4tk^2\right)^{1/2}, \tag{2.65}$$

where:

$$k^2 = \sin^2\left(\frac{\gamma}{2}\right). \tag{2.66}$$

We refer back to Eq. 2.65 and define the elliptic parameter p^2 as:

$$p^2 = k^2 - \frac{\gamma_i^2}{4t}. \tag{2.67}$$

Eq. 2.67 consists of two terms: k^2, which depends on the end angle and a term that depends on the ratio of the initial curvature, γ_i and applied force, t.

For inflectional deformed shapes, $\frac{\mathrm{d}\phi}{\mathrm{d}s} = 0$. Applying this condition in Eq. 2.65 we find that:

$$\sin^2\left(\frac{\phi}{2}\right) = p^2. \tag{2.68}$$

In order to satisfy Eq. 2.68, the elliptic parameter must take values in the following domain:

$$0 \leq p^2 \leq 1. \tag{2.69}$$

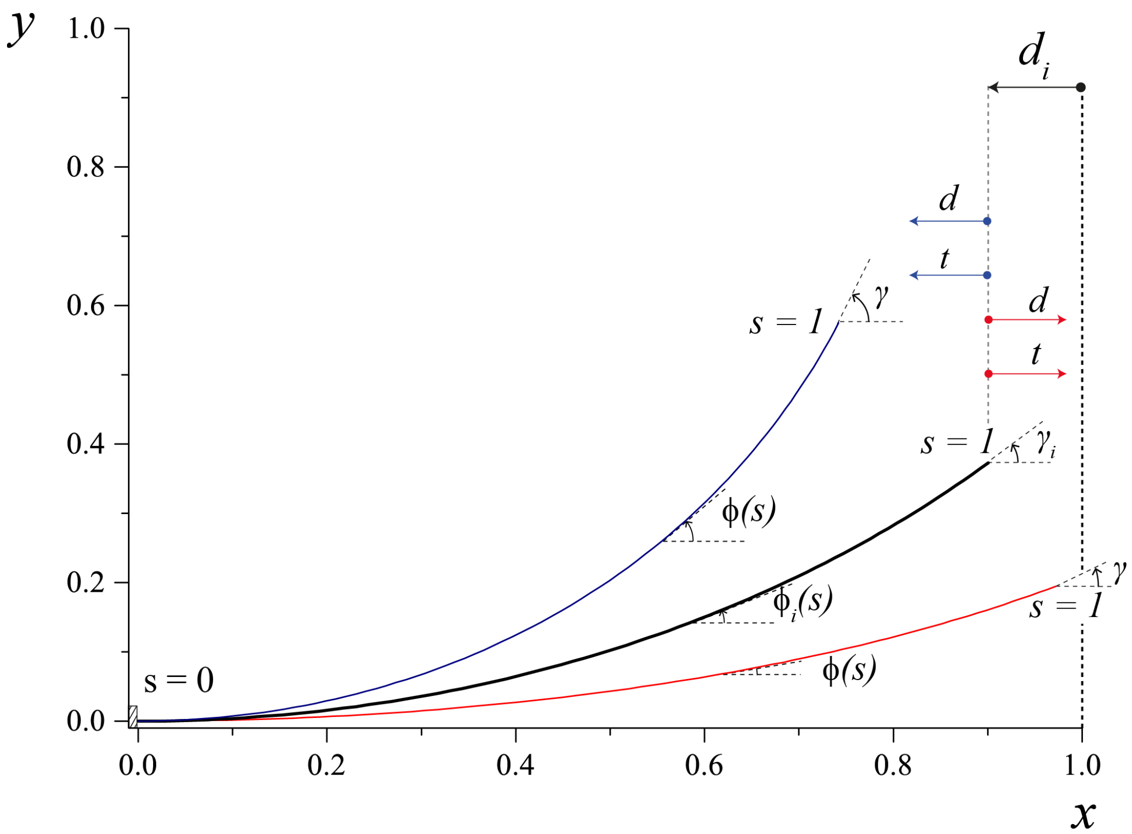

Figure 2.10: Nondimensional plot of an initially curved rod showing two configurations from its unstressed state (black curve) with initial x deflection d_i. The compressed configuration (blue) is obtained by inputting d towards the clamped end and the configuration under tension (red) is obtained by inputting d away from the clamped end.

Values of p^2 that satisfy Eq. 2.69 correspond to deformed shapes that have inflection points. Deformed shapes with no inflection points, i.e., $\frac{\mathrm{d}\phi}{\mathrm{d}s} \neq 0$, have either:

$$\begin{aligned} p^2 &> 1, \\ p^2 &< 0. \end{aligned} \tag{2.70}$$

Eq. 2.67 depends on the values of k^2 and $\frac{\gamma_i}{4t}$. In the case of an initially straight rod where $\gamma_i = 0$, the elliptic parameter is defined as $p^2 = k^2 = \sin^2\left(\frac{\gamma}{2}\right)$ (see Eq. 2.67). In that case, the elliptic parameter depends on the end angle only and consequently yields values between 0 and 1. For the uniformly curved rod in the UHP where $\gamma_i > 0$ the elliptic parameter outputs values in the ranges specified in Eqns. 2.69 and 2.70. The value of the modulus of the force $|t|$, appearing in the denominator of the latter term in Eq. 2.67 is problematic because for an infinitesimal force, $p^2 = \pm\infty$. Also, certain values of k^2 and γ_i could cause the value of p^2 to fluctuate between the ranges stated in Eqns. 2.69 and 2.70. We conclude that the solutions in terms of elliptic integrals for deformed rods in this plane are not efficient. However, we should state that the solutions are not difficult to attain and the reader is referred to the appendix of our paper, [20] where we give those. If elliptic integrals were used to solve this problem, we would have to solve Eq. 2.65 for the cases when:

- $p^2 > 1$: such solutions are associated with the non-inflectional solutions and
- $p^2 \leq 1$: such solutions are associated with the inflectional solutions.

When $t > 0$, as can be seen from Figure 2.11,

$$p^2 < 0. \tag{2.71}$$

We consider imaginary values of the the elliptic modulus p, i.e.,

$$p = \pm|p|\ i, \tag{2.72}$$

where $i = \sqrt{-1}$. In the context of the condition for inflectional solutions given by Eq 2.68, that means:

$$\sin^2\left(\frac{\phi}{2}\right) = -|p|^2. \tag{2.73}$$

Using the identity $i \sin(\phi) \equiv \sinh(i\phi)$, we find

$$\sinh^2\left(\frac{i\phi}{2}\right) = |p|^2 \tag{2.74}$$

which gives:

$$\sinh\left(\frac{i\phi}{2}\right) = \pm|p| \tag{2.75}$$

The above tells us that ϕ must be imaginary. From a physical point of view ϕ must be real since Eq 2.68 does not admit real solutions for $p^2 < 0$. To summarise, we observe that no real inflectional solutions exist. All solutions for $p^2 < 0$ (imaginary elliptic parameter p) must be non-inflectional.

The behaviour of p^2 for different values of γ_i and $|t|$ is shown in Figure 2.11. The plots appearing on the left and right hand side of that Figure correspond to a compressive and a tensile force for a rod that has certain values of intrinsic curvature respectively. The shaded and non-shaded areas in those graphs refer to values of p^2 which yield inflectional and non-inflectional solutions respectively. A rod that is deformed under a compressive force, i.e., $t < 0$, is shown in Figure (2.11) a(i), b(i) and c(i) for values of $\gamma_i = \frac{\pi}{4}, \pi$ and $\frac{3\pi}{2}$ respectively.

1. For $\gamma_i = \frac{\pi}{4}$, an infinitesimal force, $|t|$ causes the value of $p^2 \gg 1$. The value of p^2 drops below 1 for increased values of $|t|$ and then rises crossing $p^2 = 1$. In the limit, p^2 does not cross but stays asymptotic to 1.

2. For $\gamma_i = \pi$, $p^2 \gg 1$ for an infinitesimal $|t|$ and becomes asymptotic to 1 as $|t| \to \infty$. We should note that p^2 does not cross 1.

3. For $\gamma_i = \frac{3\pi}{2}$, $p^2 \gg 1$ for an infinitesimal $|t|$. As the value of $|t|$ is increased, p^2 crosses 1 and then becomes asymptotic to 1 for $|t| \to \infty$.

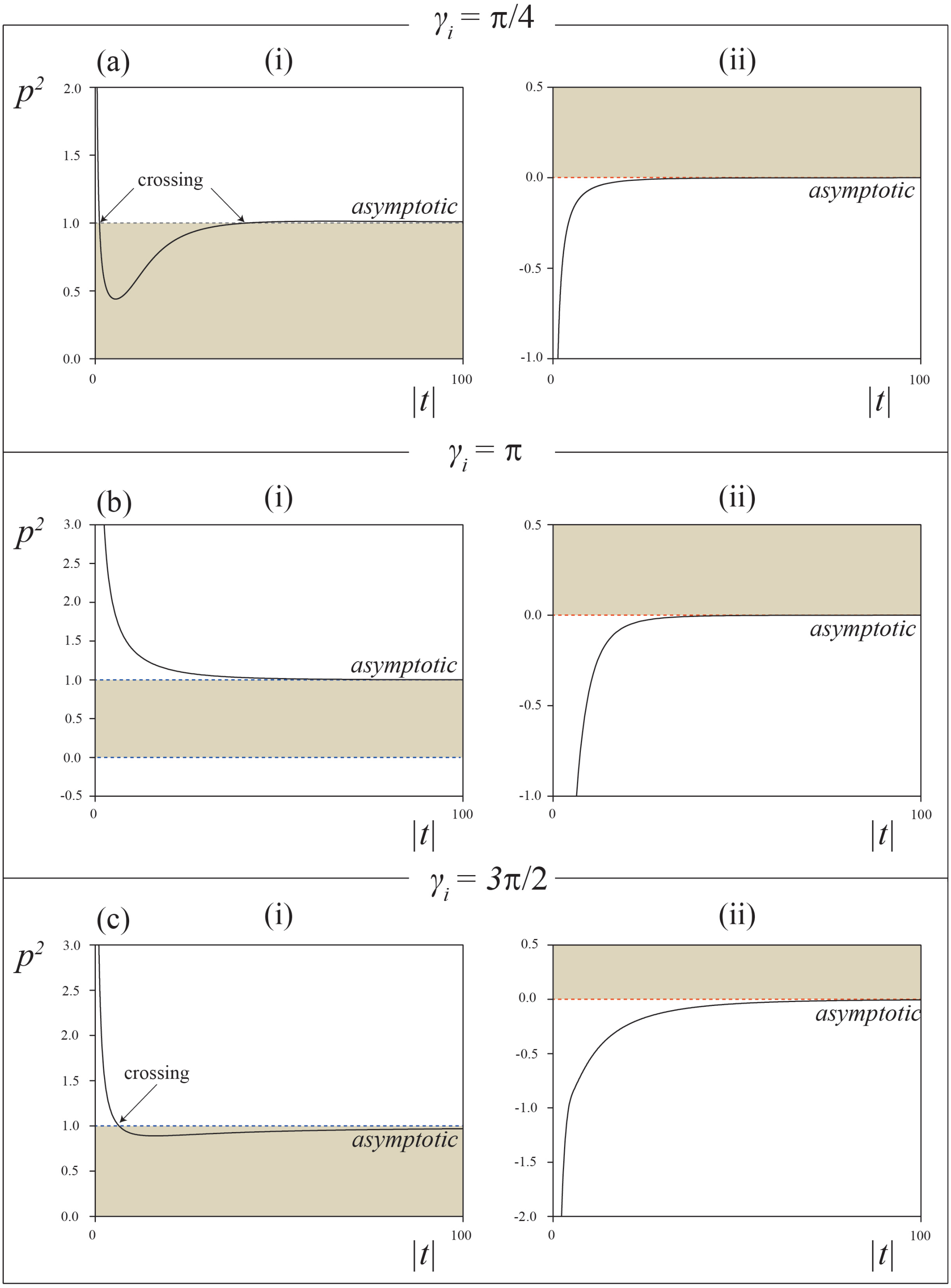

Figure 2.11: Plots of p^2 versus the magnitude of the force $|t|$, for (a) $\gamma_i = \pi/4$, (b) π and (c) $3\pi/2$. In each case (i) and (ii) correspond to compression and tension respectively. The shaded areas denote $0 < p < 1$, corresponding to inflectional solutions. Note that for solutions in compression (i) p^2 may take values greater or less than unity as t varies and according to the value of γ_i. However under tension (ii) p^2 is always less than than zero and the rod is always noninflectional.

2.8.2.2 Case II: LHP

An unstressed uniformly curved (with $\gamma_i = \pi/4$) and deformed rod is presented in Figure 2.12, see the black and green deformed shape respectively. The red filled circle located along the non-dimensional arc-length of the deformed rod and the parameters with an asterisk indicate the existence of an inflection point. For example the angle of the tangent at the inflection point $\gamma^* = \phi(s^*)$. We refer the reader back to Eq. 2.64 and the discussion following that. In the LHP the rod has negative curvature from the origin up to the inflection point s^* and positive curvature for the remainder.

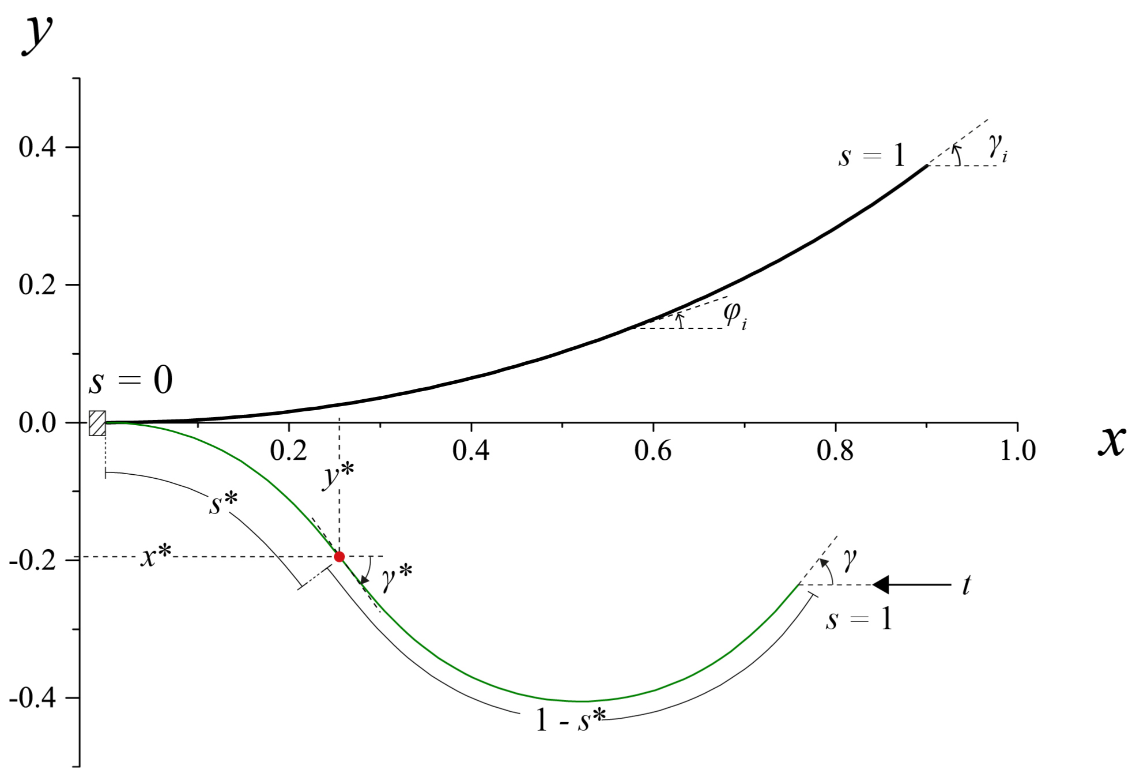

Figure 2.12: An unstressed uniformly curved rod (shown in black, where $\gamma_i = \pi/4$) along with a deformed rod (bent from the unstressed state and held with an applied compressive force) in the LHP. The deformed shapes in the LHP have an at least one inflection point

It follows that the curvature along the rod in the LHP is given by the following two first order, ordinary differential equations:

$$\frac{\mathrm{d}\phi}{\mathrm{d}s} = -\left(\gamma_i^2 - 4t\left(\sin^2\left(\frac{\gamma}{2}\right) - \sin^2\left(\frac{\phi}{2}\right)\right)\right)^{1/2} \quad 0 \le s < s^*, \tag{2.76}$$

$$\frac{\mathrm{d}\phi}{\mathrm{d}s} = \left(\gamma_i^2 - 4t\left(\sin^2\left(\frac{\gamma}{2}\right) - \sin^2\left(\frac{\phi}{2}\right)\right)\right)^{1/2} \quad s^* < s \le 1. \tag{2.77}$$

At the inflection point $\frac{\mathrm{d}\phi}{\mathrm{d}s}(s^*) = 0$,

$$\frac{\mathrm{d}\phi}{\mathrm{d}s}(s^*) = \pm\left(\gamma_i^2 - 4t\left(\sin^2\left(\frac{\gamma}{2}\right) - \sin^2\left(\frac{\gamma^*}{2}\right)\right)\right)^{1/2} = 0. \tag{2.78}$$

We find γ_i^2 from Eq. 2.78 and substitute into Eqs. 2.76 and 2.77 to obtain:

$$\frac{\mathrm{d}\phi}{\mathrm{d}s} = -2\left(-t\right)^{1/2}\left(\sin^2\left(\frac{\gamma^*}{2}\right) - \sin^2\left(\frac{\phi}{2}\right)\right)^{1/2} \quad 0 \le s < s^*. \tag{2.79}$$

$$\frac{\mathrm{d}\phi}{\mathrm{d}s} = 2\left(-t\right)^{1/2}\left(\sin^2\left(\frac{\gamma^*}{2}\right) - \sin^2\left(\frac{\phi}{2}\right)\right)^{1/2} \quad s^* < s \le 1. \tag{2.80}$$

The equation for the arc length up to the inflection point is is given below:

$$\int_0^s \mathrm{d}u = -\frac{1}{2\left(-t\right)^{1/2}}\int_0^\phi \frac{\mathrm{d}\psi}{\left(\sin^2\left(\frac{\gamma^*}{2}\right) - \sin^2\left(\frac{\psi}{2}\right)\right)^{1/2}}. \tag{2.81}$$

To express this integral in standard form we introduce a new integration variable θ, which is defined as follows:

$$\theta = \arcsin\left(\frac{\sin\left(\frac{\psi}{2}\right)}{p^*}\right), \tag{2.82}$$

where p^* is the elliptic modulus defined at the inflection point,

$$p^* = \sin\left(\frac{\gamma^*}{2}\right). \tag{2.83}$$

It follows that elliptic parameter $p^{*2} \in [0, 1]$ and the solutions are thus inflectional. We derive the solutions for the deformed rod in the LHP in §3.4.1.

2.9 Discussion

The system of first order ordinary differential Eqs. 2.35-2.39, along with the boundary conditions given in Table 2.1 constitute a well posed system. It is solved by a single-parameter continuation of either d or f using the software AUTO. We should remark that the system of ODEs given by Eqs. $2.35 - 2.39$ and the boundary conditions stipulated in Table 2.1 reflects more directly the experimental set-up and by setting the equations under continuation of d or t, we mimic the actual experimental procedure.

For the study of the behaviour of real rods as observed through experiments, we need to pay special attention to the experimental set-up. As much as it is practically possible, we seek to identify and eliminate physical imperfections that may cause the experimental data to depart away from the mathematical model. For instance, we require rods with linear elasticity at large deformations, and avoid heavy rods. We pause here to remark that we can take our experiments beyond the scope of our mathematical model, i.e., in our experiments we can encompass self contact, extension of the rod, shear and very large deformations in which the linearity assumptions of our constitutive relation is no longer valid.

In section 2.8.2.1 we formulate the solutions to deformed rods in the UHP and we show that the elliptic parameter can yield values in the ranges specified in Eqs. 2.69−2.70. Rods that are deformed with a force $t < 0$ correspond to values where $p^2 \leq 1$ and $p^2 > 1$, and are defined as inflectional and non-inflectional respectively; those corroborate with [10] and what they called “first” and “second” type respectively. Solutions that arise for values of $t < 0$ correspond to $p^2 < 0$. Those correlate with [10] and the solutions that they called the “third” type. In

Figure 2.11 we present plots of p^2 vs. $|t|$, where (a), (b) and (c) correspond to $\gamma_i = \frac{\pi}{4}, \pi$ and $\frac{3\pi}{2}$ respectively. In the case of $t < 0$, i.e., (a(i)), (b(i)) and (c(i)), the value of p^2 is not well-behaved. For the case where $t > 0$ the elliptic parameter $p^2 < 0$ and the solutions are noninflectional. The inconsistency of p^2 makes the use of elliptic integrals unwieldy and we therefore solve this BVP using AUTO.

In §2.8.2.2 we formulate the solution (using elliptic integrals) to rods that are located in the LHP. As a result of the interior inflection point the solution to the rod is governed by two first order ODEs, see Eqs. 2.76 and 2.77. Additionally, we present the equation for the curvature at the inflection point and it follows that we reduce equations (Eqs. 2.76 and 2.77) to standard elliptic form. Thus, we define the elliptic modulus p^* in terms of the angle γ^* and it follows that the elliptic parameter $0 < p^{*2} \leq 1$.

Solutions are either inflectional or noninflectional and such solutions are classified in terms of the value of the elliptic parameter [9]. The value of the elliptic parameter to solutions in the UHP is muddled and the shapes correspond to either inflectional or noninflectional shapes. The interior inflection point in deformed rods that are located in the LHP means that the deformed shapes are of one type, i.e., inflectional.

The remaining chapters of this thesis reports on the experimental, numerical and some analytical results on the large deflections of both uniformly curved and straight rods.

Chapter 3

Loop formation and jumps in curved rods

3.1 Introduction

In this chapter we compute the equilibrium diagrams and deformed shapes of a rod that has uniform intrinsic curvature. As we have discussed in the previous chapter, there are two qualitatively different equilibrium shapes. There are those that do not have interior inflection points (red and blue deformed shapes shown in Figure 2.9) and those that do have interior inflection points (green deformed shapes that are depicted in Figure 2.9). The deformed shapes in the UHP and LHP are obtained experimentally and compared with theoretical results. The experimental solutions are obtained under the continuation of d and t i.e., rigid and dead loading respectively. Note, that in this chapter $\alpha = 0$ and $f = \pm t$.

We begin this chapter with a review on the previous work appertaining to clamped-free rods that have some degree of uniform curvature in their unstressed state. The experimental set-up is given in §3.2 and then we give the results (experiments and theory) for deformed rods in the UHP and LHP in §3.3 and §3.4, respectively. Within those sections we give the conditions for loop formation and critical unstable points.

Few naturally occurring rod-like structures are actually straight and, be it trivial or not, nearly all contain some magnitude of intrinsic curvature. An example of intrinsically curved rod like structures are human hair (see [40] for a survey) and mammalian whiskers (see [41] for a review on whisker modelling).

In the case of a straight rod, the equation representing the curvature, i.e., Eqs. 2.37−2.38 can be expressed in standard elliptic integral form, (see [4], [5] and [6]), and then solved for certain values of the elliptic parameter. The value of the elliptic parameter can be expressed in terms of the of the tip angle (of the rod), and thus the elliptic argument varies from 0 to $\frac{\pi}{2}$. Owing to the boundary conditions it follows that the solutions are always inflectional. In contrast, the corresponding solutions for intrinsically curved rods are muddled.

Studies on intrinsic curvature are usually approached from various perspectives. Some studies define the problem and then obtain results using numerical software, and others define the problem and obtain closed form solutions [6] and [10]. Examples of the former include the studies [12], [11] and [24]. The author of [11] considers the uniformly curved rod and compares the loading paths that obtained using linear theory to those obtained using nonlinear theory. The author computes the solutions using a numerical solver. A uniformly curved rod that is subjected to a follower load is considered in [24], where a Runge-Kutta method with a shooting technique is used to compute the loading paths and deformed shapes. The author of the paper [12] considers a uniformly curved rod that is deformed by an eccentric load applied at the tip. Equations for the arc-length and the end displacement are presented in integral form and then solved simultaneously for pairs of values of applied force and end displacement. The authors plot loading diagrams for small values of initial curvature along with the loading path for the straight rod. They also present some deformed shapes. Note that the studies that we have discussed above are useful for comparing results, however the authors do not discuss any analysis.

A few pertinent studies that discuss the closed form solutions and the complications involved are in [6] and [10]. In chapter 4 of the book [6], the author examines the uniformly curved clamped-free rod that is loaded with an axial force (a force that acts in the direction along negative $\mathbf{i}$ in our model). The author expresses the solution in terms of elliptic integrals and reports on an issue that crops up with respect to the elliptic parameter. The author reports that a small change in the value of end force can cause a large change in the value of the elliptic parameter. This effect is that the distinction between two qualitatively different types of configurations, namely those with inflection points and those without (inflectional and non-inflectional respectively), which is clear in the case of intrinsically straight rods, becomes muddled. The author gives the different types of solutions that arise, however does not attempt to classify the solutions. The same problem is also analysed by [10]. The author categorises the deformed shapes into three 'types' (which arise due to values of the elliptic parameter), and shows that rods that are deformed under a compressive force may correspond to inflectional or non-inflectional shapes, whereas rods that are deformed under a tensile force always correspond to non-inflectional. The authors of the papers [6] and [10] are useful in providing an insight into the complications that arise with respect to the analysis. They show the different types of solutions that can arise depending on the value of the elliptic parameter. However, they do not give a global overview on the relationship between the elliptic parameter and the force, nor do they study the effect of large curvature.

The author in [42] performed experiments on uniformly curved elastomeric rods which are clamped at both ends. The author observed that the configurations of the deformed rod were quantitatively and qualitatively different for each case, and that the effect of weight "delayed" the effect of curvature. The author did not induce high values of curvature and similarly to [4] considered deformations whereby both twist and end displacement were varied.

Experimentally we find that loop formation arises at critical values of initial curvature. We find that loop formation is directly linked to the effect of curvature and the applied force. We compare those critical values with the planar theory and a semi-analytical approach. Note, that in the experiments the rod cannot self-intersect and during loop formation there is a small amount of out of plane deformation. That out of plane deformation, is only the thickness of the rod. Loop formation is a three-dimensional phenomena, however, we use rods that have rectangular cross-sections and out of plane deformations are negligible. Nevertheless, we find a very good match between the experiments and the planar theory.

The formation of loops can lead to kinks in cables and this may lead to permanent damage. Cables that are stored in spools can develop permanent curvature, and upon application of end forces a loop could form. If tightened, the loop could develop into a kink and permanently damage the cable [43]. Nitinol can be bent around radii of less than 3cm without kinking, see [29, 44]. Nitinol is renowned for its kink resistance [29].

Only a few experimental studies on loop formation in rods exist in the literature, see [45] and [46]. The experimental study by [46] investigates hockling and pop-out. They derive formulae for both the formation of a loop and the point at which it buckles out of the plane. They compare the results with experimental data. The thesis by [4] shows experimental and analytical results whereby loop formation occurs and then pops out. The author uses the three-dimensional theory and determines an analytical expression for pop-out. The paper by [47] uses the three dimensional theory and determines the condition for pop-out in the noninflectional rod. Other pertinent studies on loop formation that have employed rod theory include [43], [45] and [48].

3.2 Experimental set-up

Experiments on rods that are identified with the UHP and LHP are conducted under rigid and dead loading respectively. The experimental rig pictured in Figure 3.1 is used in both cases. In this section we describe the experimental apparatus and procedure for a rod that is deformed under those loading procedures.

3.2.1 Case I: UHP

The experimental set-up is depicted in Figure 3.1. One end of the uniformly curved rod ($S = 0$) is fixed in the chuck (see Figure 2.4) and the other ($S = L$)

is inserted into a bespoke pin-joint-slider device, see Figure 3.2. The device was

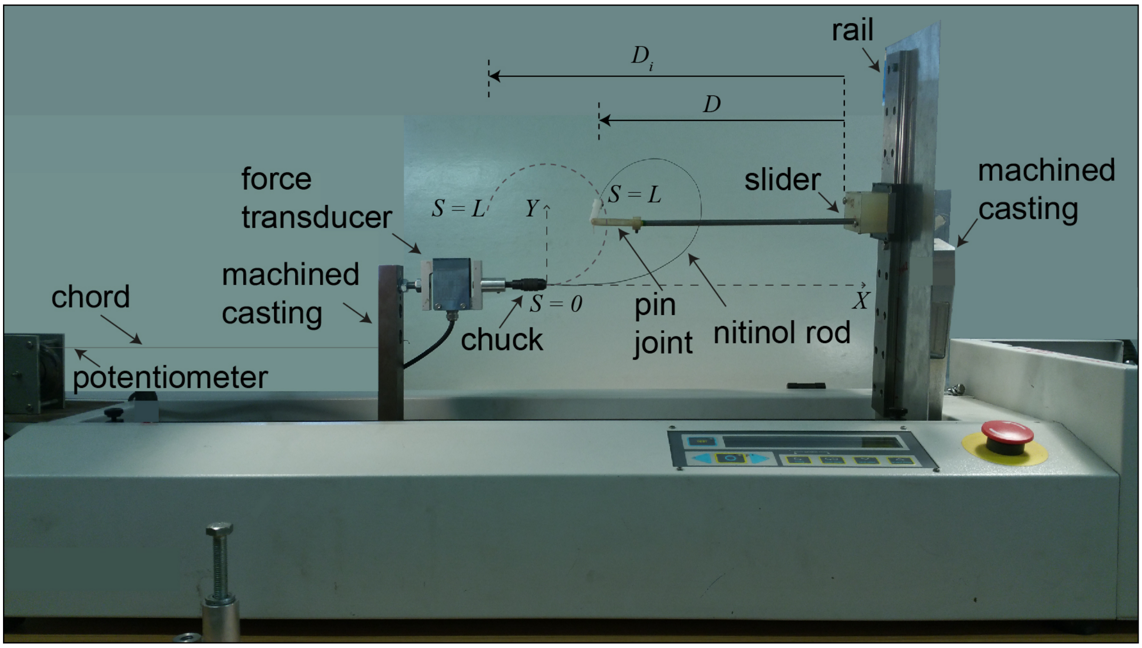

Figure 3.1: The experimental set-up for experiments on initially curved rods under rigid displacement, D. An experiment starts with the rod clamped in its unstressed state at distance D_i.

designed and constructed to model the boundary condition specified at $S = L$ (Eqs. 4 and 5b in Table 2.1), see Figure 3.2. This consists of a slider, rail and a specially designed one-degree of freedom pinned joint that permits rotations $0 > \gamma \gtrapprox 2\pi$.

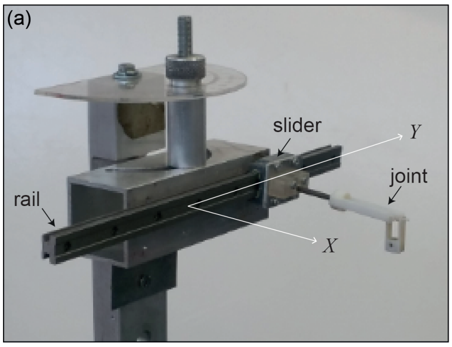

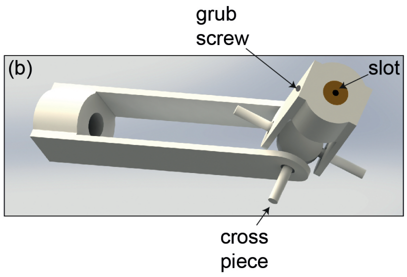

Figure 3.2: Details of the pinned joint at $S = L$. (a) The pinned joint is attached to the slider and free to move along the rail (Y-axis). (b) The nitinol rod is held in the slot by means of a grub screw. The pinned joint is allowed to rotate about the cross piece.

Once the rod is fixed in the rig, it is situated at an initial distance D_i from the clamped end ($S = 0$). An experiment proceeds by displacing the clamped end in a straight line by amount D either towards or away from the pinned end. During that displacement, the pinned end is free to slide up and down along the rail (Y axis). A transducer records the force in the rod. Note that for $D \to 0$, $T > 0$ and for $D \to 2$, $T < 0$. The value of D includes the initial distance D_i and is always positive.

For numerical simulations we solve Eqs. 2.35−2.39 along with the boundary conditions (1) – (4), and 5(b), (see Table 2.1) under the continuation of d.

3.2.2 Case II: LHP

For these experiments we position the rig such that the X-axis acts in the direction opposite to acceleration due to gravity, see Figure 3.3. In its unstressed state the configuration of the rod is identified with the UHP. By applying a bending moment (by hand) that is opposite to the rods intrinsic curvature, the rod is bent into a configuration that is identified with the LHP, see Figure 3.3. Upon application of the bending moment an inflection point arises at $S = S^*$. Note, to hold the rod in equilibrium such that it can be described in terms of the LHP, an end load is required to stop the rod flicking back to its unstressed state (which is in the UHP). We remark here that the aforementioned applied bending moment is not accounted for in our mathematical model. Furthermore, we think it is impossible for a rod to be bent into the LHP from its natural state under the loading specified in our model.

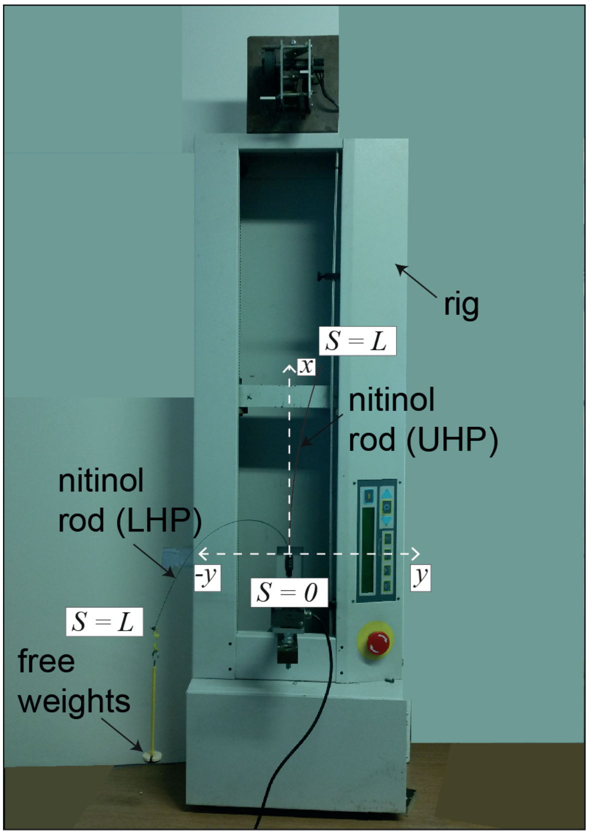

Figure 3.3: The experimental rig along with an unstressed and deformed nitinol rod in the UHP and LHP respectively. A bending moment opposite to the rods intrinsic curvature is applied at the tip of the rod, and the rod transitions from the UHP to the LHP. Once in that plane the rod is held in equilibrium with a weight.

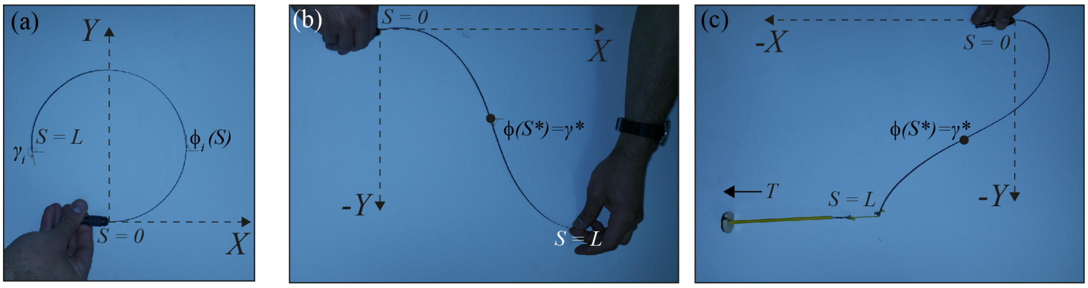

Figure 3.4: (a) A uniformly curved rod with $\gamma_i \approx 3\pi/2$. In this state the rod is described in the UHP. (b) The rod undergoing a bending moment of opposite sign to its intrinsic curvature, such that the rod is described in the LHP. Note that during this process an inflection point is introduced at S^*. (c) The rod is held in the LHP by a weight attached at $S = L$. An experiment proceeds by either attaching or detaching weight.

An experiment begins by either adding or removing load. Experimental data is obtained by recording the load and the position of the tip of the rod $X(L)$. The experimental data is nondimensionalised and plotted with the (nondimensional) theory.

For numerical simulations we solve Eqs. 2.35−2.39 along with the boundary conditions $(1) - (4)$, and 5a, (see Table 2.1) under the continuation of t. Note, in order to obtain the numerical data we have to adjust the step-size.

3.3 Results: Case I UHP

The theoretical equilibrium paths and experimental data points that correspond to a rod with different values of intrinsic curvature are presented. The theoretical loading paths are depicted in Figures 3.5 and 3.6 and the experimental data are shown in Figures 3.7 and 3.8. The formation of a loop(s) occurs at critical values of curvature and the loading paths depicted in Figures 3.5, 3.7 and Figures 3.8, 3.6 correspond to deformed shapes that have no loop and one loop respectively. The positions of the tip of the unstressed rod d_i is represented with white filled circles. Note that all values of t (both experimental and theoretical) are normalised by t_E, see Eq. 2.45.

The theoretical loading path for an initially straight rod ($\gamma_i = 0$) is shown in black in Figures 3.5 and 3.6. In the case where a force corresponding to $\frac{t}{t_E} > -1$, the rod does not deform and remains in its initial straight state. If a force is applied such that $\frac{t}{t_E} < -1$ the rod deflects, bifurcating at $\frac{t}{t_E} = -1$ (primary bifurcation). The rod can buckle into either the UHP or LHP, see Figure 2.8. Note that if the primary bifurcation is stabilised the rod can buckle into an infinite number of equilibrium states, i.e., *mode shapes*, as shown in [4].

The loading paths shown in blue in Figure 3.5 correspond to values of initial curvature in the range $0 < \gamma_i \leq \frac{133\pi}{90}$. There is no bifurcation and upon input of a force of any magnitude and direction, the rod deforms from its reference state (refer to the blue loading paths). The loading paths in the region where $\frac{t}{t_E} > 0$ correspond to deformed shapes where $d \to 0$. Note that rods with initial curvature cannot be pulled straight, i.e., $d \neq 0$. In the region where $\frac{t}{t_E} < 0$ the loading paths (blue paths), cross such that in the limit they approach the loading path of the straight rod (black path). For values of intrinsic curvature that approach a critical value for loop formation, there is a sharp gradient as $t > 0$ is applied to the unstressed rod, see the loading path that corresponds to $\gamma_i = \frac{133\pi}{90}$. The sudden change in gradient for $\gamma_i = \frac{133\pi}{90}$ signifies that the rods curvature is close to the critical value of curvature where loop formation occurs.

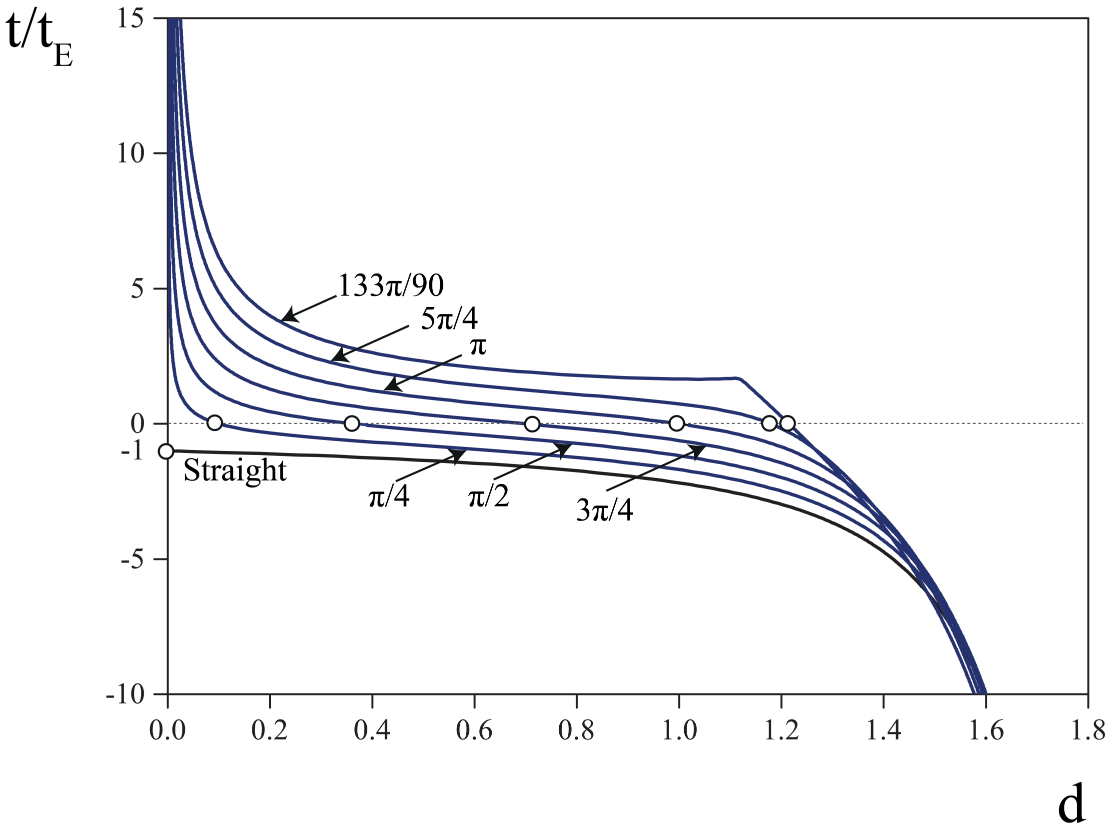

Figure 3.5: The td loading diagram for a rod with uniform curvature along with the loading path of the straight rod. The open circles in those paths denote the position of the unstressed rod d_i.

The theoretical loading paths shown in Figure 3.6 correspond to a uniformly curved rod that has initial curvature in the range $\frac{3\pi}{2} \leq \gamma_i \leq 3\pi\forall$. The red loading paths correspond to deformed shapes where one loop forms and exists for $t < 0$. The green loading paths correspond to deformed shapes where one loop forms and exists for both $t < 0$ and $t > 0$. Loading paths that correspond to greater values of the critical curvature (where loop forms) are qualitatively different. Loop formation involves high change in forces and this is reflected in the steep gradient in the corresponding loading diagrams. In the $t > 0$ region the loading paths do not approach zero in the limit and this is because the rod has a loop. The loading paths when $t < 0$ is applied are of two types: those that have one loop (refer to the green loading paths in Figure 3.6) and those that have no loop (refer to the red loading paths in Figure 3.6). We investigate the conditions for loop formation in §3.3.1.

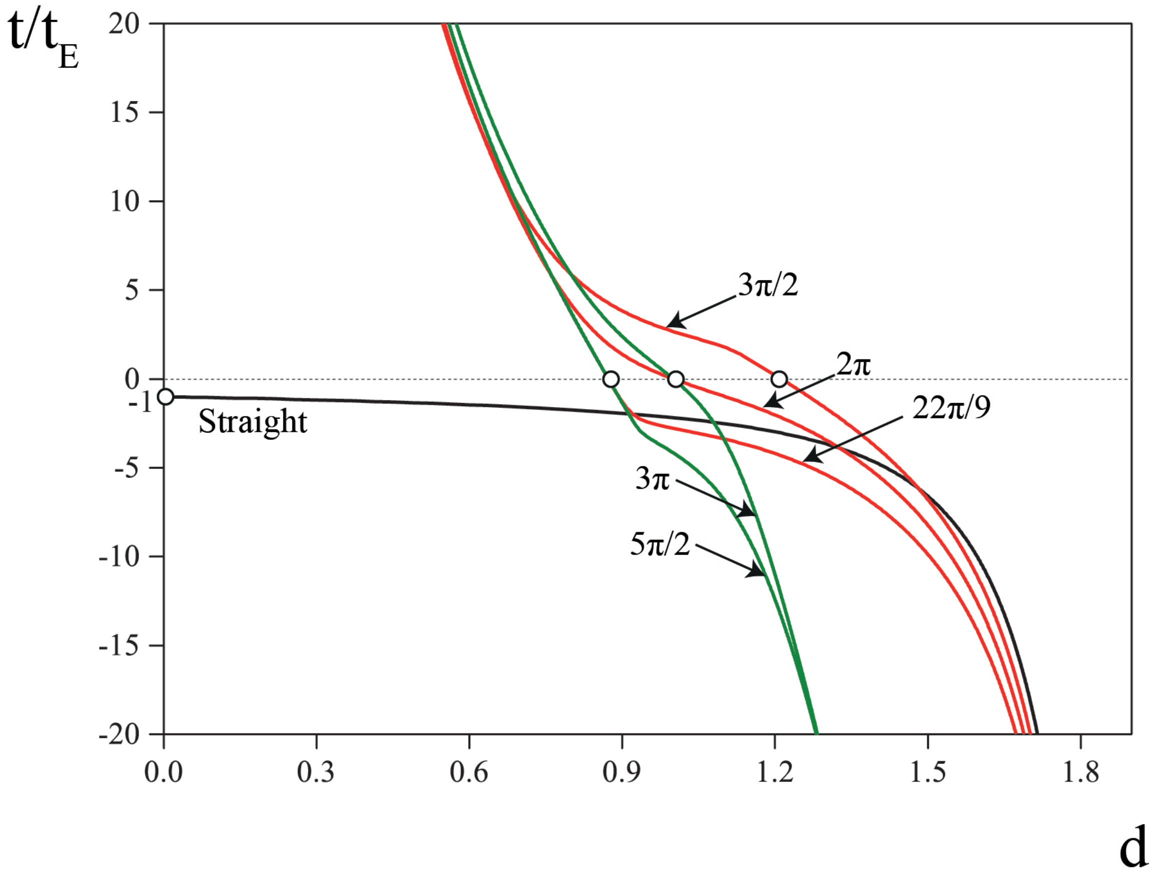

Figure 3.6: The td loading diagram for a rod with uniform curvature along with the loading path of the straight rod. The open circles in those paths denote the position of the unstressed rod d_i.

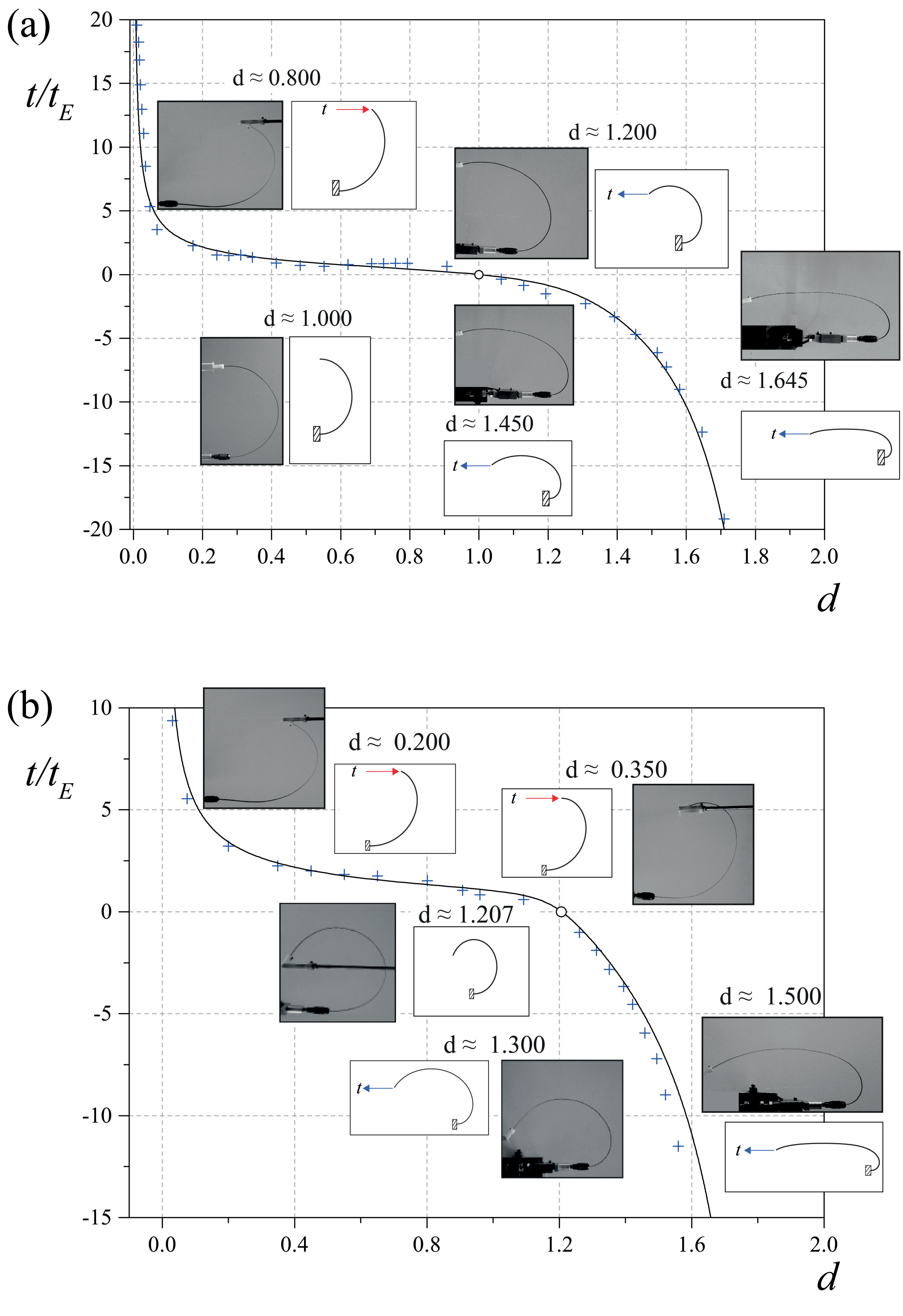

Figure 3.7: Experimental data points (blue crosses) along with data obtained from AUTO (continuous black line) for a rod with uniform curvature where (a) $\gamma_i \approx \pi$ and (b) $\gamma_i \approx \frac{4\pi}{3}$. The open circles denote the position of the unstressed rod D_i and in both cases no loop formation is observed. The experimental data is in close agreement with the theory, however during loop formation the rod slides past itself causing unwanted friction. Also, exact alignment of the ends and satisfaction of the boundary conditions could contribute to the deviation of the experimental data points from the theory.

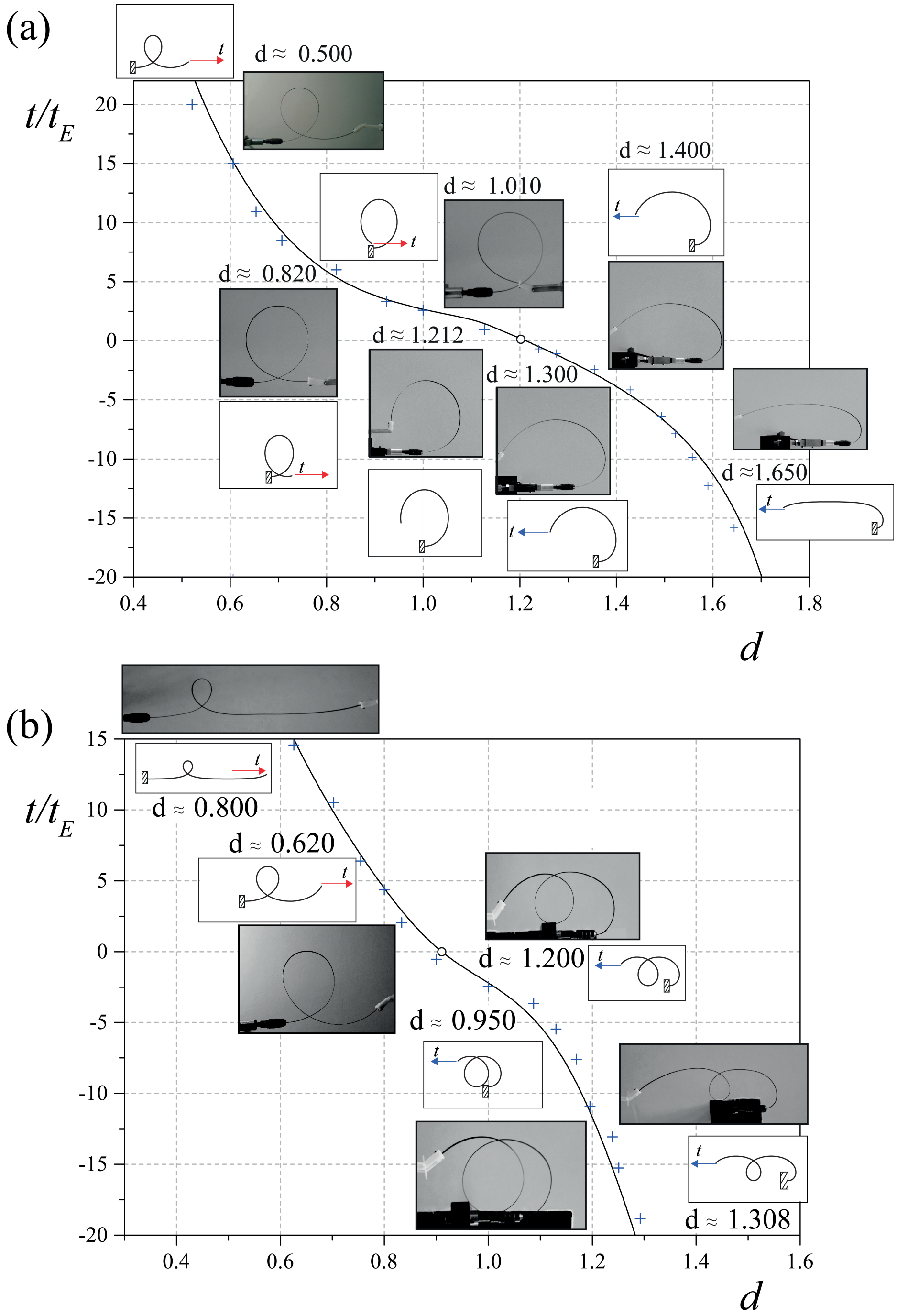

Figure 3.8: Experimental data points (blue crosses) along with data obtained from AUTO (continuous black line) for a rod with uniform curvature, where (a) $\gamma_i \approx \frac{3\pi}{2}$ and (b) $\gamma_i \approx \frac{49\pi}{18}$. The open circles denote the position of the unstressed rod D_i and in the case of $\gamma_i \approx 3\pi/2$ one loop forms and remains under further loading of $t > 0$. For $\gamma_i \approx \pi/18$ one loop forms and is still present for both $t > 0$ and $t < 0$. The experimental data is in close agreement with the theory, however during loop formation the rod slides past itself causing unwanted friction. Also, exact alignment of the ends and satisfaction of the boundary conditions could contribute to the deviation of the experimental data points from the theory.

The theoretical and the experimental data is depicted in Figures 3.7-3.8. The continuous line and the blue crosses denote the loading paths that are obtained from the theory and the experiments respectively. In the case where $\gamma_i = \pi$ and $\gamma_i = \frac{4\pi}{3}$ (see (a) and (b) in Figure 3.7 respectively), there is no loop formation for both $t < 0$ and $t > 0$. For values of intrinsic curvature $\gamma_i = \frac{3\pi}{2}$ (see Figure 3.8 (a)), one loop forms for values of $t > 0$ only. In the case for $\gamma_i = \frac{49\pi}{18}$, (see Figure 3.7 (b)), one loop forms for $t < 0$ and $t > 0$.

The experimental data correlate reasonably well with the theory. We identified two sources where friction was a problem. Firstly, the slider does not move in a continuous motion and there are irregular jerks of motion as D is input, and secondly, during the formation of a loop the rod makes contact with itself and again causes irregular jerks of motion. The experimental data that is presented in Figures 3.7 and 3.8 correspond to the mean of at least five separate experiments. In general, the experimental data is in close agreement with the theory. However, deviation of experimental data from the theory may be explained by a number of factors. First, whilst every attempt has been made to ensure the rods a have uniform intrinsic curvature along their entire length this was difficult to obtain. Second, exact replication of the boundary conditions, including alignment and ensuring the assumptions of planarity are prone to error. Also, during loop formation the configuration of the rod is clearly not planar (in the elastica theory a rod can self intersect). Furthermore, a normal force and friction act at the point of self contact.

3.3.1 Conditions for loop formation

Observation of our experiments along with the numerical computation indicate that deformed shapes can either have no loop or n loop(s), where $n = 1, 2, 3, ..., \infty$. The loop is dependent on both the loading procedure and the magnitude of initial intrinsic curvature. We compute and plot the deformed shapes for rods with curvature of $\gamma_i \approx \frac{133\pi}{90}, \frac{3\pi}{2}$ and $\frac{5\pi}{2}$ in Figures 3.9, 3.10 and 3.11 respectively. In those figures, (a) and (c) are deformed shapes that are obtained in AUTO and correspond to $t > 0$ and $t < 0$ respectively, and (b) depicts a nitinol rod that has the same value of intrinsic curvature. Note that the initial angle of the unstressed rod is denoted γ_i and as the rod deforms the angle is γ.

The deformed shapes for a rod that has initial curvature corresponding to $\gamma_i = \frac{133\pi}{90}$ are shown in Figure 3.9. As the end displacement $d_i > d$ ($t > 0$) is input, the curvature in the rod decreases and γ approaches zero. For the case where $d_i < d$ ($t < 0$) the rod deforms and the angle of the tip of the rod approaches π.

The deformed shapes of a uniformly curved rod for values of curvature that correspond to $\gamma_i = \frac{3\pi}{2}$ are shown in Figure 3.10. If end displacement is input, such that $d < d_i$ ($t > 0$), γ increases and self-intersects. Upon further inputs of displacement, the rod forms a loop and $\gamma \to 2\pi$. For a rod of the same curvature that is deformed under the application of $d > d_i$ ($t < 0$), there is no loop formation and γ decreases and tends to π.

Deformed configurations of a rod with an initial uniform curvature of $\gamma_i = \frac{5\pi}{2}$ are shown in Figure 3.11. A single loop forms and remains for both situations where $d < d_i$ ($t > 0$) and $d > d_i$ ($t < 0$) are applied i.e., a compressive and tensile force respectively. In the case where $d < d_i$ ($t > 0$) is applied, the angle of the tip of the rod decreases and approaches 2π. For values of $d > d_i$ ($t < 0$) the angle of the tip of the rod increases and approaches 3π.

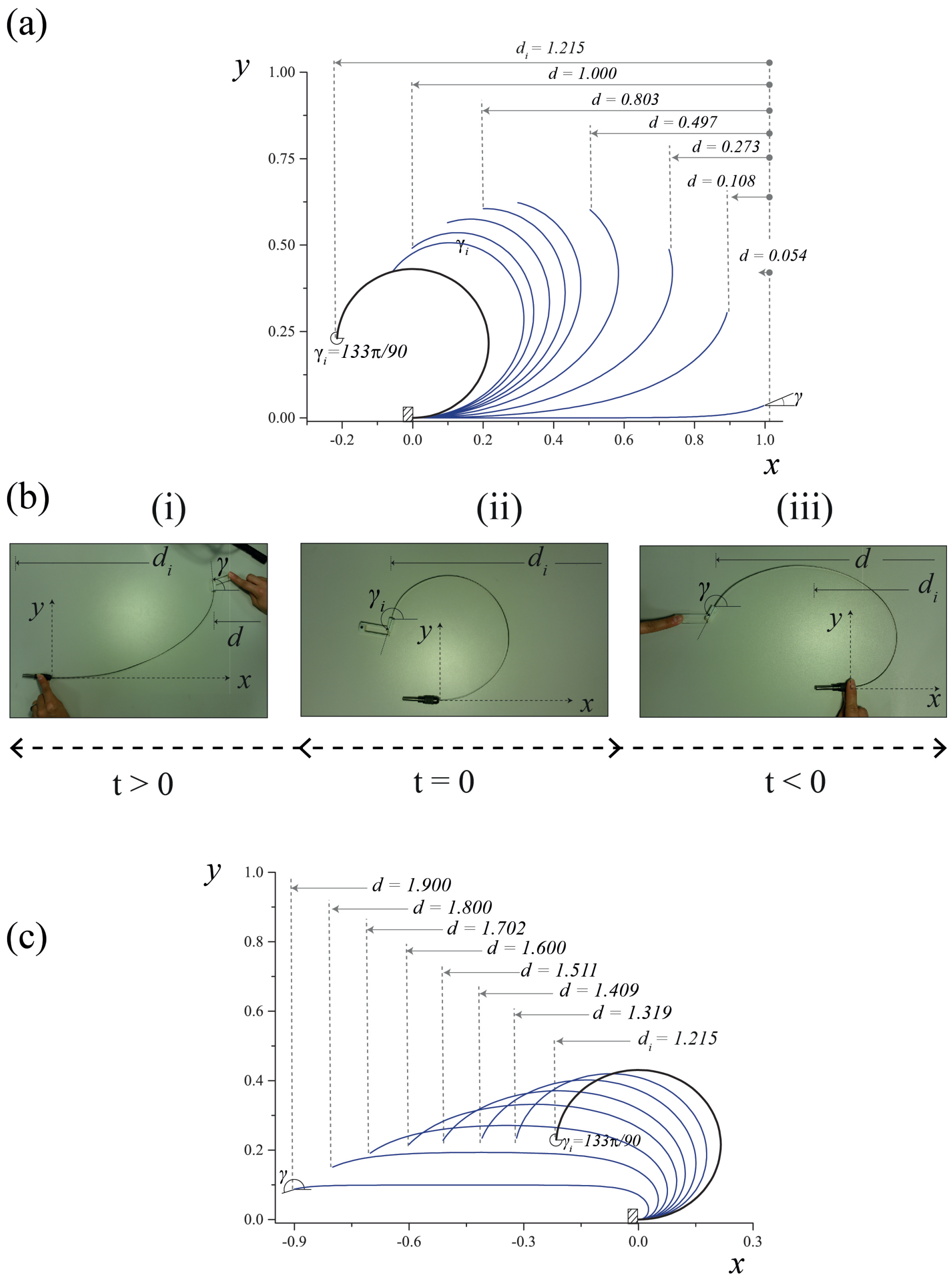

Figure 3.9: A uniformly curved rod with $\gamma_i = \frac{133\pi}{90}$. The deformed shapes in (a) and (c) correspond to the application of $t > 0$ and $t < 0$ respectively, and (b)(ii) shows an unstressed nitinol strip of the same curvature. In (b)(i),(iii) we show a deformed nitinol strip that is deformed under a$t > 0$ and $t < 0$ respectively. No loop formation occurs for $\gamma_i = \frac{133\pi}{90}$.

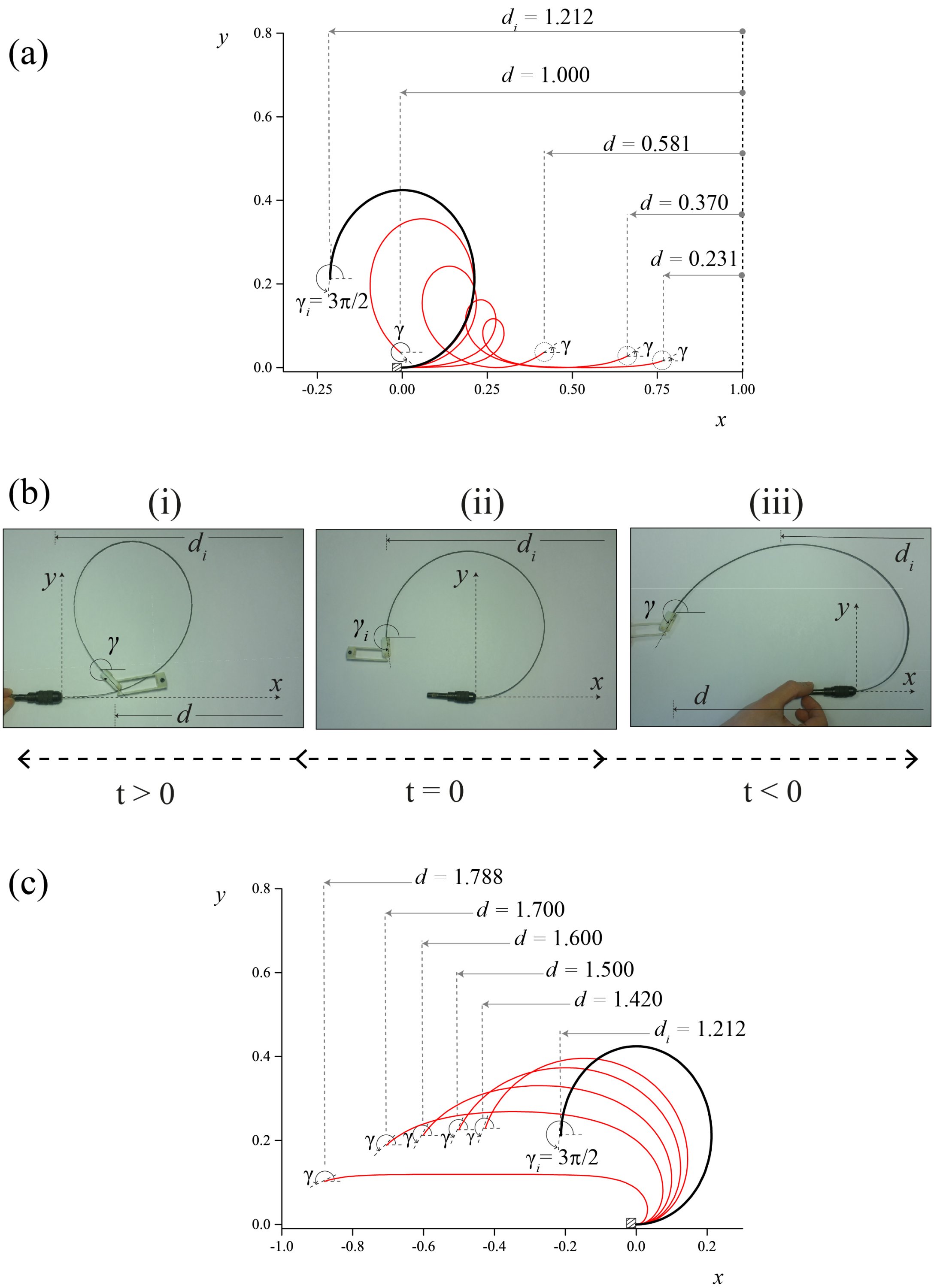

Figure 3.10: A uniformly curved rod with $\gamma_i = \frac{3\pi}{2}$. The deformed shapes shown in (a) and (c) correspond to a rod under the application of $t > 0$ and $t < 0$ respectively, and (b)(ii) shows an unstressed nitinol strip of the same curvature. In (b)(i),(iii) we show a deformed nitinol strip that is deformed under $t > 0$ and $t < 0$ respectively. Loop formation occurs when a tensile force $t > 0$ is applied, see (a) and (b)(i), however no loop forms or exists when a compressive force is applied, see (b)(iii) and (c).

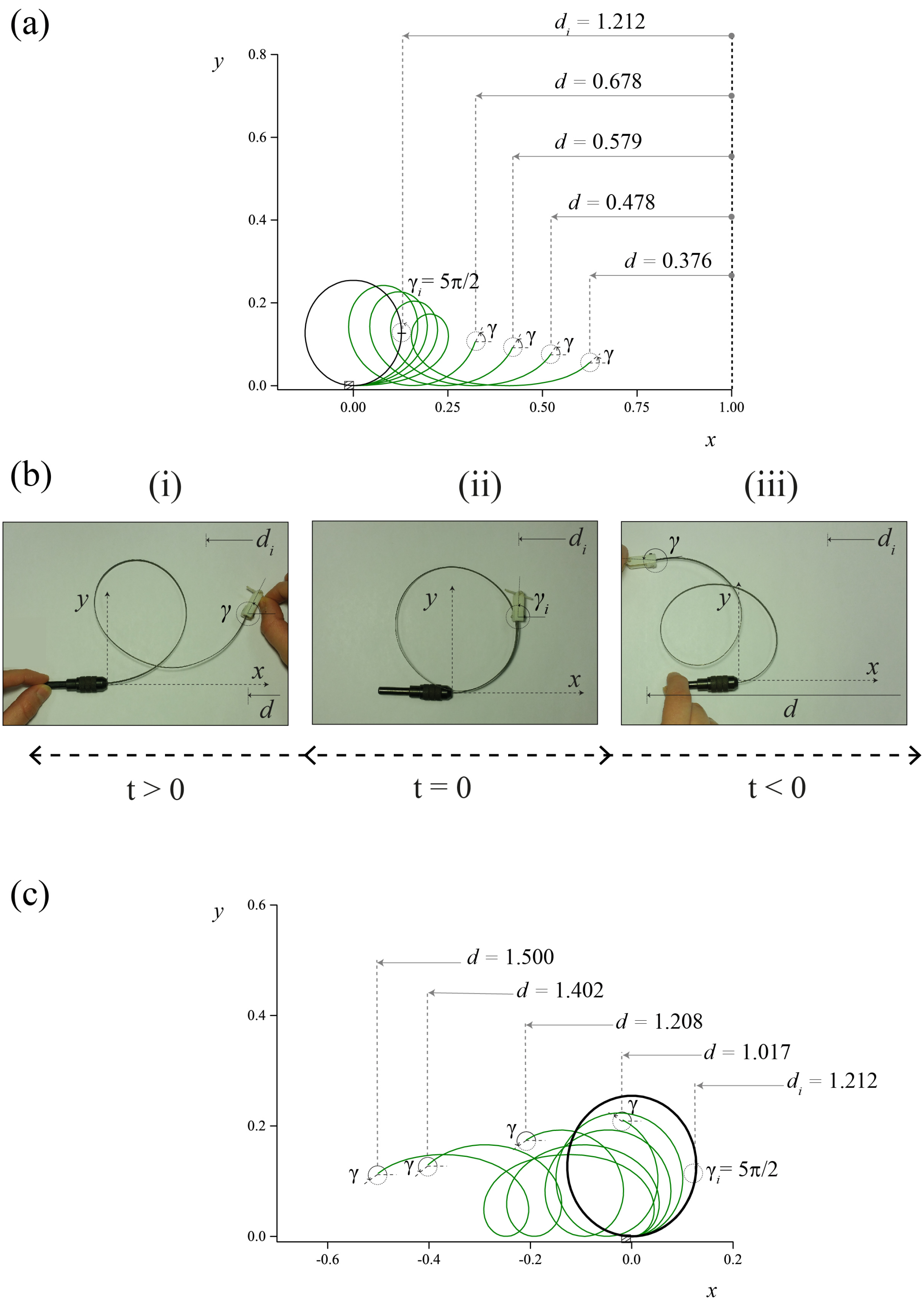

Figure 3.11: A uniformly curved rod with $\frac{5\pi}{2}$. The deformed shapes shown in (a) and (b) correspond to a rod under the application of $t > 0$ and $t < 0$ respectively, and (b) shows an unstressed and deformed nitinol strip of the same curvature, see (b)(ii) and (b)(i),(iii) respectively. One loop forms and exists when $t > 0$ (see (a) and (b)(i)) and $t < 0$ (see (b)(iii) and (c)) are applied to the rod.

Inspection of the deformed shapes show that the formation of loops in intrinsically curved rods depend on the end angle γ, the amount of initial curvature γ_i and the direction of D (or the applied force T), see Figure 3.12. In that Figure, (a), (b) and (c) correspond to $\gamma_i \approx \frac{133\pi}{90}$, $\gamma_i \approx \frac{3\pi}{2}$ and $\gamma_i \approx \frac{5\pi}{2}$ respectively.

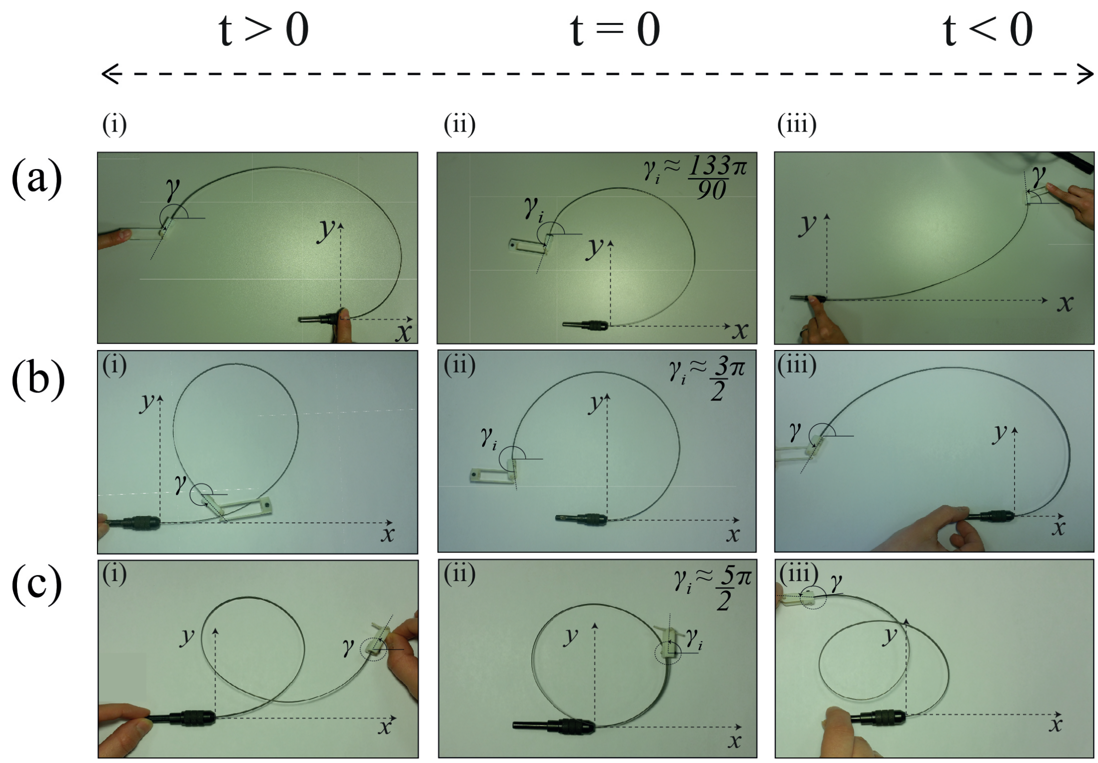

Figure 3.12: Photographs of experiments on nitinol rods with different values of intrinsic curvature. In (a)(ii), (b)(ii) and (c)(ii) those values correspond to $\gamma_i \approx \frac{133\pi}{90}$, $\gamma_i \approx \frac{3\pi}{2}$ and $\gamma_i \approx \frac{5\pi}{2}$ respectively. In some cases loops may (or may not) form under different loading sequences.

A three-dimensional loading diagram for a rod with different values of initial intrinsic uniform curvature, γ_i, is presented in Figure 3.13. The x, y and z axes denote the values of the force t, displacement d and end angle γ respectively. In the case where $\gamma_i = 0$ only values of $t < 0$ correspond to deformed configurations, see the black loading path in Figure 3.13. In this case the end angle varies from zero to π for different values of d. The divergence in the loading paths arise due to loop formation and are labelled 'A' and 'B'. Those points correspond to critical values of γ whereby loop formation occurs under applied $t > 0$ and $t < 0$ respectively. From Figure 3.13 it is observed that:

- for $\gamma_i \neq 0$ and $t > 0$ the value of γ either tends to 0 (no loop formation) or 2π (1 loop forms and exists),

- for $\gamma_i \neq 0$ and $t < 0$ the value of γ either tends to π (no loop formation) or 3π (1 loop forms and exists).

It is pertinent to define and plot the function $\gamma(t)$. Note that we obtain $\gamma(t)$ from AUTO, see Figure 3.14 where we present different values of initial curvature γ_i. We observe from that figure that the angle of the tip of the rod tends to the following values:

$$\gamma(t) \rightarrow 2n\pi, \qquad \text{for} \quad t > 0, \quad n = 0, 1, 2, 3, ..., \infty, \tag{3.1}$$

$$\gamma(t) \rightarrow (2n+1)\pi, \qquad \text{for} \quad t < 0, \quad n = 0, 1, 2, 3, ..., \infty. \tag{3.2}$$

If $n = 0$, there is no loop formation and the angle of the tip approaches 0 and π for $t > 0$ and $t < 0$ respectively, see the blue paths shown in Figure 3.14. For one loop to form, the angle of the tip of the rod approaches 2π and 3π for $t > 0$ and $t < 0$, respectively (see the red and green paths shown in Figure 3.14 respectively). In general, loop formation only occurs at critical values of γ_i, see points A and B in Figure 3.14 respectively). We denote those critical values as γ_n^c and γ_n^t, the subscripts c and t denote compression and tension respectively, and n is the number of loops that will subsequently form. Next, we show the method for determining γ_n^c and γ_n^t.

The function $\gamma(t)$ can be approximated around an infinitesimal force ($|t| \ll 1$) using a Taylor series expansion. We express $\gamma(t)$ and note that $\gamma(0) = \gamma_i$,

$$\gamma(t) = \gamma(0) + \frac{d\gamma(t)}{dt}\Big|_{t=0} t + \frac{d^2\gamma(t)}{dt^2}\Big|_{t=0} \frac{t^2}{2} + \mathcal{O}(t^3). \tag{3.3}$$

For convenience we define the following:

$$\dot{\gamma}_i := \frac{d\gamma(t)}{dt}\Big|_{t=0}, \tag{3.4}$$

$$\ddot{\gamma}_i := \frac{d^2\gamma(t)}{dt^2}\Big|_{t=0}. \tag{3.5}$$

We observe from Figure 3.14 that generally for an applied tensile force, i.e., $t > 0$, the function $\gamma(t)$ increases for the formation of one loop and decreases for no loop formation. For an infinitesimal tensile force Eq. 3.3 indicates that if $\dot{\gamma}_i < 0$ with t increasing, $\gamma(t)$ decreases and the tip of the rod is pulled straight. For a compressive force Eq. 3.3 indicates that if $\dot{\gamma}_i > 0$, with t decreasing, $\gamma(t)$ decreases and the rod is also pulled straight (since $t \ll 0$). To summarise, in order for γ to increase and the rod form a loop, the following conditions must be satisfied.

1. For loop formation of a rod under a compressive force, i.e., $t < 0$:

$$\dot{\gamma}_i < 0, \tag{3.6}$$

$$\ddot{\gamma}_i > 0. \tag{3.7}$$

2. For loop formation of a rod under a tensile force, i.e., $t > 0$:

$$\dot{\gamma}_i > 0, \tag{3.8}$$

$$\ddot{\gamma}_i > 0. \tag{3.9}$$

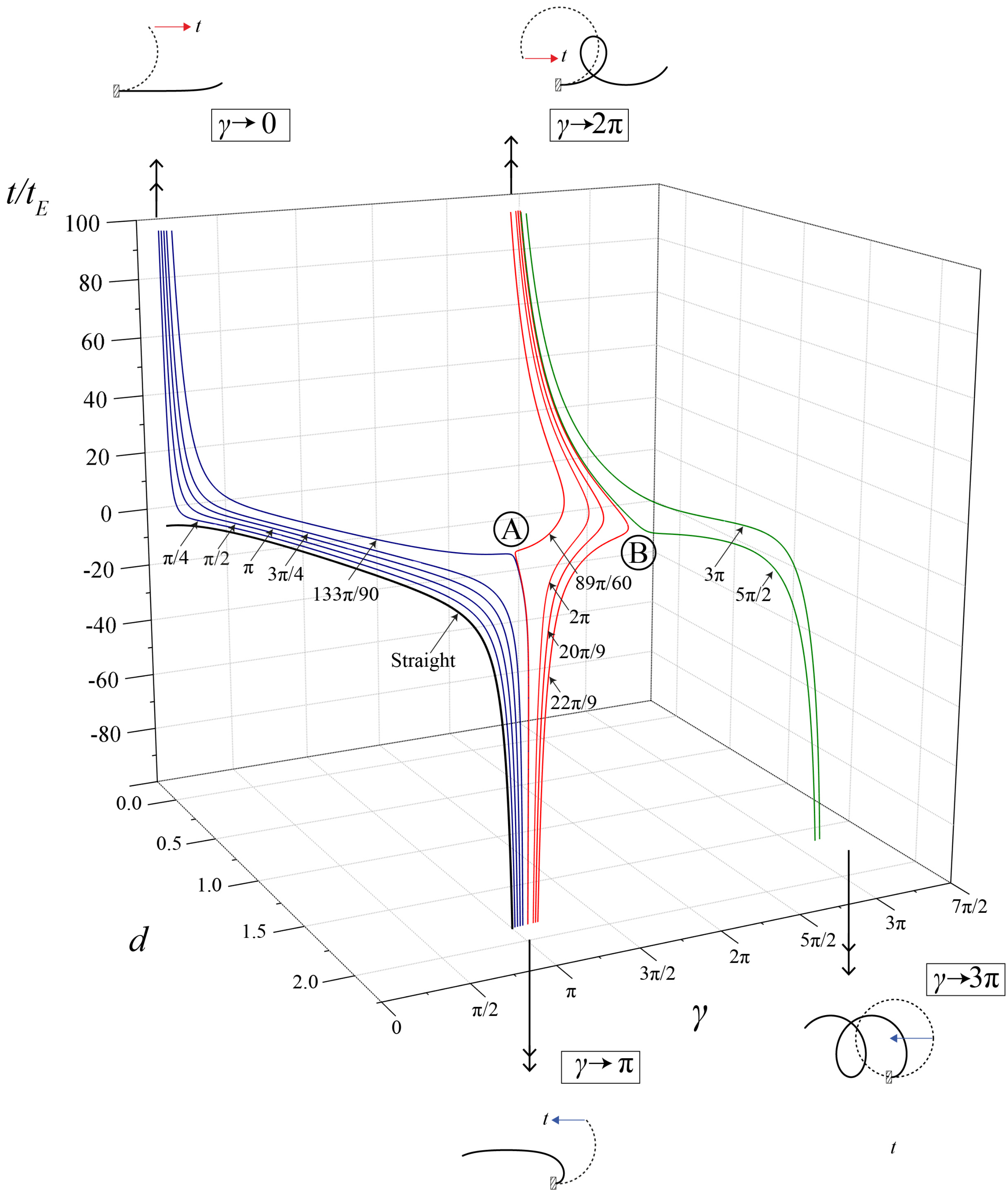

Figure 3.13: A 3-Dimensional $td\gamma$ plot for different values of γ_i (red, blue and green loading paths), along with the loading path for the straight rod (shown in black). The divergence in the γt plane arises because of the formation and existence of loops. In the case of an initially straight rod there is a bifurcation at $\frac{t}{t_E} = -1$ and γ varies from 0 to π.

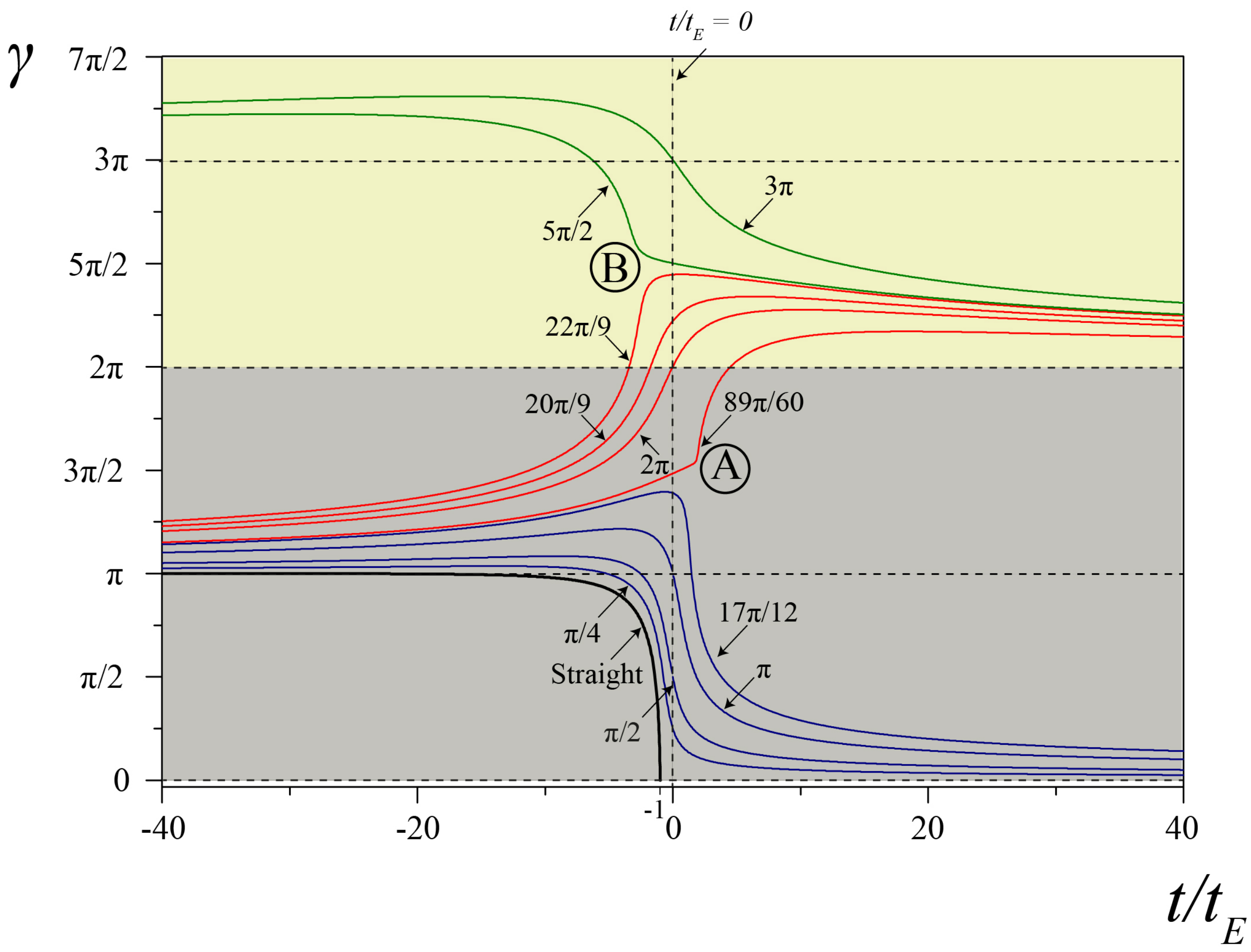

Figure 3.14: A plot showing the function $\gamma(t)$ for a rod with different values of uniform intrinsic curvature. The blue paths denote the deformed shapes that have no loop for both $t > 0$ and $t < 0$. The red paths indicate the deformed shapes that have a loop for $t > 0$ only and the green paths represent those shapes that have a loop under both $t > 0$ and $t < 0$. The yellow and grey shaded regions correspond to deformed shapes where solutions with and without a loop exist, respectively.

We now derive expressions for $\dot{\gamma}_i$ and $\ddot{\gamma}_i$ and apply those to Eq. 3.3. For this we split and integrate Eq. 2.64 as follows:

$$1 = \int_0^{\gamma} \frac{\mathrm{d}\psi}{\Big(\gamma_i^2 - 2t(\cos(\psi) - \cos(\gamma))\Big)^{1/2}}. \tag{3.10}$$

We differentiate Eq. 3.10 with respect to t and note that $\gamma = \gamma(t)$. If there is a function $F(\psi, t)$ that is continuous and differentiable in both t and ψ then according to Leibniz's Integral rule:

$$\frac{\mathrm{d}}{\mathrm{d}t} \int_0^{\gamma(t)} F(\psi, t)\mathrm{d}\psi = \int_0^{\gamma(t)} \frac{\partial F(\psi, t)}{\partial t}\mathrm{d}\psi + F(\gamma(t), t)\frac{\mathrm{d}\gamma(t)}{\mathrm{d}t}. \tag{3.11}$$

Applying Eq. 3.11 to Eq. 3.10 we obtain:

$$\frac{\mathrm{d}\gamma}{\mathrm{d}t} = -\gamma_i \int_0^{\gamma} \mathrm{d}\psi \frac{(\cos(\psi) - \cos(\gamma) + t\sin(\gamma)\frac{\mathrm{d}\gamma}{\mathrm{d}t})}{\Big(\gamma_i^2 - 2t(\cos(\psi) - \cos(\gamma))\Big)^{3/2}}. \tag{3.12}$$

Additionally, we apply Eq. 3.11 to Eq. 3.12 and find:

$$\begin{aligned} \frac{\mathrm{d}^2\gamma}{\mathrm{d}t^2} = & -\gamma_i \int_0^{\gamma} \mathrm{d}\psi \Bigg[\frac{\Big(2\sin(\gamma)\frac{\mathrm{d}\gamma}{\mathrm{d}t} + t\cos(\gamma)(\frac{\mathrm{d}\gamma}{\mathrm{d}t})^2 + t\sin(\gamma)\frac{\mathrm{d}^2\gamma}{\mathrm{d}t}\Big)}{\Big(\gamma_i^2 - 2t\big(\cos(\psi) - \cos(\gamma)\big)\Big)^{3/2}} + \\ & + \frac{3\Big(\cos(\psi) - \cos(\gamma) + t\sin(\gamma)\frac{\mathrm{d}\gamma}{\mathrm{d}t}\Big)^2}{\Big(\gamma_i^2 - 2t\big(\cos(\psi) - \cos(\gamma)\big)\Big)^{5/2}} \Bigg] - \frac{t}{\gamma_i^2}\sin(\gamma)\Big(\frac{\mathrm{d}\gamma}{\mathrm{d}t}\Big)^2. \end{aligned} \tag{3.13}$$

In order to determine Eq. 3.4 and Eq. 3.5 we set $t = 0$ in Eqs. 3.12−3.13 and integrate as follows (we should remark that in the case of $\ddot{\gamma}_i$, we use the identity

$\cos^2\psi \equiv \frac{1}{2}\cos(2\psi) + \frac{1}{2}$:

$$\begin{aligned}
\dot{\gamma}_i &= -\gamma_i \int_0^{\gamma_i} \frac{\cos(\psi) - \cos(\gamma_i)}{\gamma_i^3}\,\mathrm{d}\psi \\
&= -\frac{1}{\gamma_i^2}\Big(\sin(\gamma_i) - \gamma_i\cos(\gamma_i)\Big) && (3.14) \\
\ddot{\gamma}_i &= -\gamma_i \int_0^{\gamma_i} \mathrm{d}\psi \left(\frac{2\sin(\gamma_i)\dot{\gamma}_i}{\gamma_i^3} + \frac{3\big(\cos^2(\psi) - 2\cos(\psi)\cos(\gamma_i) + \cos^2(\gamma_i)\big)}{\gamma_i^5}\right) \\
&= -\gamma_i \int_0^{\gamma_i} \mathrm{d}\psi \left[\frac{2}{\gamma_i^3}\sin(\gamma)\dot{\gamma}_i + \frac{3}{\gamma_i^5}\Big(1 + \frac{1}{2}\cos(2\psi) - 2\cos(\psi)\cos(\gamma_i) + \frac{1}{2} + \cos(2\gamma_i)\Big)\right] \\
&= -\gamma_i \left[\frac{2}{\gamma_i^3}\sin(\gamma_i)\dot{\gamma}_i\gamma_i + \frac{3}{\gamma_i^5}\left(\gamma_i + \frac{1}{4}\sin(2\gamma_i) - 2\sin(\gamma_i)\cos(\gamma_i)\right.\right. \\
&+ \left.\left.\frac{1}{2}\cos(2\gamma_i)\gamma_i\right)\right]. && (3.15)
\end{aligned}$$

We substitute Eq. 3.14 into the last of Eq. 3.15, and use the identity $\sin(2\gamma_i) \equiv 2\sin(\gamma_i)\cos(\gamma_i)$ as follows:

$$\ddot{\gamma}_i = \frac{2}{\gamma_i^3}\sin^2(\gamma_i) - \frac{1}{\gamma_i^2}\sin(2\gamma_i) - \frac{3}{\gamma_i^3} - \frac{3}{4\gamma_i^4}\sin(\gamma_i) - \frac{3}{2\gamma_i^3}\cos(2\gamma_i). \quad (3.16)$$

Where, $\sin^2\gamma_i = \frac{1}{2}(1 - \cos(2\gamma_i))$ and Eq. 3.16 can be re-written as follows:

$$\ddot{\gamma}_i = \frac{1}{\gamma_i^2}\sin(2\gamma_i)\Big(\frac{9}{4\gamma_i^2} - \frac{1}{\gamma_i^2}\Big) - \frac{2}{\gamma_i^3} - \frac{5}{2\gamma_i^3}\cos(2\gamma_i). \quad (3.17)$$

We should remark that this work has been published in our paper [20]. A plot of the derivatives $\dot{\gamma}$ and $\ddot{\gamma}$, that is Eqns. 3.14 and 3.17, is depicted Figure 3.15 and the open and closed circles denote the formation of loops for a rod under a tensile and compressive force respectively. The formation of loops under a tensile force requires both $\dot{\gamma}$ and $\ddot{\gamma}$ to be > 0, whereas the formation of loops for a rod under a compressive force requires $\dot{\gamma} < 0$ and $\ddot{\gamma} > 0$.

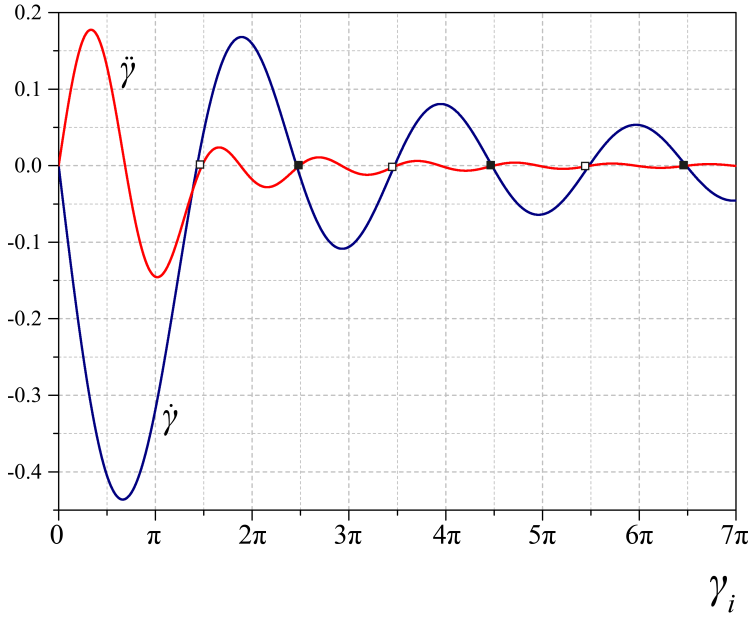

Figure 3.15: An approximation of the first and second derivative of the function $\gamma(t)$ around an infinitesimal force $|t| \ll 1$. The open squares and the closed squares denote the formation of loops under a tensile and compressive force respectively.

Table 3.1 shows the approximate values of γ^c and γ^t for loop formation that are found as a result of the above analysis.

Number of loops n	**Tension** γ_n^t	**Compression** γ_n^c
1	266^o	448^o
2	628^o	808^o
3	989^o	1169^o

Table 3.1: An approximation of the value of initial uniform curvature where loop formation subsequently occurs.

The approximate values for the formation of a single loop, see Table 3.1 are in good agreement with the experiments, see Figures 3.7 and 3.8.

3.4 Results: Case II LHP

The theoretical equilibrium paths and experimental data points that correspond to a rod with different values of intrinsic curvature in the LHP are presented. The theoretical loading paths are depicted in Figure 3.16 and the experimental data are shown in Figures 3.18−3.21.

The theoretical loading paths presented in Figure 3.16 correspond to loading paths for a straight and uniformly curved rod in both the UHP and LHP, see the black, blue and orange equilibrium paths respectively. The positions of the tip of the unstressed rod d_i is represented with white filled circles. Note that the reference configuration of those rods lie in the UHP. The shapes in the UHP are deformed from the unstressed configuration, i.e., $t = 0$, whereas the solutions in the LHP have to be moved into the LHP and then loaded. Consequently those paths do not cross the $x-$axis. The loading paths which correspond to deformed shapes that lie in the LHP (orange paths) are qualitatively different to those that lie in the UHP. We observe that one value of $\frac{t}{t_E}$ can give two different values of d and vice versa. Certain values of γ_i approach the limit $d = 0$ and as the curvature in the rod is increased, the corresponding loading paths move away from the limit $d = 0$.

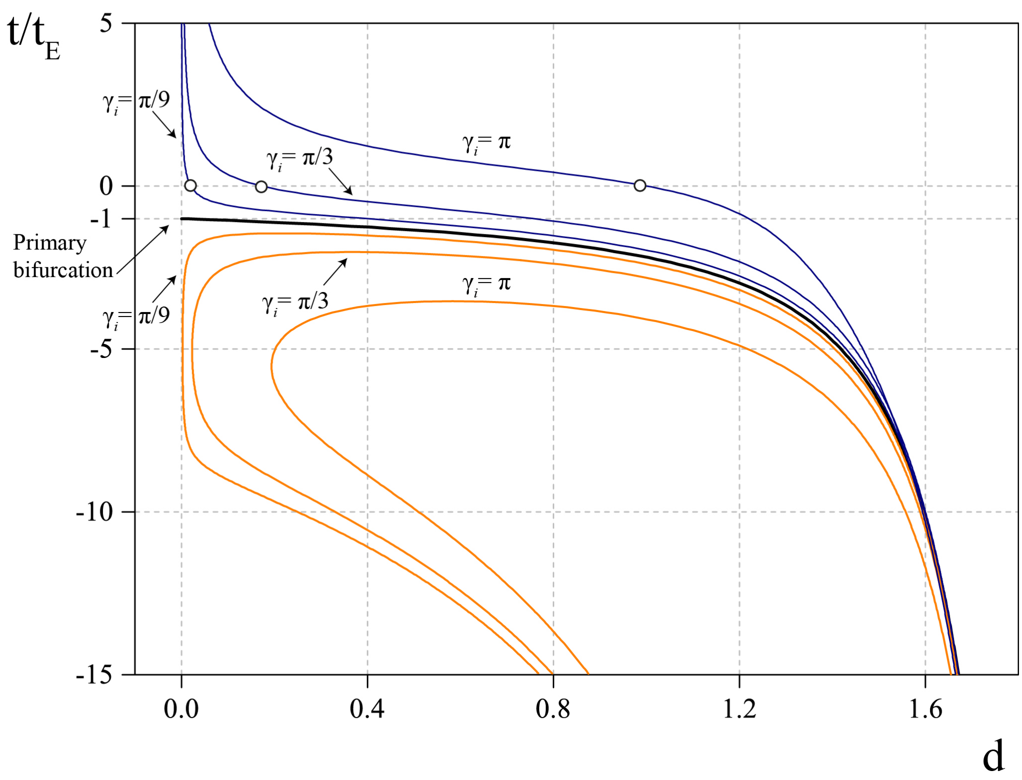

Figure 3.16: The loading diagram for an initially uniformly curved rod rod that is situated in the UHP and LHP see blue and orange loading paths respectively. The paths that correspond to rods that are deformed in the UHP cross the horizontal axis, i.e., $t = 0$, and are denoted with white filled circles. The loading paths for rods that are situated in the LHP do not cross $t = 0$.

The theoretical loading paths along with the experimental data for a rod with uniform curvature is presented in Figures 3.18−3.21. The blue dashed and the orange continuous lines in those Figures correspond to deformed shapes in the UHP and LHP respectively. The red and blue crosses denote experimental data that corresponds to deformed shapes in the UHP and LHP respectively.

The unstressed uniformly curved rod lies in the UHP (see white filled circle in Figures 3.18−3.21). A rod is defined as being in the LHP if a bending moment that is opposite to the rods intrinsic curvature is applied. The rod is held in equilibrium with a load (for example see point (a) in Figures 3.18−3.21). The weights are incrementally removed (see point (b) and (c) in Figures 3.18−3.21). A point is then reached whereby the rod becomes unstable, i.e., if an increment of load is removed the rod loses the inflection point and "jumps", such that it takes an equilibrium form whereby it has no apparent inflection point. At this point the rod is defined in the UHP. Note that the rod remains in the UHP (see d,e,f in Figures 3.18−3.21). If from that state the rod is loaded or unloaded, the loading path either approaches $d = 2$ or $d = d_i$ respectively. A rod that lies in the UHP does not have an inflection point along its length and cannot return to the LHP under an axial load. For the case where $\gamma_i \approx \pi/9$ (see Figure 3.18) the loading path (orange path) approaches $d = 0$ in the limit. The loading path where $d \to 0$, corresponds to a "nearly" straight configuration and obtaining those solutions using this experimental procedure is not possible. For higher values of γ_i, see Figures 3.19−3.21, the gap between the limit ($d = 0$) and the loading paths increases.

The experimental transition between the LHP and UHP is denoted by the black arrows, and for increased values of γ_i the "gap" between the loading paths of the UHP and LHP increases, see Figures 3.18−3.21. Experimentally the rod undergoes a sudden large deformation across to the other half plane, i.e., UHP. The description we have given on the transition between the LHP and UHP holds for all the experimental data that we have presented. We found reporting on experiments where the curvature was greater than $\frac{23\pi}{18}$ challenging and this is because the number of inflection points increase. We show plots of $\frac{\mathrm{d}\phi}{\mathrm{d}s}$ vs. s

in Figure 3.17. Rods with uniform curvature in the range $0 < \gamma_i \leq \pi$ have one inflection point, see Figure 3.17, (a)-(c), and rods where the curvature is $\gamma_i \approx 2\pi$ have 4 inflection points, see Figure 3.17, (d). Experimentally, it is practical to validate those solutions that have one inflection point.

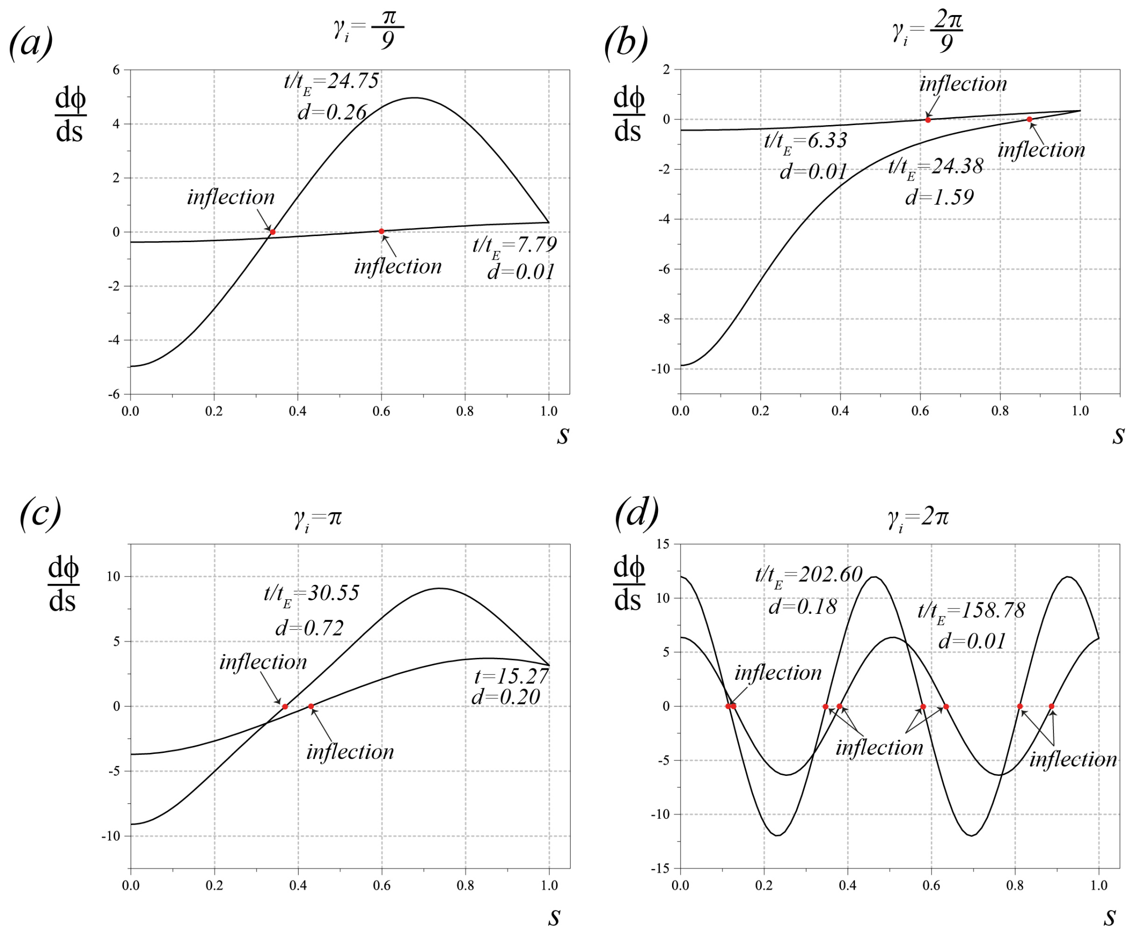

Figure 3.17: Plots of $\frac{\mathrm{d}\phi}{\mathrm{d}s}$ vs. s for a uniformly curved rod that is located in the LHP. The inflection points are denoted with red filled circles. Rods with values of curvature of $\gamma_i = 2\pi$ have four inflection points.

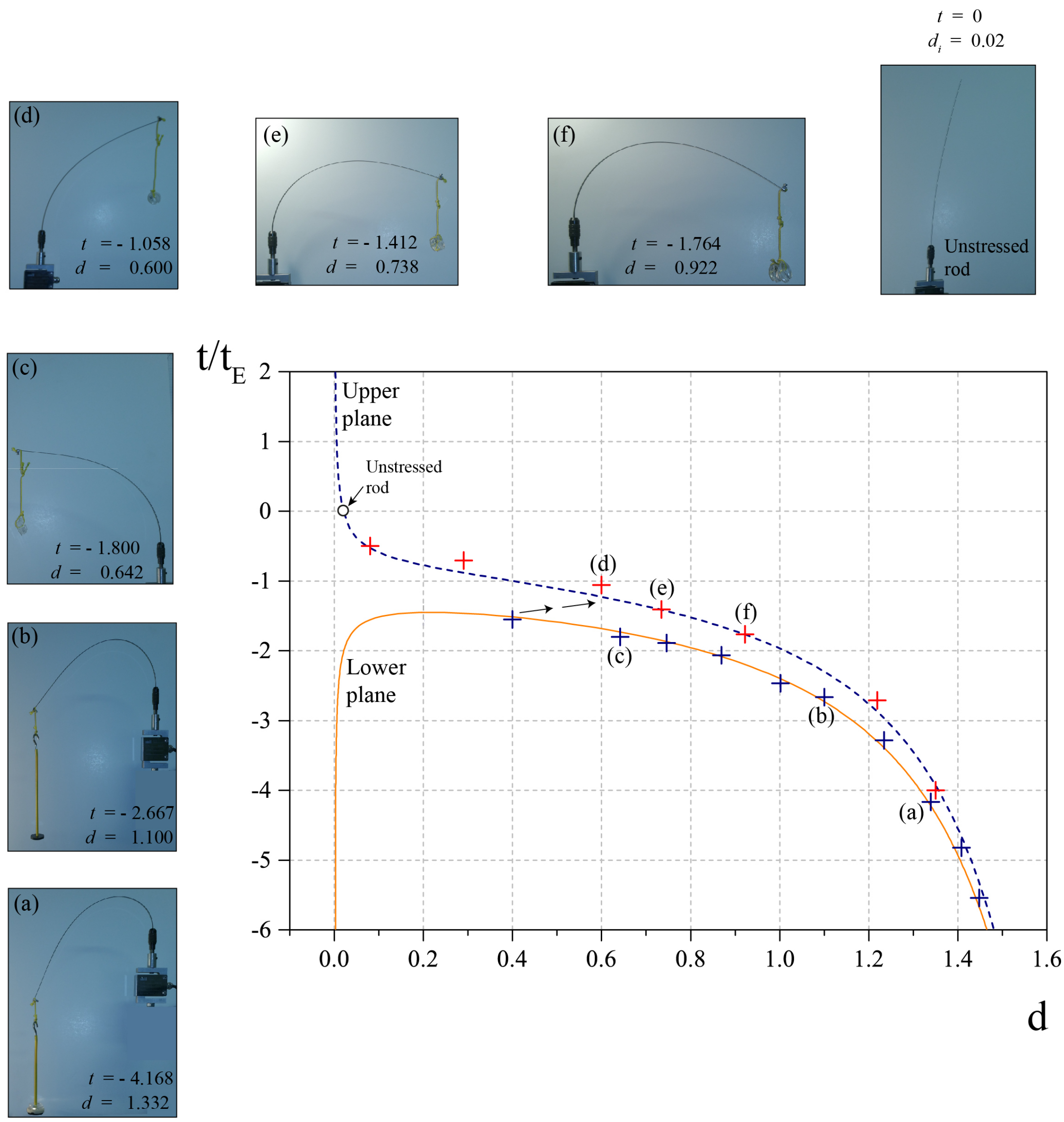

Figure 3.18: Experimental data for a rod with $\gamma_i = \frac{\pi}{9}$ in the LHP and UHP, see blue and red crosses respectively. The equilibrium loading paths that are obtained in AUTO are presented with solid and dashed lines, see orange and blue loading paths for a rod that is located in the LHP and UHP respectively. The rod is uniformly curved in its unstressed state (where $\gamma_i \approx \pi/9$) and the position of the unstressed rod is denoted by the white filled circle. For deformed shapes in the LHP where $d \to 0$, correspond to unstable shapes. Those cannot be realised experimentally.

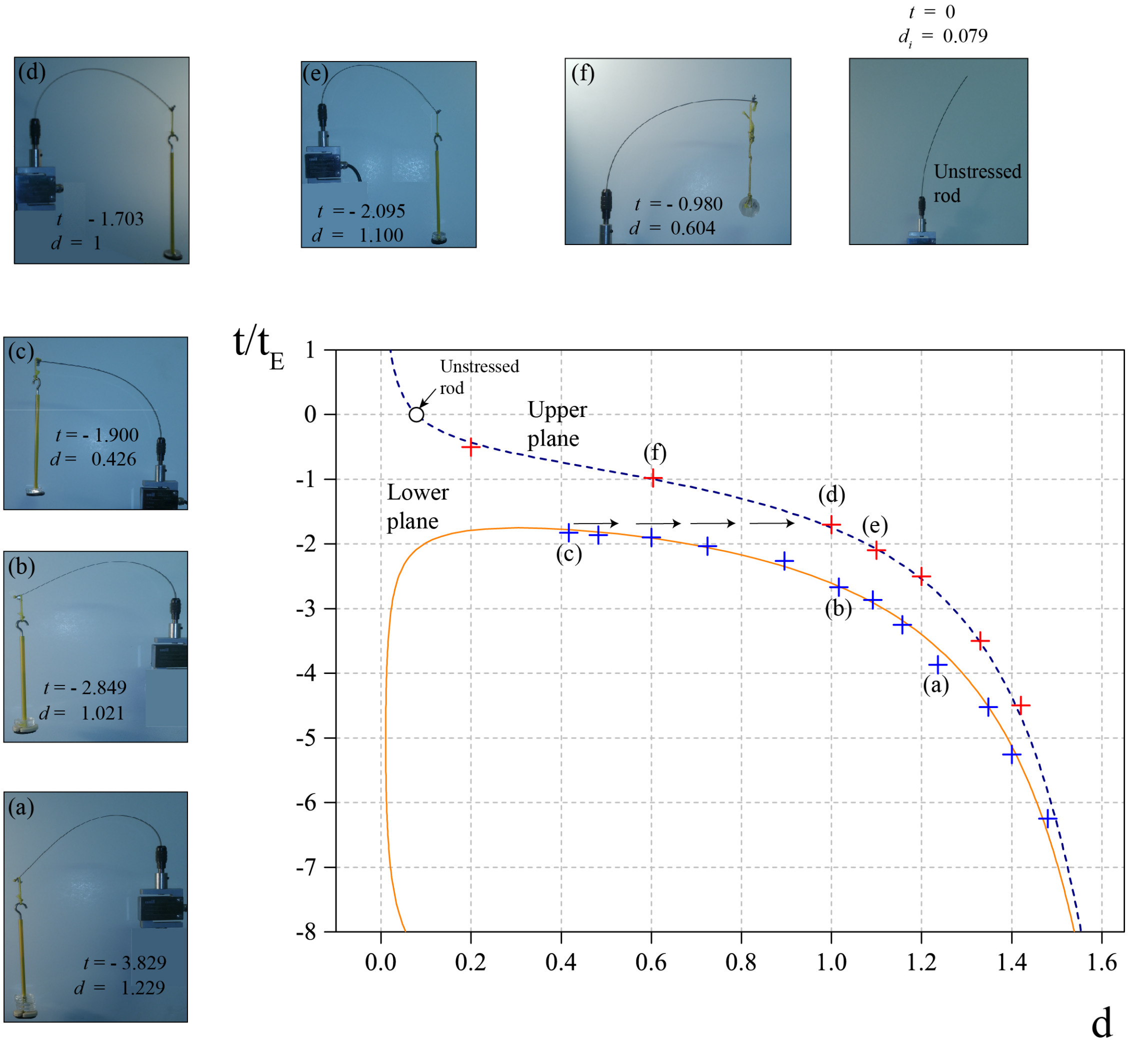

Figure 3.19: Experimental data for a rod with $\gamma_i = \frac{2\pi}{9}$ in the LHP and UHP, see blue and red crosses respectively. The equilibrium loading paths that are obtained in AUTO are shown with solid and dashed lines, see orange and blue loading paths for a rod that is located in the LHP and UHP respectively. The rod is uniformly curved in its unstressed state and the position of the unstressed rod is denoted by the white filled circle.

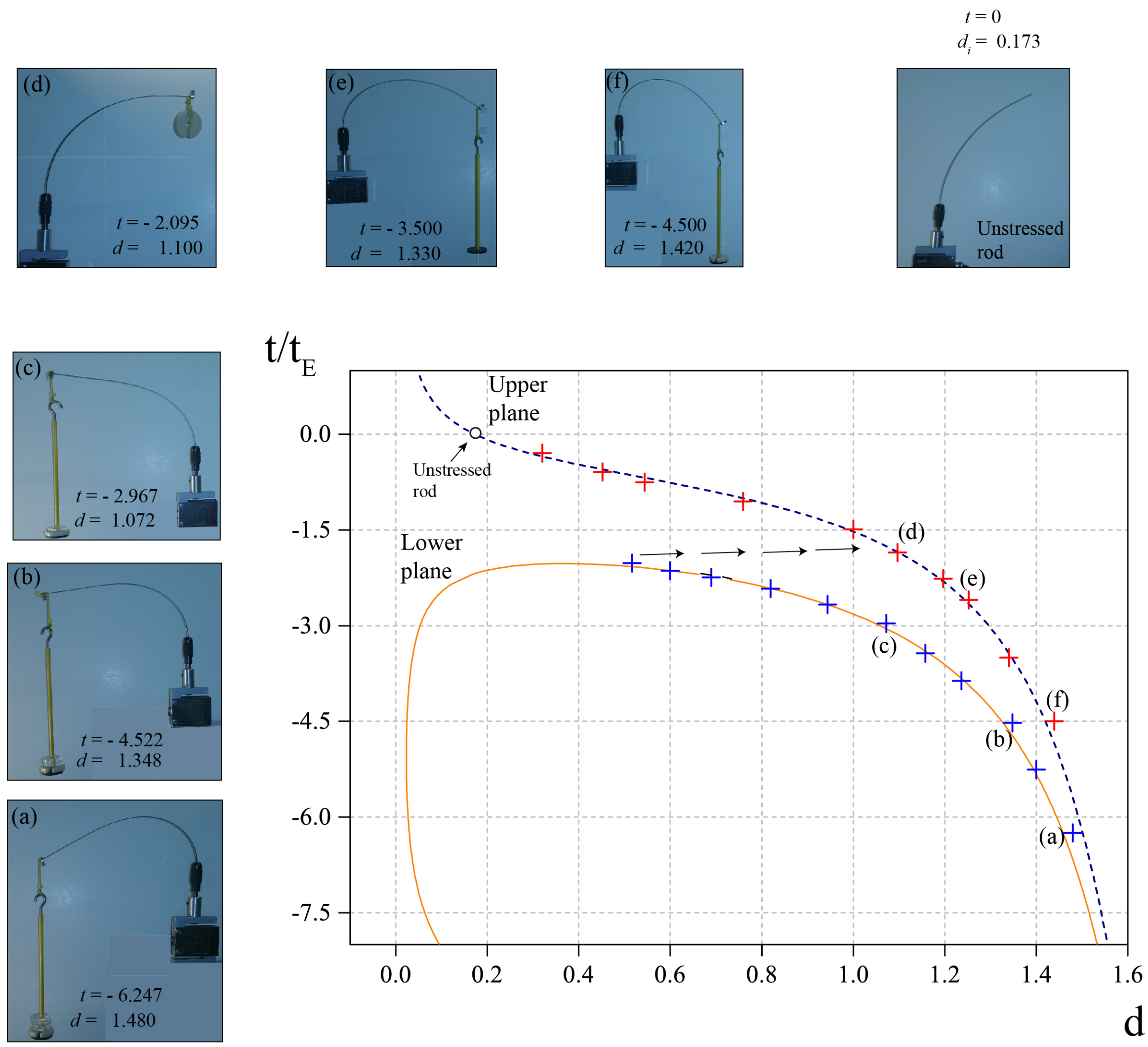

Figure 3.20: Experimental data for a rod with $\gamma_i = \frac{\pi}{3}$ in the LHP and UHP, see blue and red crosses respectively. The equilibrium loading paths that are obtained in AUTO are shown with solid and dashed lines, see orange and blue loading paths for a rod that is located in the LHP and UHP respectively. The rod is uniformly curved in its unstressed state and the position of the unstressed rod is denoted by the white filled circle. The angle of the unstressed rod at the tip is rad and the position of the unstressed rod is denoted by the white filled circle.

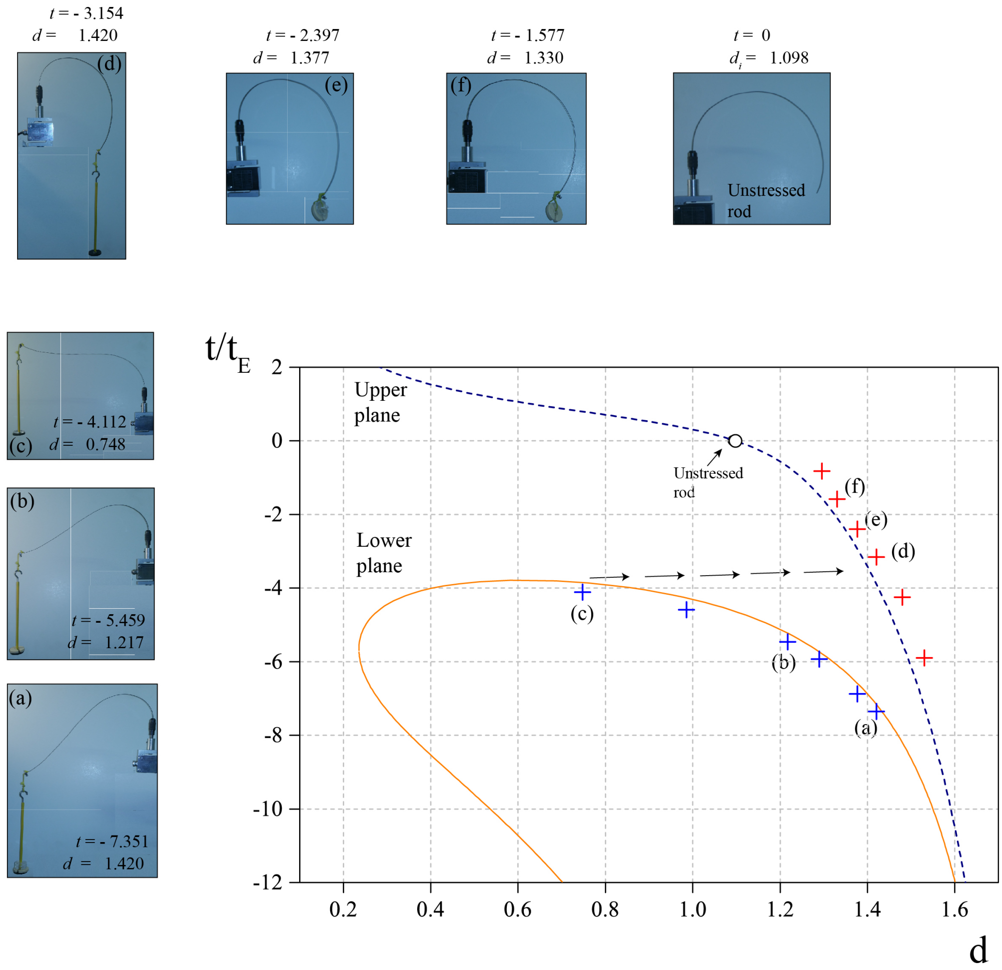

Figure 3.21: Experimental data for a rod with $\gamma_i = \frac{10\pi}{9}$ in the LHP and UHP, see blue and red crosses respectively. The equilibrium loading paths that are obtained in AUTO are shown with solid and dashed lines, see orange and blue loading paths for a rod that is located in the LHP and UHP respectively. The rod is uniformly curved in its unstressed state and the position of the unstressed rod is denoted by the white filled circle. The angle of the unstressed rod at the tip is rad and the position of the unstressed rod is denoted by the white filled circle.

Inspection of the equilibrium diagrams (both numerical and experimental) indicate that snap-through buckling phenomena will happen when $\frac{\mathrm{d}t}{\mathrm{d}d} = 0$. AUTO computes the loading path and explicitly identifies the snap-through buckling phenomena (as LP$-$limit points). Experimentally the rod becomes unstable and “jumps”. Experimental data corresponding to rods after the critical point cannot be obtained using our experimental procedure. We conclude that such solutions are unstable.

Note, that we do not vary d in our experiments but for consistency we plot the loading diagrams in terms of that parameter. For that reason it follows that we must find the critical points with respect to that variable.

In §3.4.1 we follow the numerical approach set out by [49], and determine those critical points, i.e., we find values of t and d at the instability point. Mathematically, those points correspond to values where $\frac{\mathrm{d}t}{\mathrm{d}d} = 0$, and it follows that we need to determine an expression for d. We need to know $\frac{\mathrm{d}t}{\mathrm{d}d}$, and not knowing the closed-form of $t = t(d)$ is not an impediment for determining $\frac{\mathrm{d}t}{\mathrm{d}d}$ as we shall show.

3.4.1 Critical points in uniformly curved rods

In this section we present the equations (in elliptic integral form) of the deformed rod in the LHP, and as far we know such solutions have not been reported in the literature. We then show the values of t and d that correspond to points of instability (limit points), i.e., $\frac{\mathrm{d}t}{\mathrm{d}d} = 0$

Deformed shapes that are located in the LHP have at least one inflection point located along the length of the rod. The parameters that are situated at that (inflection) point are denoted with an asterisk, see Figure 3.22. The equations for the geometry up to the inflection point $s = s^*$ and the tip $s = 1$ are presented in this section, i.e. $x(s^*)$, $y(s^*)$ and $x(1)$, $y(1)$ respectively. The expression for d involves $x(1)$ and is obtained from Eq. (5b) in Table 2.1.

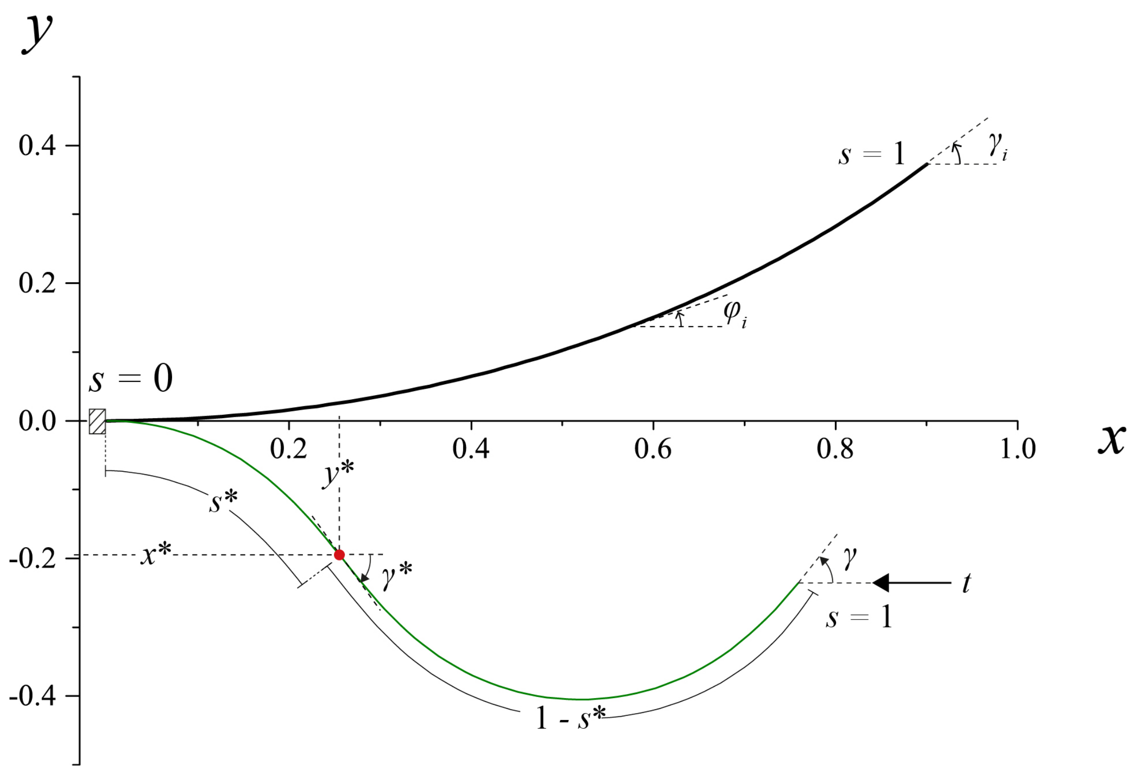

Figure 3.22: An unstressed uniformly curved rod (shown in black, where $\gamma_i = \pi/4$) along with a deformed rod (bent from the unstressed state and held with an applied compressive force) in the LHP. Deformed configurations in the LHP have atleast one inflection point and this is illustrated by presenting the associated parameters with an asterisk.

The equation for the arc length, up to the inflection point is given below:

$$\int_0^s \mathrm{d}u = -\frac{1}{2\,(-t)^{1/2}}\int_0^{\phi}\frac{\mathrm{d}\psi}{\left(p^{*2}-\sin^2\left(\frac{\psi}{2}\right)\right)^{1/2}}. \tag{3.18}$$

We convert Eq. 3.18 in to standard form. We refer back to Eq. 2.82 and find:

$$\mathrm{d}\psi = \mathrm{d}\theta\frac{2p^{*}\cos\left(\theta\right)}{\left(1-p^{2*}\sin^2\left(\theta\right)\right)^{1/2}}. \tag{3.19}$$

Eq. 3.18 is expressed as:

$$\begin{aligned} s &= \frac{1}{(-t)^{1/2}}\int_0^{\theta_\phi}\frac{\mathrm{d}\theta}{\left(1-p^{*2}\sin^2\theta\right)^{1/2}}, \\ &= \frac{1}{(-t)^{1/2}}F(\theta_\phi, p^{*}), \end{aligned} \tag{3.20}$$

where:

$$\theta_\phi \quad = \quad \arcsin\left(\frac{\sin\left(\frac{\phi}{2}\right)}{p^*}\right). \tag{3.21}$$

The equation for the x coordinate is given as follows:

$$\begin{aligned} x(s) &= \int_0^s \mathrm{d}u \cos(\phi(u)), \\ &= -\frac{1}{2(-t)^{1/2}} \int_0^\phi \frac{\mathrm{d}\psi \quad \cos(\psi)}{\left(p^{*2} - \sin^2(\psi/2)\right)^{1/2}}. \end{aligned} \tag{3.22}$$

We make use of the following identity:

$$\cos(\psi) = 2\cos^2\left(\frac{\psi}{2}\right) - 1 = 2\left(1 - \sin^2\left(\frac{\psi}{2}\right)\right) - 1 = 2\left(1 - p^{*2}\sin^2(\theta)\right) - 1, \tag{3.23}$$

and express Eq. 3.22 as follows:

$$x(s) \quad = \quad \frac{1}{(-t)^{1/2}}\left(\int_0^{\theta_\phi} \mathrm{d}\theta \;\; 2\left(1 - p^{*2}\sin^2(\theta)\right)^{1/2} \quad - \int_0^{\theta_\phi} \frac{\mathrm{d}\theta}{\left(1 - p^{*2}\sin(\theta)\right)}\right). \tag{3.24}$$

The equation for the y coordinate is presented as follows:

$$\begin{aligned} y(s) &= \int_0^s \mathrm{d}u \sin\left(\phi\left(u\right)\right), \\ &= -\frac{1}{2\left(-t\right)^{1/2}} \int_0^\phi \frac{\mathrm{d}\psi \quad \sin\left(\psi\right)}{\left(p^{*2} - \sin^2\left(\frac{\psi}{2}\right)\right)^{1/2}}. \end{aligned} \tag{3.25}$$

We use the following trigonometric identity,

$$\begin{aligned} \sin\left(\psi\right) &= 2\sin\left(\frac{\psi}{2}\right)\cos\left(\frac{\psi}{2}\right) = 2\sin\left(\frac{\psi}{2}\right)\left(1 - \sin^2\left(\frac{\psi}{2}\right)\right)^{1/2} \\ &= 2p^*\sin\left(\theta\right)\left(1 - p^{*2}\sin^2\left(\theta\right)\right)^{1/2} \end{aligned}$$

and determine the coordinate $y(s)$ as follows:

$$y(s) \quad = \quad \frac{2}{\left(-t\right)^{1/2}} \int_0^{\theta_\phi} p^*\sin\left(\theta\right)\mathrm{d}\theta = \frac{2p^*}{\left(-t\right)^{1/2}}\left(1 - \cos(\theta_\phi)\right) \tag{3.26}$$

To determine $x^* = x(s^*)$, $y^* = y(s^*)$ we set $\phi = \gamma^*$. It follows that $\theta_\phi = \frac{\pi}{2}$ and Eqs. 3.20, 3.24 and 3.25 become:

$$\begin{aligned} s^* &= \frac{1}{(-t)^{1/2}} K(p^*), &(3.27)\\ x^* &= \frac{1}{(-t)^{1/2}} \left(2E(p^*) - K(p^*)\right), &(3.28)\\ y^* &= \frac{2p^*}{(-t)^{1/2}}. &(3.29)\end{aligned}$$

We now present the equations for $s \in [s^*, 1]$:

$$\int_{s^*}^{s} \mathrm{d}u = \frac{1}{2(-t)^{1/2}} \int_{\gamma^*}^{\phi} \frac{\mathrm{d}\psi}{\left(p^* - \sin^2\left(\frac{\psi}{2}\right)\right)}. \tag{3.30}$$

We re-write Eq. 3.30 as follows:

$$s - s^* = -\frac{1}{(-t)^{1/2}} \int_{\pi/2}^{\theta_\phi} \frac{\mathrm{d}\theta}{(1 - p^{*2}\sin^2(\theta))^{1/2}}. \tag{3.31}$$

Similarly the equations for the coordinates x and y in the aforementioned region are presented as follows:

$$\begin{aligned} x(s) &= \int_0^{s^*} \mathrm{d}u \cos(\phi(u)) + \int_{s^*}^{s} \mathrm{d}u \cos(\phi(u)),\\ &= \frac{1}{(-t)^{1/2}} \left(4E(p^*) - 2K(p^*) - 2E(\theta_\phi, p^*) + F(\theta_\phi, p^*)\right), &(3.32)\\ y(s) &= \int_0^{s^*} \mathrm{d}u \sin(\phi(u)) + \int_{s^*}^{s} \mathrm{d}u \sin(\phi(u)),\\ &= \frac{2p^*}{(-t)^{1/2}} \left(\cos(\theta_\phi) + 1\right). &(3.33)\end{aligned}$$

We set $s = 1$ in Eqs. 3.31 3.33 and 3.32 and obtain $x = x(1)$ and $y = y(1)$,

$$\begin{aligned} 1 &= \frac{1}{(-t)^{1/2}} \left(2K(p^*) - F(\theta_\gamma, p^*)\right), &(3.34)\\ x(1) &= \frac{1}{(-t)^{1/2}} \left(4E(p^*) - 2K(p^*) - 2E(\theta_\gamma, p^*) + F(\theta_\gamma, p^*)\right), &(3.35)\\ y(1) &= \frac{2p^*}{(-t)^{1/2}} \left(1 + \cos(\theta_\gamma)\right). &(3.36)\end{aligned}$$

Where from Eq. 3.21 at $s = 1$, $\phi(1) = \gamma$ and

$$\theta_\gamma = \theta_\phi(1) = \arcsin\left(\frac{\sin\frac{\gamma}{2}}{p^*}\right) \tag{3.37}$$

Accordingly, we solve the following system of equations using FSOLVE in MATLAB:

$$\gamma_i^2 + 4tp^*\cos^2(\theta_\gamma) = 0, \tag{3.38}$$

$$\frac{1}{(-t)^{1/2}}K(p^*) - s^* = 0, \tag{3.39}$$

$$\frac{1}{(-t)^{1/2}}\left(2K(p^*) - F(\theta_\gamma, p^*)\right) - 1 = 0, \tag{3.40}$$

We solve Eqs. 3.38−3.40 for θ_γ, s^* and p^*, and where γ_i and t are input, i.e., uniform curvature and force. We should note that we could reduce the system and solve Eqs. 3.38 and 3.40 simultaneously for p^* and θ_γ, and then solve for s^* from Eq. 3.39.

We now proceed to obtain values where $\frac{\mathrm{d}t}{\mathrm{d}d} = 0$. We refer back to Eqs. 3.38−3.40 and set up the following system of equations:

$$U(t, p^*, \theta_\gamma) = \gamma_i^2 + 4tp^*\cos^2(\theta_\gamma) = 0, \tag{3.41}$$

$$V(t, p^*, \theta_\gamma) = \frac{1}{(-t)^{1/2}}\left(2K(p^*) - F(\theta_\gamma, p^*)\right) - 1 = 0, \tag{3.42}$$

$$\begin{aligned} W(d, t, p^*, \theta_\gamma) &= 1 - d - \frac{1}{(-t)^{1/2}}\Big(4E(p^*) \\ &- 2K(p^*) - 2E(\theta_\gamma, p^*) + F(\theta_\gamma, p^*)\Big) = 0. \end{aligned} \tag{3.43}$$

Eqs. 3.41 and 3.42 refer to the curvature at the inflection point and the total length of the rod respectively, and Eq. 3.43 is derived from Eq. 3.35 and condition (5b) in Table 2.1.

The derivatives of Eqs. 3.41−3.43 are,

$$\frac{\mathrm{d}U}{\mathrm{d}d} = \frac{\partial U}{\partial d} + \frac{\partial U}{\partial t}\frac{\mathrm{d}t}{\mathrm{d}d} + \frac{\partial U}{\partial \theta_\gamma}\frac{\mathrm{d}\theta_\gamma}{\mathrm{d}d} + \frac{\partial U}{\partial p^*}\frac{\mathrm{d}p^*}{\mathrm{d}d} = 0, \tag{3.44}$$

$$\frac{\mathrm{d}V}{\mathrm{d}d} = \frac{\partial V}{\partial d} + \frac{\partial V}{\partial t}\frac{\mathrm{d}t}{\mathrm{d}d} + \frac{\partial V}{\partial \theta_\gamma}\frac{\mathrm{d}\theta_\gamma}{\mathrm{d}d} + \frac{\partial V}{\partial p^*}\frac{\mathrm{d}p^*}{\mathrm{d}d} = 0, \tag{3.45}$$

$$\frac{\mathrm{d}W}{\mathrm{d}d} = \frac{\partial W}{\partial d} + \frac{\partial W}{\partial t}\frac{\mathrm{d}t}{\mathrm{d}d} + \frac{\partial W}{\partial \theta_\gamma}\frac{\mathrm{d}\theta_\gamma}{\mathrm{d}d} + \frac{\partial W}{\partial p^*}\frac{\mathrm{d}p^*}{\mathrm{d}d} = 0. \tag{3.46}$$

From Eqs. 3.44−3.46 we can show that:

$$\mathbf{J}\begin{pmatrix} \frac{\mathrm{d}t}{\mathrm{d}d} \\ \frac{\mathrm{d}\theta_\gamma}{\mathrm{d}d} \\ \frac{\mathrm{d}p^*}{\mathrm{d}d} \end{pmatrix} = -\begin{pmatrix} 0 \\ 0 \\ \frac{\partial W}{\partial d} \end{pmatrix} \tag{3.47}$$

where $\frac{\partial U}{\partial d}$ and $\frac{\partial V}{\partial d}$ are zero since $U(t, p^*, \theta_\gamma) = 0$ and $V(t, p^*, \theta_\gamma) = 0$, and the 3×3 matrix $\mathbf{J}$ is given by:

$$\mathbf{J} = \begin{pmatrix} \frac{\partial U}{\partial t} & \frac{\partial U}{\partial \theta_\gamma} & \frac{\partial U}{\partial p^*} \\ \frac{\partial V}{\partial t} & \frac{\partial V}{\partial \theta_\gamma} & \frac{\partial V}{\partial p^*} \\ \frac{\partial W}{\partial t} & \frac{\partial W}{\partial \theta_\gamma} & \frac{\partial W}{\partial p^*} \end{pmatrix}. \tag{3.48}$$

For convenience we denote the partial derivatives shown in Eq. 3.48 with a letter and a subscript. For example, we denote $\frac{\partial U}{\partial t} = U_t$, $\frac{\partial U}{\partial \theta_\gamma} = U_{\theta_\gamma}$ and so on. Then provided det $(\mathbf{J}) \neq 0$, where:

$$\begin{aligned} \det(\mathbf{J}) &= U_t(V_{\theta_\gamma}W_{p^*} - V_{p^*}W_{\theta_\gamma}) - U_{\theta_\gamma}(V_tW_{p^*} - V_{p^*}W_t) \\ &+ U_{p^*}(V_tW_{\theta_\gamma} - V_{\theta_\gamma}W_t), \end{aligned} \tag{3.49}$$

we find $\mathbf{J}^{-1}$. It then follows that:

$$\frac{\mathrm{d}t}{\mathrm{d}d} = \frac{-W_d(V_{\theta_\gamma}U_{p^*} - U_{\theta_\gamma}V_{p^*})}{\det(\mathbf{J})} \tag{3.50}$$

$$\frac{\mathrm{d}p^*}{\mathrm{d}d} = \frac{W_d(U_tV_{\theta_\gamma} - U_{\theta_\gamma}V_t)}{\det(\mathbf{J})} \tag{3.51}$$

$$\frac{\mathrm{d}\theta_\gamma}{\mathrm{d}d} = \frac{-W_d(U_tV_{p^*} - U_{p^*}V_t)}{\det(\mathbf{J})}. \tag{3.52}$$

The partial derivatives of U, V and W that are required to give the quantities in Eqs. 3.49−3.52 for $d \in [0,1]$ are presented. We should note that we make use of the book [50].

$$U_t = 4p^{*2}\cos^2(\theta_\gamma), \tag{3.53}$$

$$U_{p^*} = 8tp^*\cos^2(\theta_\gamma), \tag{3.54}$$

$$U_{\theta_\gamma} = -8tp^{*2}\cos(\theta_\gamma)\sin(\theta_\gamma), \tag{3.55}$$

$$V_t = \frac{1}{2(-t)^{3/2}}\left(2K(p^*) - F(\theta_\gamma, p^*)\right), \tag{3.56}$$

$$\begin{aligned} V_{p^*} &= \frac{1}{(-t)^{1/2}}\left\{\frac{1}{p^*p^{*2\prime}}\Big(2E(p^*) - E(\theta_\gamma, p^*) + p^{*2\prime}F(\theta_\gamma, p^*) - 2p^{*2\prime}K(p^*)\right. \\ &+ \left.\frac{p^{*2}\sin(\theta_\gamma)\cos(\theta_\gamma)}{(1-p^{*2}\sin^2(\theta_\gamma))^{1/2}}\right\}, \end{aligned} \tag{3.57}$$

$$V_{\theta_\gamma} = \frac{-1}{\left(-t\left(1-p^{*2}\sin^2(\theta_\gamma)\right)\right)^{1/2}}, \tag{3.58}$$

$$W_t = \frac{-1}{2(-t)^{3/2}}\left(4E(p^*) - 2K(p^*) - 2E(\theta_\gamma, p^*) + F(\theta_\gamma, p^*)\right), \tag{3.59}$$

$$\begin{aligned} W_{p^*} &= \frac{-1}{(-t)^{1/2}}\left\{\frac{1}{p^*}\left(4E(p^*) - 2K(p^*) - 2E(\theta_\gamma, p^*) + F(\theta_\gamma, p^*)\right),\right. \\ &+ \left.\frac{1}{p^*p^{*2\prime}}\left(E(\theta_\gamma, p^*) - 2E(p^*) - \frac{p^{*2}\sin(\theta_\gamma)\cos(\theta_\gamma)}{(1-p^{*2}\sin^2(\theta_\gamma))^{1/2}}\right)\right\}, \end{aligned} \tag{3.60}$$

$$W_{\theta_\gamma} = \frac{-1}{(-t)^{1/2}}\left(\frac{1}{(1-p^{*2}\sin^2(\theta_\gamma))^{1/2}} - 2\left(1-p^{*2}\sin^2(\theta_\gamma)\right)^{1/2}\right), \tag{3.61}$$

where,

$$p^{*2\prime} = 1 - p^{*2}. \tag{3.62}$$

The values of p^* and θ_γ are solved for different values of $d \in [0,1]$, i.e., the system of Eqs. 3.41−3.43. Once those values are known, we can determine the derivatives that are shown in Eqs. 3.50−3.52, provided $\det(\mathbf{J}) \neq 0$. Those values involve solving Eq. 3.47.

Initial curvature, γ_i	d	t	d (experimental)	t (experimental)
$\pi/9$	0.22	-1.450	0.40	-1.55
$2\pi/9$	0.32	-1.75	0.41	-1.83
$\pi/3$	0.40	-2.02	0.51	-2.02
$10\pi/9$	0.58	-3.81	0.75	-4.11

Table 3.2: An approximation of the displacement d and force t where the rod in the LHP loses stability. The rod "jumps" and an inflection point is lost. The rod is then defined in the UHP.

The critical points $\frac{\mathrm{d}t}{\mathrm{d}d} = 0$ are depicted, along with data from experiments, in Table 3.2. We should note that the discrepancy between the analysis and the experimental data is due to not having smaller increments of weights. The analytical procedure for determining the snap-through buckling points will work for a rod with other values of curvature.

3.5 Conclusions

An intrinsically straight rod will buckle at the critical Euler Buckling Load (Eq. 2.45) from its reference state (where it lies along the x axis). The deformed shape immediately after buckling will have curvature that is assigned positive or negative depending on whether we take the appropriate sign in Eq. 2.64 (or Eq. 2.64). For the purpose of the analysis, we have defined intrinsic curvature as +ve and in its unstressed state, it lies in the UHP.

In general, for the case of an intrinsically straight rod, whether one considers the rod with +ve or −ve curvature is inconsequential because the configurations are symmetric about the x-axis. However, in the case of an intrinsically curved rod, the sign of curvature is important because the symmetry with respect to the x axis is broken. Also a rod with initial curvature can be loaded from its unstressed state such that its bent form has curvature of the same sign as its initial curvature, in this case the rod is in the UHP. Alternatively, it can be loaded with a $-$ve moment such that the deformed rod has curvature of the opposite sign to its initial curvature (and the rod is in the LHP), and in this case it has an inflection point, $s^* \in [0, 1]$.

Whereas all configurations discussed in this work that lie in the LHP are inflectional elastica, configurations in the UHP may be either inflectional or noninflectional. Unfortunately, one cannot distinguish from inspection of the shape of a bent rod in the UHP, either within an experimental or numerical context, whether it is part of a noninflectional or inflectional solution. This confusion is manifest in the value of the elliptic parameter p, see Eq. 2.67 and Figure 2.11, where it is apparent that the value of p can change such that $p > 1$ (noninflectional) or $p \leq 1$ (inflectional) through small changes in the term involving the ratio of intrinsic curvature γ_i with the force t. That added term does not appear in the elliptic modulus for solutions in the LHP. Unlike in the UHP where the inflection points are muddled, in the LHP the inflection points are interior to the rod, i.e., $s^* \in [0, 1]$.

In its unstressed state the uniformly curved rod lies in the UHP. Experimentally, we apply a bending moment which which acts opposite to the rod's initial curvature. Upon application of the bending moment, we give rise to an interior inflection point and the rod is located in what we call the LHP. To ensure that the rod remains in the LHP, we apply a weight at the tip of the rod. We then apply a force, T and measure the position of the tip rod $X(L)$. Observation of our experimental data show that at certain values of T, there is a large change in d, i.e., the rod "jumps" from the LHP and into the UHP. Experimentally, we observe unstable equilibrium points. We approximated the location of those critical points and this required that we derived closed-form solutions.

We have shown that for certain values of intrinsic curvature, γ_i, loops can form. From our experimental and numerical observations we find that the first case of loop formation arises for $\gamma_i \approx 267^o$ under increasing $t > 0$. We also observed that a loop formed for $\gamma_i \approx 448^o$ under increasing $t < 0$. Generally, for loop formation to occur we identified that the angle of the tip of the rod γ increases under applied $|t|$, see Figure 3.14. Consequently, we observe the importance of the function $\gamma(t)$ and approximate it around an infinitesimal force $0 \ll t$ using a Taylor series expansion. In order for the function $\gamma(t)$ to increase under applied $-t$, $\frac{\mathrm{d}\gamma}{\mathrm{d}t}$ and $\frac{\mathrm{d}^2\gamma}{\mathrm{d}t^2}$ must be negative and positive respectively. For loop formation under applied $+t$, the function $\gamma(t)$ increases when both $\frac{\mathrm{d}\gamma}{\mathrm{d}t}$ and $\frac{\mathrm{d}^2\gamma}{\mathrm{d}t^2}$ are positive. We find expressions for $\frac{\mathrm{d}\gamma}{\mathrm{d}t}$ and $\frac{\mathrm{d}^2\gamma}{\mathrm{d}t^2}$ from the governing equation (see Eq. 3.10) and plot those along with values of γ_i in Figure 3.15. The values of γ_i where the aforementioned conditions are satisfied correspond to critical values of uniformly curved rods. The points where $\frac{\mathrm{d}\gamma}{\mathrm{d}t}$ become negative, and $\frac{\mathrm{d}^2\gamma}{\mathrm{d}t^2}$ become positive are denoted with open squares and correspond to the value of γ_i where loop formation occurs under applied $-t$. The points where $\frac{\mathrm{d}\gamma}{\mathrm{d}t}$ and $\frac{\mathrm{d}^2\gamma}{\mathrm{d}t^2}$ become positive are denoted with open white squares and correspond to the value of γ_i where loop formation occurs under applied $+t$. We should remark that our approximation can be misleading for values of γ_i near the critical values, because we find that the conditions on $\frac{\mathrm{d}\gamma}{\mathrm{d}t}$ and $\frac{\mathrm{d}^2\gamma}{\mathrm{d}t^2}$ can be satisfied and loops do not form. Our approximation can be improved if we were to derive and include higher order terms. In conclusion we find that the values of γ_i that we found in Figure 3.15 are in close agreement with our experiments.

Chapter 4

Initially straight rods in contact

4.1 Introduction

In this chapter we compute the deformed shapes of an initially straight rod with ends that are clamped and free, respectively. The free end of the rod makes contact with a smooth, rigid plate as it is displaced towards the clamped end in a straight line, see Figure 4.1. The rigid plate, which is inclined at $\frac{\pi}{2} - \alpha$ radians from the x-axis, exerts a force f on the tip of the rod. The unstressed configuration of the rod is straight and the boundary conditions are given in (1) − (4) along with (5b) (see Table 2.1), note that $\gamma_i = 0$. We plot td loading paths, embracing the planar equilibrium configurations for stages whereby both the tip and a section of the rods length are in contact with the wall. We denote those as point and line contact respectively.

Problems of this type give rise to equilibrium shapes whereby either the tip of the rod is in contact or a section of the rod's length is in contact with the rigid plate. In this section we review the literature on rods that are in point and line

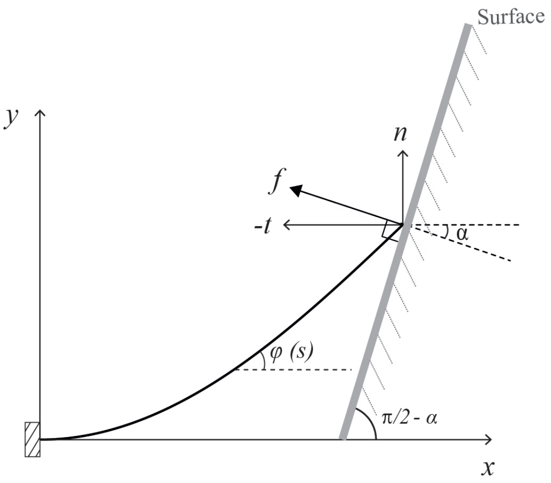

Figure 4.1: A nondimensional, clamped-free rod that is constrained by a flat plate. The surface exerts a force f on the tip of the rod. That force is exerted at an angle α.

contact, and this includes reviewing the work on rods that are deformed by loads which are applied at $0 \leq \alpha \leq \pi/2$.

The analytical solutions of an initially straight rod that is deformed by a load that is applied at $\alpha = 0$ i.e., an axial load, is one of the oldest problems [7], see [2] and [4] for a historical perspective. The book in [5], and the papers in [22] and [51] examine the cases for a rod that is loaded at an inclination of $\alpha = \pi/2, \alpha = 0$ and $0 < \alpha < \pi/2$, i.e., a normal, axial and inclined load respectively. The paper by the author of [22] shows the loading diagrams as a function of the end displacement and gives the analytical expression for the vertical displacement in terms of elliptic integrals. In chapter 2 of the book [5], the equations for the force and coordinates are given in terms of elliptic integrals. The authors tabulate the nondimensional values of t, $x(1)$ and $y(1)$ for the case where $\alpha = 0$. However, they do not give any loading plots nor do they give any deformed shapes. The problem of determining the configuration of a rod under the action of an inclined load, i.e., $0 < \alpha < \pi/2$, can be traced back to the work of [52], who published a treatise that was entirely devoted to the determination of deflection curves of clamped-free rods using elliptic integrals of the first and second types. A plethora of research on rods that are deformed by inclined loads have appeared since, see [53, 54]. The book in [6] examines the problem of a rod that is loaded at its free end by an inclined load. They give the equations for the load and the coordinates but do not give any numerical values. The authors of [51] address the same problem and published a method for obtaining all possible equilibrium configurations. They observe that there are multiple equilibrium configurations but provide no general conclusion, other than the number of possible equilibrium configurations depend on the value of the load. In fact, according to [53] an infinite number of equilibrium shapes exist, however [51] enumerate only seven. A study published in 2010 by the authors of [55] examine the same problem from which it is shown that for a specific load only one tip angle exists whereas for a specified tip angle several solutions exist, thus verifying the work of [51].

The problem of a rod that is in contact has previously been examined, for instance the authors of [23] examine the case of a clamped-clamped rod that is pressed against a flat, rigid plate. The authors compute the deformed shapes of the rod as it encounters point and line contact. They also show that if the displacement is input further a bifurcation occurs within the line contact region. They solve the problem using a shooting technique and they present the loading diagrams and deformed shapes. They do not conduct any experiments nor do they change the orientation of the plate. The paper by the authors of [56] carried out experiments on strips that were constrained by two rigid side walls. The side walls were placed parallel, either side of the unstressed rod. The rod was deformed under rigid loading, and upon input of end displacement the rod makes point and line contact with the one of the plates. The authors also find stable and unstable loading paths. They compare the loading diagrams that were obtained from experiments to those that were found using numerical methods. We should remark that although the author varied the height they did not alter the orientation of the side walls. The paper by the authors of [57] shows the deformed shapes and loading diagrams of a rod that is constrained by concave, convex and flat plates. Whilst the studies that we have mentioned above are useful for informing this research, they involve a different BVP i.e., the clamped-clamped rod.

The modelling of a rod in line contact with a rigid surface has practical applications to the off-shore engineering industry. Pipeline engineers are interested in the configuration of a pipeline whilst it comes into contact with the seabed. Their main concern is to avoid excessive curvatures and/or twisting of the pipeline, which could lead to permanent, expensive damage. The theory of rods has been applied to the laying [58] and the buckling of pipelines [59]. The authors of [60] published the first paper on pipeline buckling in 1974. They conducted experiments using stainless steel rods that were clamped at the ends. They induced internal oil pressure and showed the buckling of the pipe. [61] considers the buckling modes of pipelines using linear theory. The paper by [62] considers a pipeline that is lifted from the seabed with a mid-span force. The authors present numerical data for maximum deflection, bending moment at the lift off point and the reaction forces at the ends. However, they do not obtain the length of the contact region. Pertinent work on pipelines as BVPs can be found in [59, 63].

As we have pointed out from our review, the solutions to the rod that is deformed under an axial, normal and inclined load i.e., a rod that is in point contact, is not new and the equations are readily available. However there are no experimental investigations on clamped free rods that are deformed under a load that acts at an angle, i.e., in the range between $0 < \alpha < \pi/2$ nor is there any experimental work where both the transition between point and line contact occur.

An applicable scenario of the work we present in this chapter is that of whisker object interaction. The clamped end represents the whisker base (follicle) and the free end encounters contact with a rigid plate. Certain animals gather information, such as size and distance, by constantly tapping their whiskers against objects, see [64] and [65]. In the case of certain mammals, for example rats, a load-deflection relationship provides information about the surroundings, i.e., the whisker is a sensory device, connected to its neurological system. That form of tactile sensing has attracted considerable interest from researchers in robotics and neuroscience, see [66] and [67]. When a whisker makes contact with its surroundings, it bends, and this bending generates force and moments at the base of the whisker. Quantifying those mechanical variables when surfaces are of different orientation and location is of interest.

The study by the authors of [68] conduct experiments on whiskers whereby a normal force is applied along different locations along the length of the whisker. They plotted the load diagram and found that the slope of the loading paths are much steeper for loads that are applied near to the whisker base. If pressed further against a plate, a section of the whisker tends to establish line contact, providing further information on the shapes and textures of objects, see [69]. In order to quantify the mechanics and shed some light on the information elicited by the mechanoreceptors, researchers have applied both the linear and nonlinear model to the whisker. The paper by the author of [17] is one of the first published numerical models of the whisker. The authors investigate the dynamical behaviour of the whisker as it comes into contact with objects of different roughness. They apply the linear theory and analyse the frequency of the beam under the following events (boundary conditions): (a) the contact-free whisker (i.e., a clamped-free rod), (b) the whisker, as it is pushed against the object but not held rigidly, (i.e., a clamped-pinned rod) and (c) the whisker as it is pushed against the object and held rigidly, such that the slope at that end is fixed (i.e., a clamped-clamped rod). The authors conclude that texture identification could be facilitated by the whisker resonance properties. Similarly, [19] analysed the contact between the whisker tip and the object using linear theory. The model, formulated as a BVP, examined different surface roughnesses by inputting values for the coefficient of friction.

4.2 Experimental and numerical procedure

In this section we give details on the experimental and numerical procedure. Two qualitatively different solutions are determined. There are solutions whereby the only the tip of rod is in contact, and there are solutions whereby a section of the rod's length is in contact. The length of the contact region along the rod's length is assigned the parameter B_p. The nondimensional length is given by:

$$b = \frac{B_p}{L}. \tag{4.1}$$

As the plate is displaced along the X-axis, the tip of the rod ascends and the angle of the tip of the rod is in the range $0 < \gamma < \left(\frac{\pi}{2} - \alpha\right)$, see Figure 4.2(a). Upon further input of displacement, the rod reaches a situation whereby the angle of the tip of the rod is equal to the orientation of the plate, i.e., $\gamma = \left(\frac{\pi}{2} - \alpha\right)$, see Figure 4.2(b). This is a critical point whereby further input of displacement will result in a contact region that develops along the rods length. If the displacement is increased past this critical point, the parameter B_p increases, see Figure 4.2(c). Note that the position of the unstressed rod $D_i = 0$ and this holds for all experiments conducted in this chapter.

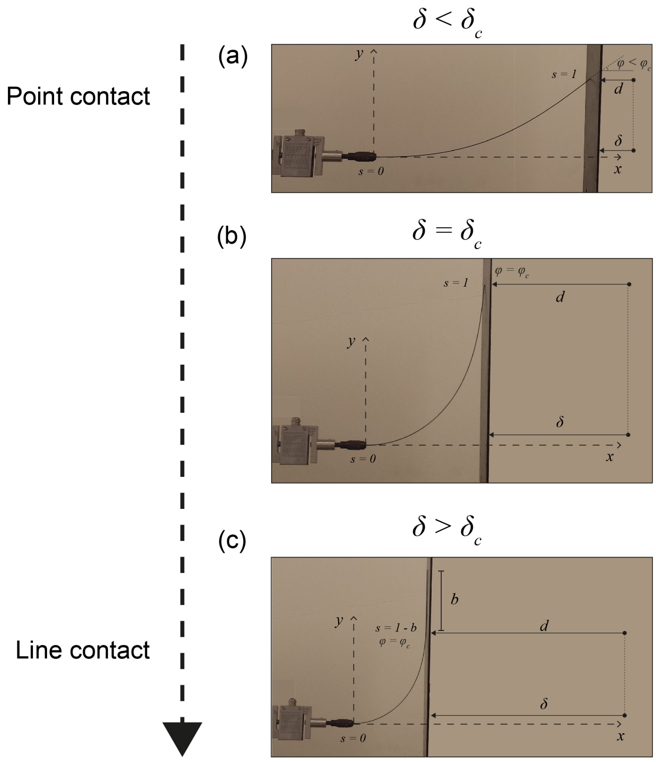

Figure 4.2: Photograph of a 1mm diameter nickel-titanium rod of length 300mm in point and line contact with the plate. (a) Upon input of displacement (of the surface) the rod is in point contact. If displaced further, the tangent of the deformed rod becomes parallel with the surface and this denoted a *critical* point (b) (transition between point and line contact). Upon further input of end displacement a section B_p, of the rods length lies flat on the surface i.e., line contact. We should note that in this photograph the surface is placed perpendicular to the X-axis, i.e., $\alpha = 0$.

4.2.1 Experimental procedure

The experimental set-up is depicted in Figure 4.3 and consists of a chuck, force transducer, potentiometer and a rigid surface. One end of the nitinol rod is clamped in the chuck and the other is free. The surface is fixed on to the machined casting, which is then attached on to the moveable base, at $X = L$. The potentiometer is attached to the rigid plate and the displacement is recorded as the plate is displaced along the X-axis towards the clamped end in a straight line.

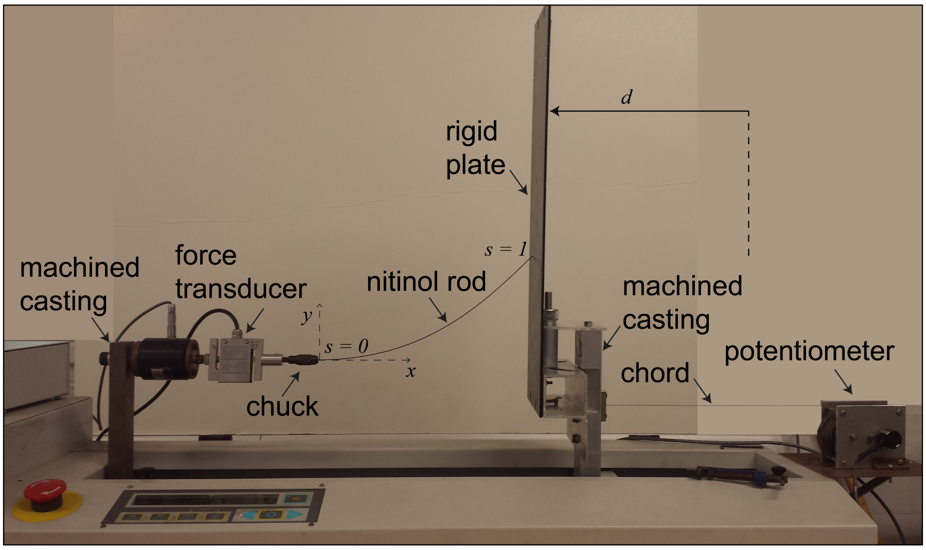

Figure 4.3: A clamped-free nitinol rod constrained by a flat, rigid, frictionless plate. The plate moves in a straight line parallel to the X-axis and first makes point and then line contact with the plate. We should remark that in these experiments we adopt initially straight rods and $D_i = 0$ for all cases.

The rigid plate is placed at the tip of the unstressed, straight rod, i.e., $X(L) = L$. The orientation of the plate is governed by the parameter, α and we define the perpendicular set-up as $\alpha = 0$. To begin with, we position the plate such that it is perpendicular to the X-axis i.e., $\alpha = 0$. We then input end displacement D and record values of F using the force transducer. We repeat for the case where $\alpha = \frac{\pi}{6}$. We then increase the angle α in increments of $\pi/12$ until $\alpha = \frac{5\pi}{12}$.

Experimentally it is practical to measure the displacement of the rigid plate and the parameters D and Δ refer to the displacement of the rod at the point of first contact and the rigid plate respectively, see Figure 4.4. The length $\Delta = \delta L$, and note that for the case when the rigid plate is positioned perpendicular to the

x axis i.e., $\alpha = 0$, the displacement of both the surface and the tip of the rod are equal, i.e., $\Delta = D$. Note that naturally we obtain values corresponding to Δ from our experiments, and that the following equations are applied to data obtained from non-experimental methods. The values of Δ are obtained as follows:

$$\Delta = L - X(L) + Y(L)\tan(\alpha) \qquad \text{for point contact,} \tag{4.2}$$

$$\Delta = L - X(L - B_p) + Y(L - B_p)\tan(\alpha) \qquad \text{for line contact.} \tag{4.3}$$

The first two terms in Eqns. 4.2 and 4.3 correspond to D (see Table 2.1) and the latter expression represents the length opposite to the angle α, shown in blue in Figure 4.4.

4.2.2 Numerical procedure

For numerical computation we follow [23] and introduce a re-scaling of the arc length. This is defined as:

$$z = \frac{s}{\lambda}, \qquad \lambda = 1 - b \tag{4.4}$$

The length of the rod in contact is b and z is the re-scaled arclength. Where $z \in [0, 1]\ \forall\ b$, and the governing Eqns., 2.35−2.39 are re-written as follows:

$$\frac{\mathrm{d}x}{\mathrm{d}z} = \lambda\cos(\phi), \tag{4.5}$$

$$\frac{\mathrm{d}y}{\mathrm{d}z} = \lambda\sin(\phi), \tag{4.6}$$

$$\frac{\mathrm{d}\phi}{\mathrm{d}z} = \lambda\kappa, \tag{4.7}$$

$$\frac{\mathrm{d}\kappa}{\mathrm{d}z} = \lambda\Big(r\cos(\alpha)\sin(\phi) - r\sin(\alpha)\cos(\phi)\Big), \tag{4.8}$$

$$\frac{\mathrm{d}r}{\mathrm{d}z} = 0. \tag{4.9}$$

In Figure 4.5 we show the steps of computation for this problem in AUTO. The BVP is set up in FORTRAN and the solutions are computed by varying the

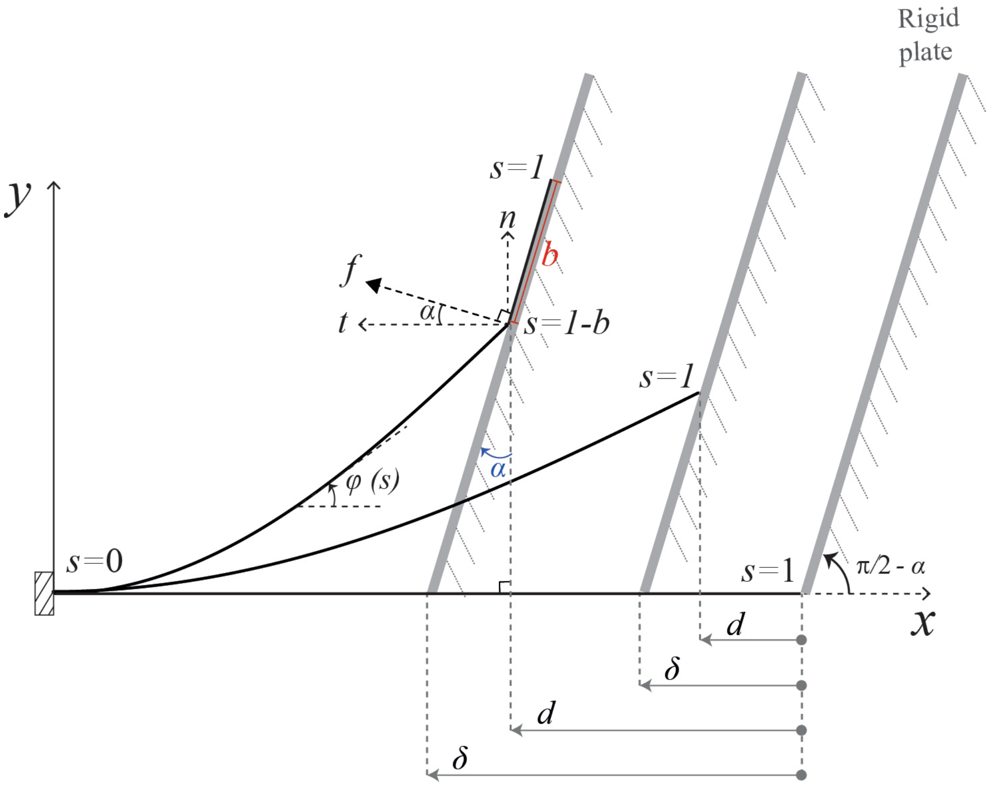

Figure 4.4: An unstressed nondimensional rod, plus two nondimensional rods in point and line contact with the plate. Distinction between the displacement of the surface δ and the tip of the rod d. In the experiments we displace the surface and record the corresponding displacement. In AUTO the rod is displaced from its initial, unstressed, straight state and we compute values of δ.

continuation parameter d. At d_{crit}, the angle of the tip of the deformed rod is equal to the inclination of the plate and AUTO is instructed to stop. We then enforce the condition $\phi(1) = \alpha$ and introduce the free parameter b, where $b > 0$ and $\lambda < 1$. We then proceed and compute the solutions that correspond to line contact.

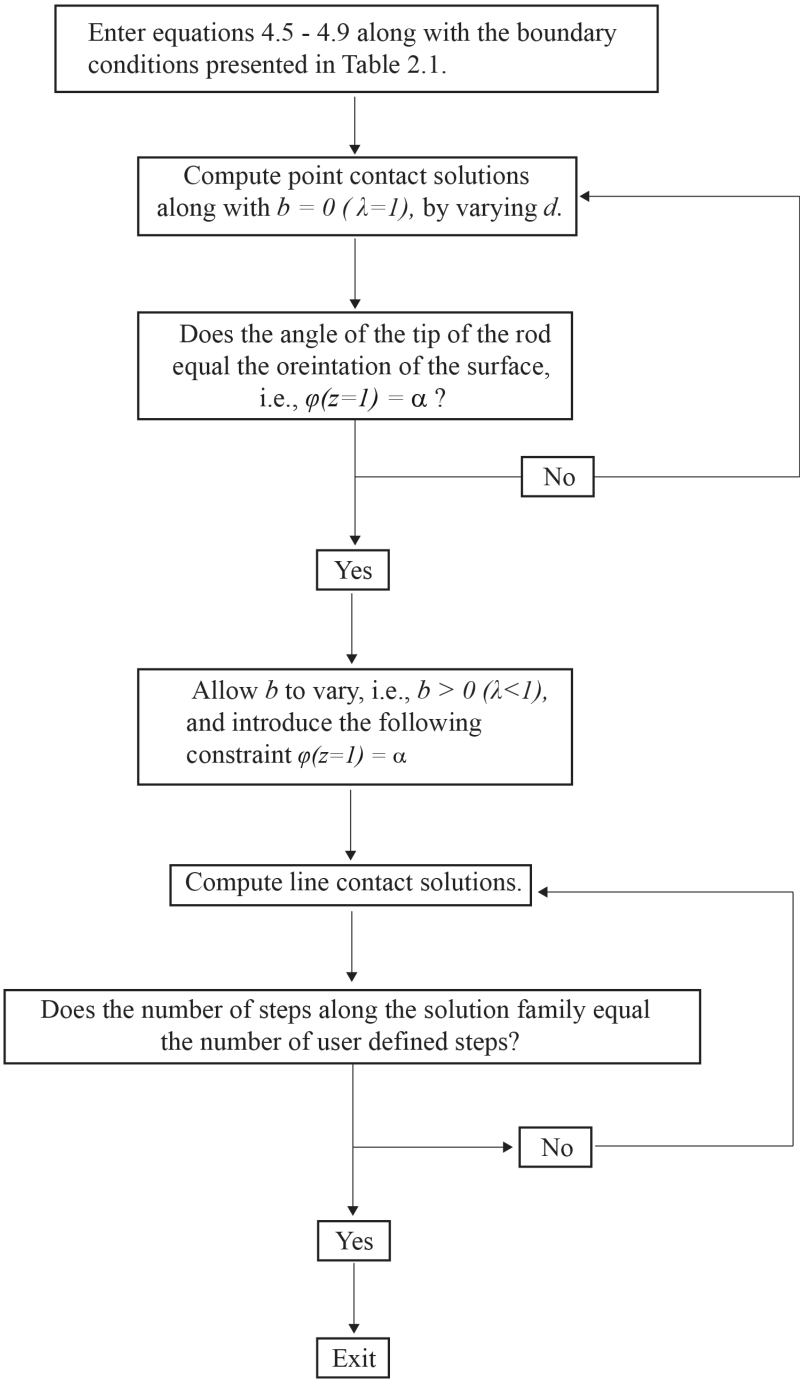

Figure 4.5: A flow chart showing the steps to compute the solutions in AUTO. Note, where $z \in [0,1] \forall\ b$ and $z = 1$ corresponds to the point of first contact. Note that we use Eqs. 4.2 and 4.3 to obtain values of δ.

4.3 Results

In this section we present the loading diagrams for a rod in point and line contact with the plate at different values of α. The loading paths presented in Figure 4.6 are obtained using the procedure outlined in Figure 4.5. For the case where the plate is positioned at $\alpha = 0$, a bifurcation occurs. For values of α near $\alpha = 0$, there is a rounding of the bifurcation, see for example the loading path for $\alpha = \frac{\pi}{180}$ in Figure 4.6. The loading paths for $\delta < \delta_c$ and $\delta > \delta_c$ are qualitatively different

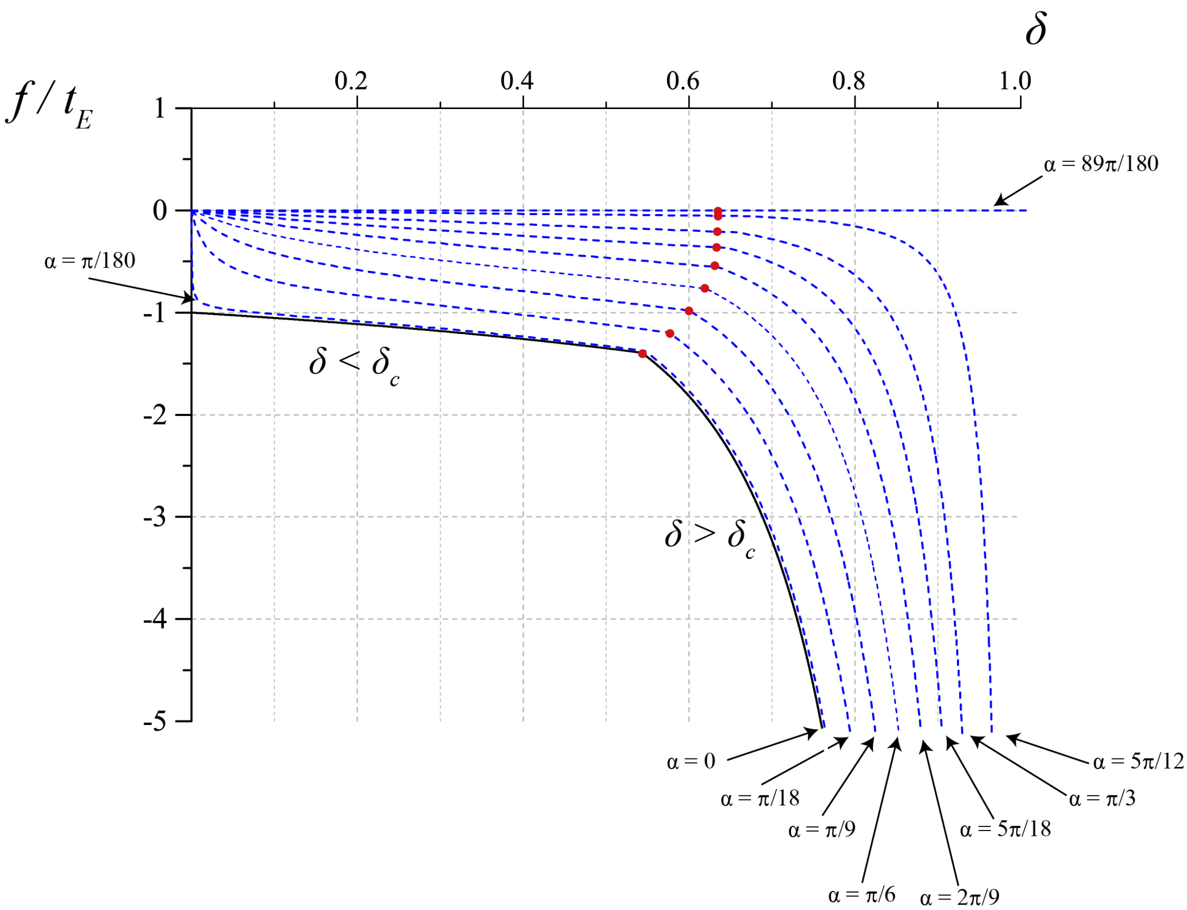

Figure 4.6: Theoretical loading paths for particular values of α. The solid black curve shows the path for $\alpha = 0$, a pure axial load, and the blue dashed curves correspond to a component of the inclined resultant force, f. The red filled circles denote the transition point i.e., δ_c. Generally as the angle α increases, the magnitude of the axial load approaches zero.

and are split at the critical point, red filled circles in Figure 4.6. In Figure 4.7 we present a plot of δ_c vs. $\alpha\forall$. For $\alpha = 0$, $\delta_c = 0.543$, and for $\alpha = \frac{89\pi}{180}$, $\delta_c = 0.0.667$. Generally the values of δ_c increase with increasing values of α.

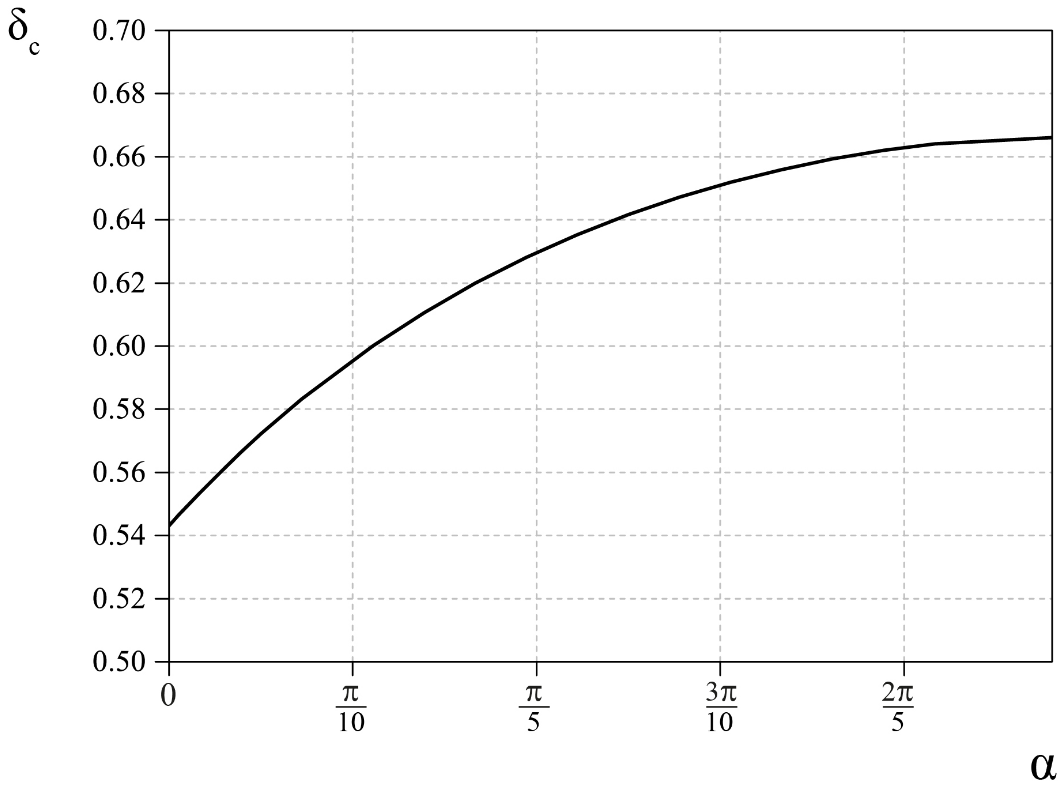

Figure 4.7: A plot of δ_c vs. $\alpha\forall$. The values of δ_c increase with increasing values of α.

We now present the deformed shapes for $\alpha = 0$ and $\alpha = \frac{\pi}{6}, \alpha = \frac{\pi}{4}, \alpha = \frac{\pi}{3}$ and $\alpha = \frac{5\pi}{12}$ in Figures 4.8−4.9 respectively.

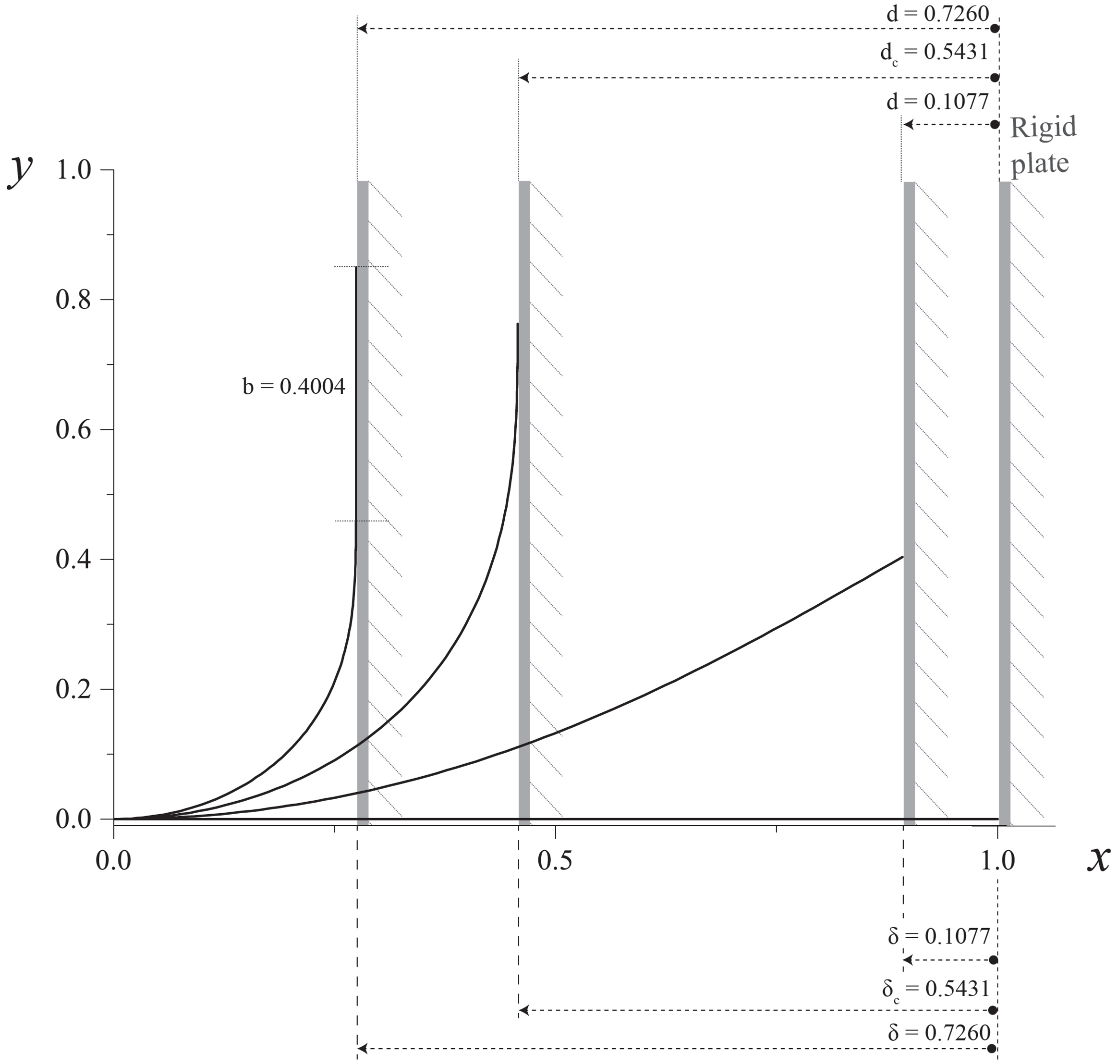

Figure 4.8: Three nondimensional bent configurations (plus the straight rod) where the plate is positioned at $\alpha = 0$. Those configurations correspond to $\delta < \delta_c$, $\delta = \delta_c$ and $\delta > \delta_c$. In the latter case, a section of the rod's of length $b = 0.4004$ is in line contact with the surface. Note for $\alpha = 0$, $\delta = d$.

(a)

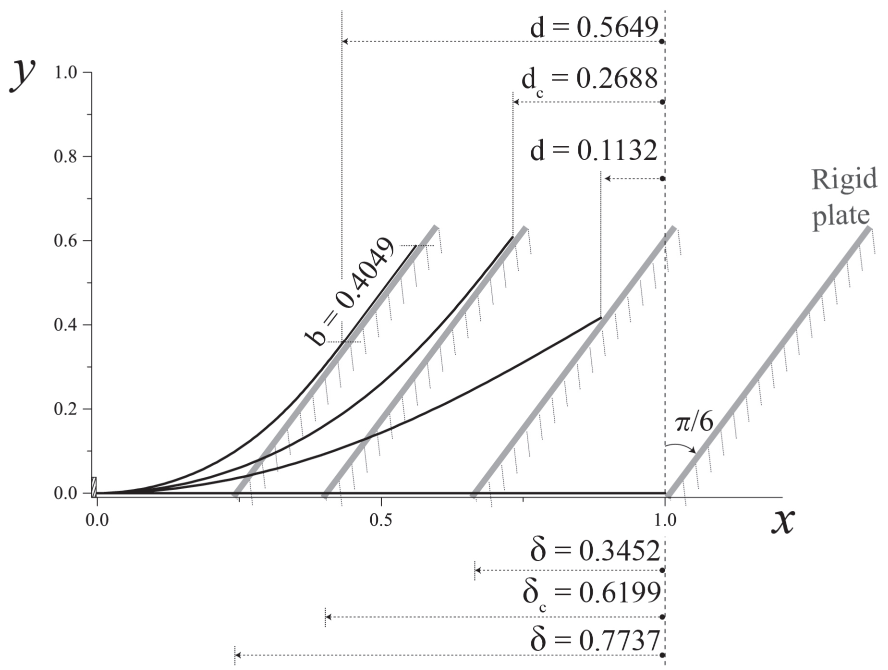
d = 0.5649
d_c = 0.2688
d = 0.1132
Rigid plate
b = 0.4049
π/6
y
x
1.0
0.8
0.6
0.4
0.2
0.0
0.0
0.5
1.0
δ = 0.3452
$δ_c$ = 0.6199
δ = 0.7737

(b)

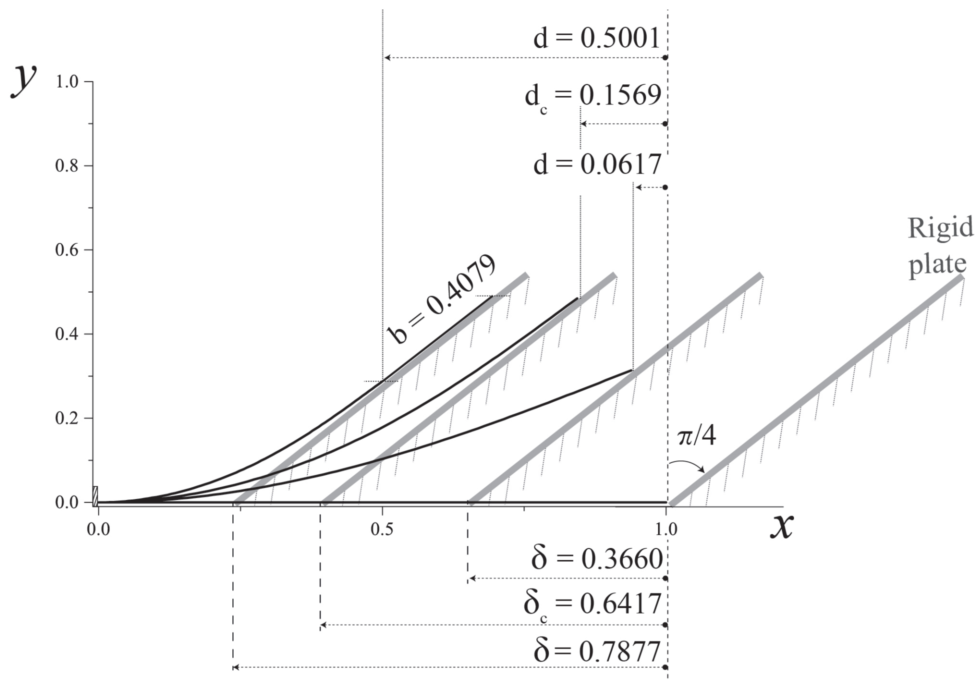
d = 0.5001
d_c = 0.1569
d = 0.0617
Rigid plate
b = 0.4079
π/4
y
x
1.0
0.8
0.6
0.4
0.2
0.0
0.0
0.5
1.0
δ = 0.3660
$δ_c$ = 0.6417
δ= 0.7877

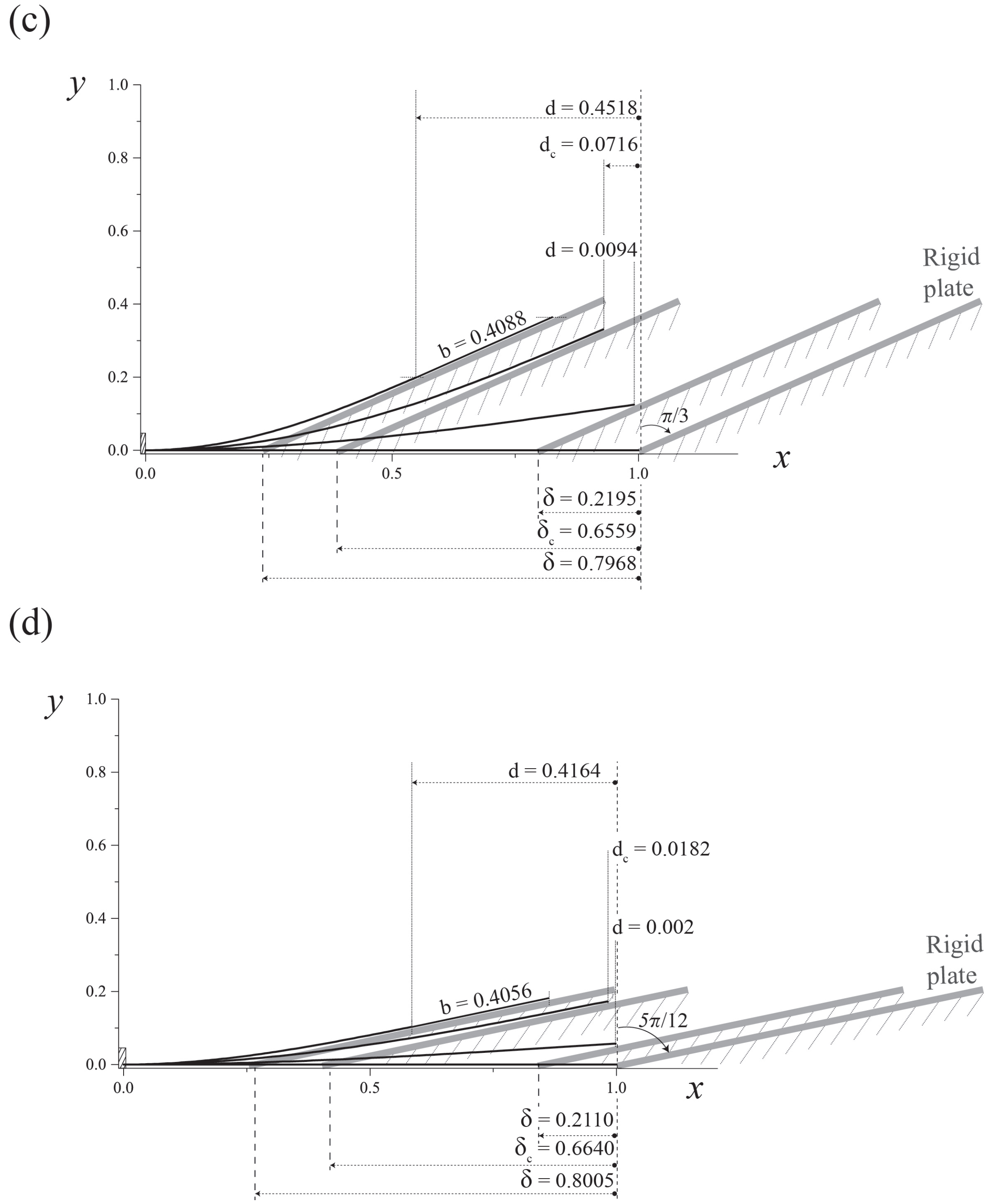

Figure 4.9: Nondimensional configurations of the rod. The surface is positioned at α, where (a) $\alpha = \frac{\pi}{6}$, (b) $\alpha = \frac{\pi}{4}$, (c) $\alpha = \frac{\pi}{3}$ and (d) $\alpha = \frac{5\pi}{12}$. Note that the values of δ_c increase with increasing values of $\alpha\forall$.

The experimental data (blue crosses) along with the theoretical loading paths (continuous line) in are depicted in Figures s 4.10−4.12. The results correspond to five different orientations of the plate. Note that the model does not account for friction and we do our best to eliminate this. For example, the surface is covered in lubricant oil before each experiment as this will lower the coefficients of static and kinetic friction. The values of both experimental and numerical f are re-scaled using Euler's critical load formula of a clamped free rod that is axially loaded, see Eq. 2.45. The red filled circle in our equilibrium paths denote δ_{crit}.

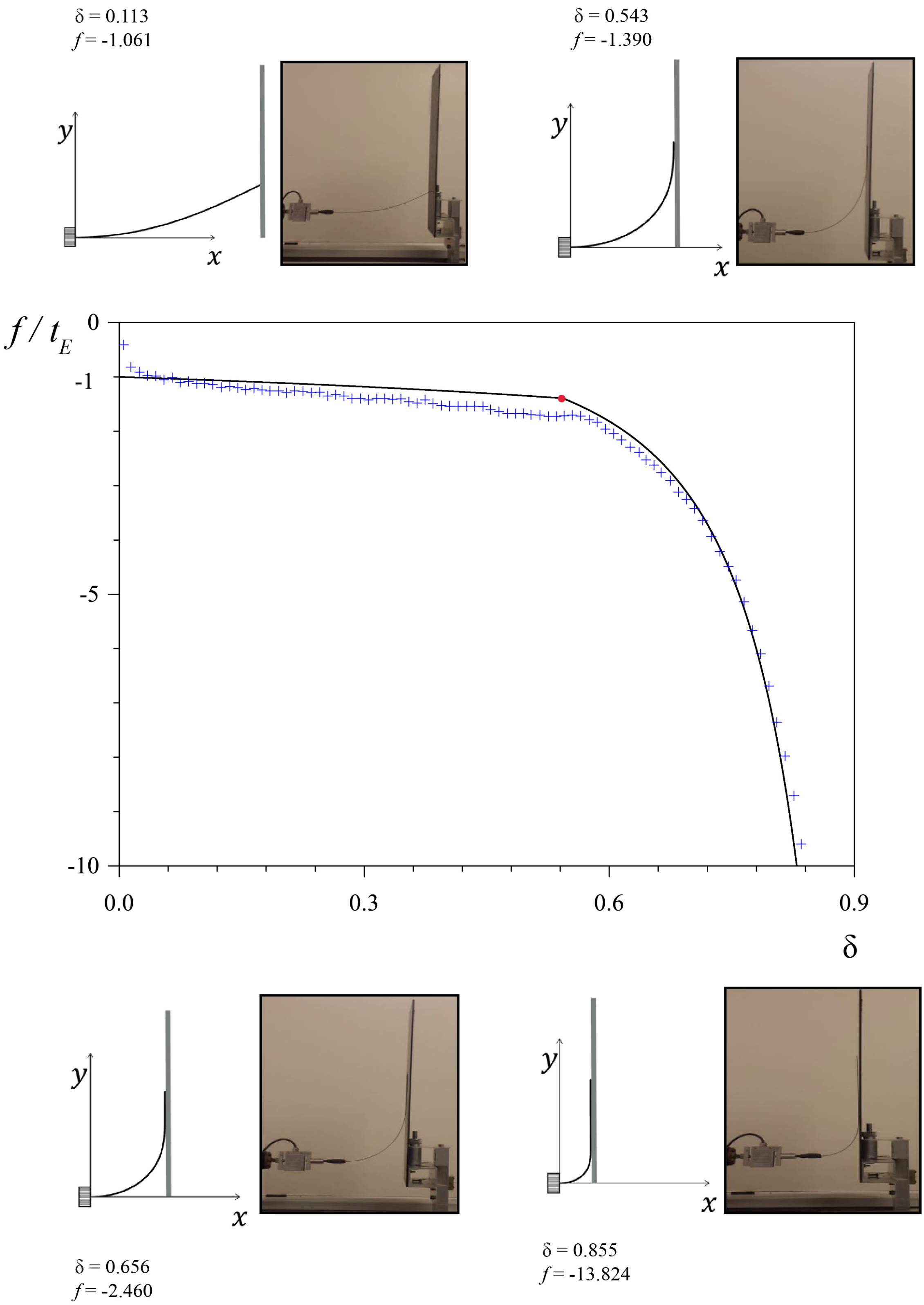

Figure 4.10: Experimental data (blue crosses) for a rod in contact with a plate that is positioned at $\alpha = 0$, i.e., an axially applied load. The theory predicts a non-dimensional primary bifurcation at $\frac{t}{t_E} = -1$, whereas the experimental loading path 'rounds' it off. The experimental data follows the theory closely for both $\delta < \delta_c$ and $\delta > \delta_c$. Note, that we force the rod to deflect into the UHP by giving the rod a slight nudge into that plane.

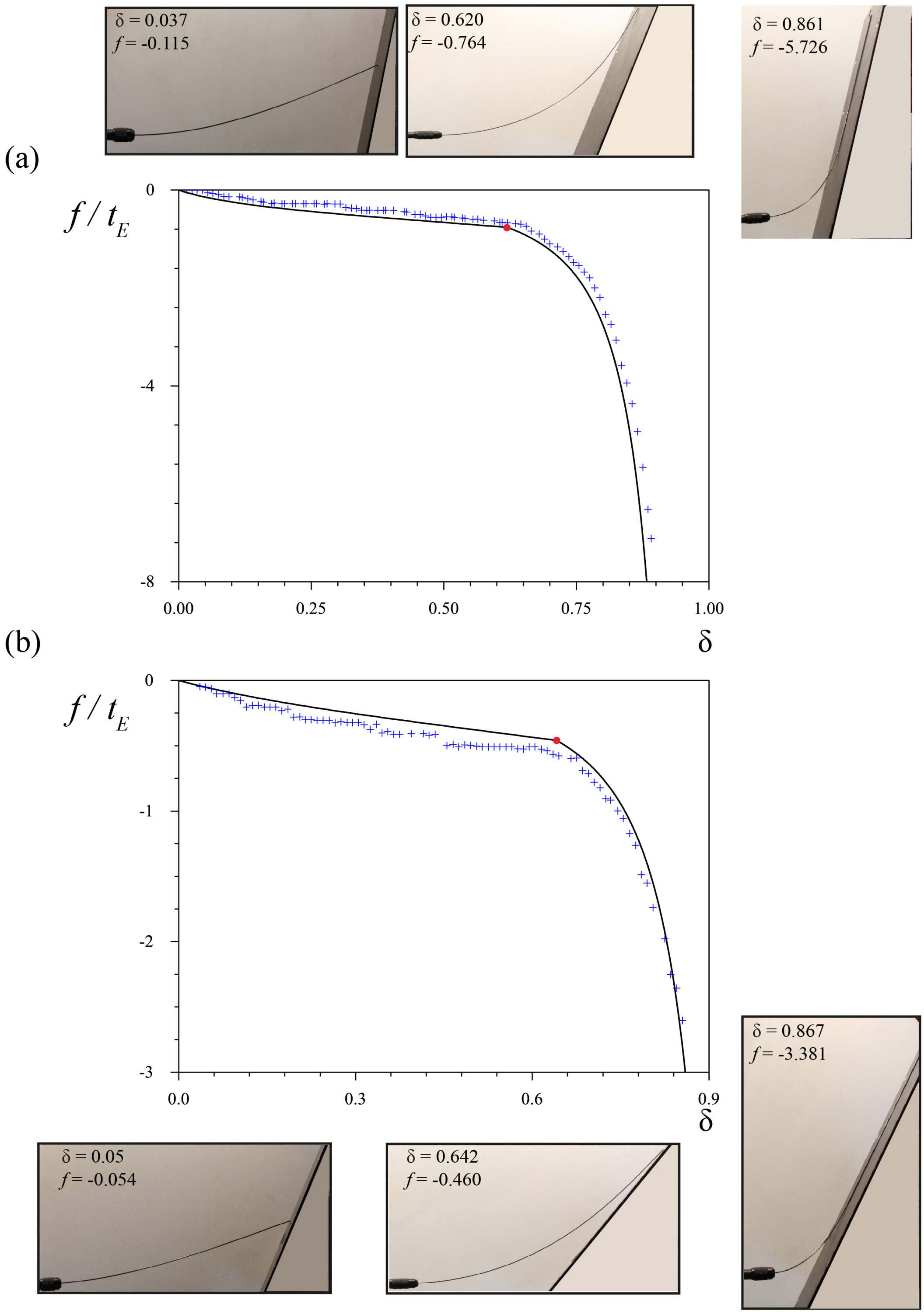

Figure 4.11: Experimental data (blue crosses) for a rod in contact with a plate that is positioned at (a) $\alpha = \frac{\pi}{6}$ and (b) $\alpha = \frac{\pi}{4}$. The experimental data follows the theoretical path closely, however there are regions where the experimental data displays "stick-slip" and this is generally more visible in pre-line contact experimental data. The appearance of "stick-slip" oscillations have been associated with grazing bifurcations, see [70, 71]

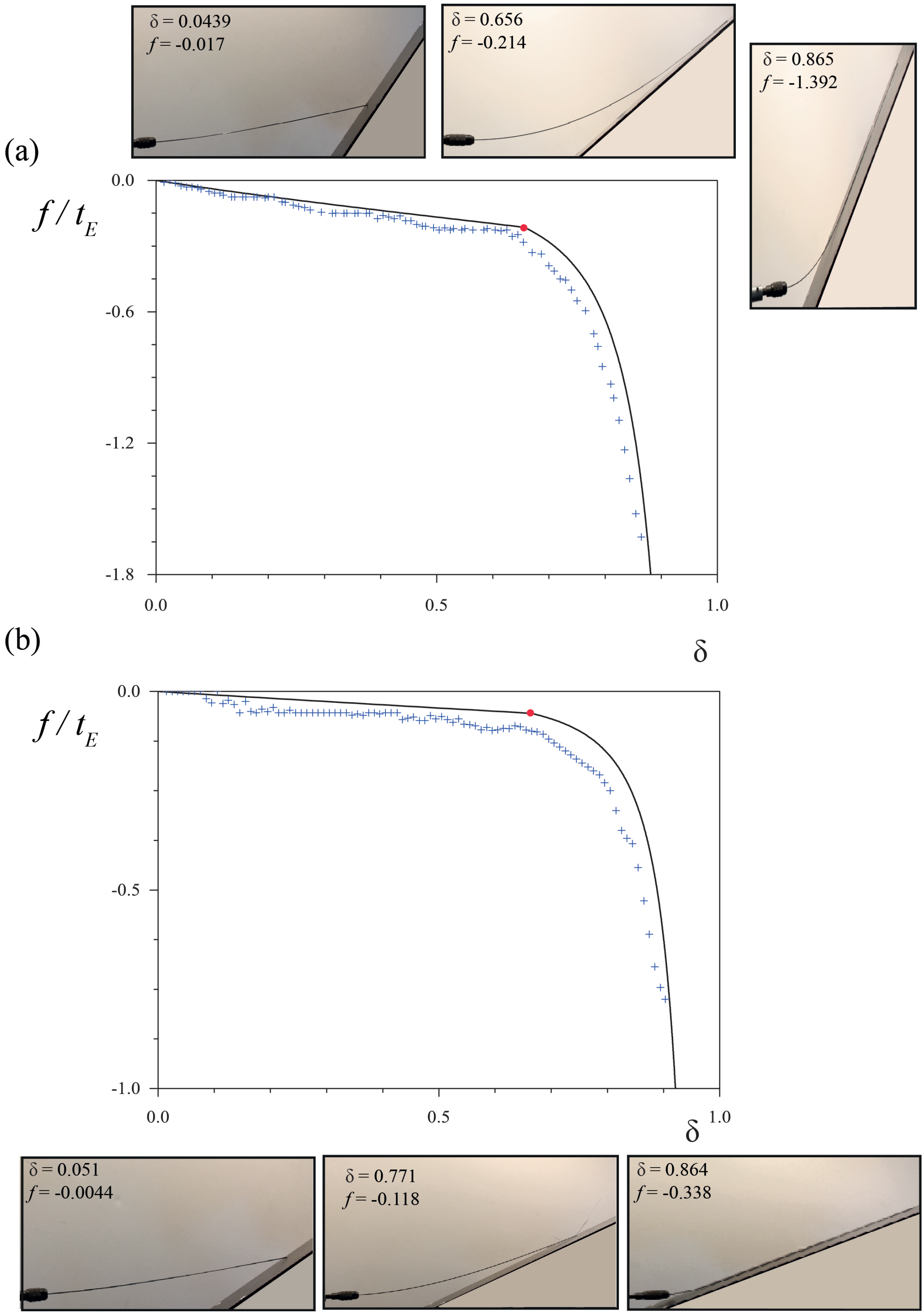

Figure 4.12: Experimental data (blue crosses) for a rod in contact with a plate that is positioned at (a) $\alpha = \frac{\pi}{3}$ and (b) $\alpha = \frac{5\pi}{12}$. Generally the experimental data is in good agreement with the theory.

4.4 Solutions for the deformed rod in contact with a rigid plate

In this section we obtain the solutions in terms of elliptic integrals. We follow the analysis published by the author of [6] and introduce the angles:

$$\beta(z) = \phi(z) + \alpha, \tag{4.10}$$

$$\beta_1 = \gamma + \alpha. \tag{4.11}$$

We introduce the angles β and β_1 which are the summation of the tangent of the rod and the inclination of the force α, at z and $z = 1$ respectively. For a graphical representation, see Figure 4.13. We now proceed in deriving explicit equations

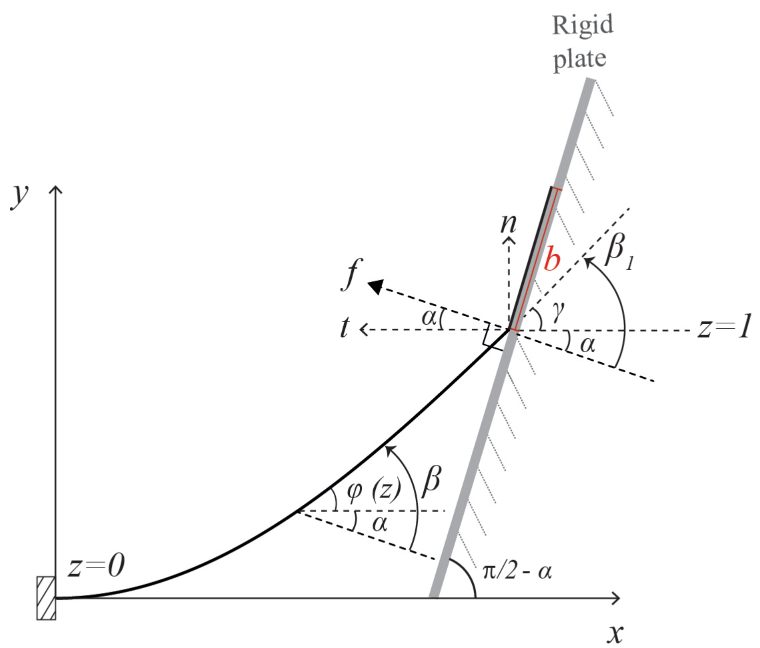

Figure 4.13: A nondimensional clamped free rod that is subjected to an inclined force, which is exerted from the plate. The point $z = 1$ represents the lift-off point and b refers to the length of rod in contact with the surface. The bold grey line corresponds to the frictionless plate, which in this case, is inclined at α radians. For values where $\alpha = 0$, the resultant force lies along the x axis and $f = -t$.

for the displacement δ and the force f. The axial and normal forces at $z = 1$ are given as follows:

$$t = -f\cos(\alpha), \tag{4.12}$$

$$n = f\sin(\alpha). \tag{4.13}$$

From Eqs. 4.7, 4.8 and 4.11 we express the following second order ODE:

$$\frac{\mathrm{d}^2\beta}{\mathrm{d}z^2} = -\lambda^2 f \sin\beta. \tag{4.14}$$

We integrate Eq. 4.14 and obtain:

$$\frac{1}{2}\left(\frac{\mathrm{d}\beta}{\mathrm{d}z}\right)^2 = \lambda^2 f\cos(\beta) + C. \tag{4.15}$$

The boundary conditions in terms of the newly defined dependent variable β are as follows:

$$\beta(0) = \alpha, \tag{4.16}$$

$$\frac{\mathrm{d}\beta}{\mathrm{d}z}(1) = 0, \tag{4.17}$$

Eq. 4.15 is written as follows:

$$\begin{aligned}\frac{\mathrm{d}\beta}{\mathrm{d}z} &= \left(2\lambda^2 f\left(\cos(\beta) - \cos(\beta_1)\right)\right)^{1/2}, \\ &= \left(4\lambda^2 f\left(\sin^2\left(\frac{\beta_1}{2}\right) - \sin^2\left(\frac{\beta}{2}\right)\right)\right)^{1/2}.\end{aligned} \tag{4.18}$$

Eq. 4.18 is integrated,

$$\int_0^z \mathrm{d}u = \frac{1}{2(f)^{1/2}\lambda}\int_\alpha^\beta \frac{\mathrm{d}\psi}{\left(\sin^2\left(\frac{\beta_1}{2}\right) - \sin^2\left(\frac{\psi}{2}\right)\right)^{1/2}}. \tag{4.19}$$

We introduce p and θ which are defined as:

$$p = \sin\left(\frac{\beta_1}{2}\right), \qquad \sin\left(\frac{\psi}{2}\right) = p\ \sin(\theta), \qquad \theta_A \le \theta \le \theta_B. \tag{4.20}$$

We differentiate the second expression of Eq. 4.20 and re-write Eq. 4.19 as follows:

$$z = \frac{1}{(f)^{1/2}\lambda} \int_{\theta_A}^{\theta_B} \frac{d\theta}{\left(1 - p^2 \sin^2(\theta)\right)^{1/2}}, \tag{4.21}$$

where θ_A and θ_B are defined as follows:

$$\theta_A = \arcsin\left(\frac{\sin\left(\frac{\alpha}{2}\right)}{p}\right), \tag{4.22}$$

$$\theta_B = \arcsin\left(\frac{\sin\left(\frac{\beta}{2}\right)}{p}\right). \tag{4.23}$$

Eq. 4.21 is split:

$$\begin{aligned} z &= \frac{1}{f^{1/2}\lambda} \int_0^{\theta_B} \frac{d\theta}{\left(1 - p^2 \sin^2(\theta)\right)^{1/2}} - \frac{1}{f^{1/2}\lambda} \int_0^{\theta_A} \frac{d\theta}{\left(1 - p^2 \sin^2(\theta)\right)^{1/2}} \\ &= \frac{1}{f^{1/2}\lambda} \left(F\left(\theta_B, p^2\right) - F\left(\theta_A, p^2\right)\right) \end{aligned} \tag{4.24}$$

The total length of the rod is be obtained by setting $z = 1$, $\beta = \beta_1$. It follows that $\theta_B = \pi/2$, and consequently, Eq. 4.24 becomes:

$$1 = \frac{1}{f^{1/2}\lambda} \left(K\left(p^2\right) - F(\theta_A, p^2)\right), \tag{4.25}$$

where K and F are complete and incomplete elliptic integrals of the first kind and second kind respectively. The forces t and n, axial and normal respectively, are recovered from the following equations:

$$\begin{aligned} t &= -f\cos\alpha, \\ &= -\frac{1}{\lambda^2}\left(K\left(p^2\right) - F\left(\theta_A, p^2\right)\right)^2 \sin(\alpha), \end{aligned} \tag{4.26}$$

$$\begin{aligned} n &= f\sin\alpha, \\ &= \frac{1}{\lambda^2}\left(K\left(p^2\right) - F\left(\theta_A, p^2\right)\right)^2 \sin(\alpha). \end{aligned} \tag{4.27}$$

For given values of α, p and b, Eq. 4.26 is used to determine the force t.

The shape of the deformed rod is obtained from Eqns. 4.5 and 4.6,

$$x(z) = \lambda \int_0^z \mathrm{d}u \cos(\beta - \alpha)\,, \tag{4.28}$$

$$y(z) = \lambda \int_0^z \mathrm{d}u \sin(\beta - \alpha)\,, \tag{4.29}$$

where,

$$\cos(\phi) = \cos(\beta - \alpha) = \cos(\beta)\cos(\alpha) + \sin(\alpha)\sin(\beta), \tag{4.30}$$

$$\sin(\phi) = \sin(\beta - \alpha) = \sin(\beta)\cos(\alpha) - \cos(\beta)\sin(\alpha), \tag{4.31}$$

and the coordinates $x(z)$ and $y(z)$ can be determined as follows:

$$\begin{aligned} x(z) &= \frac{\cos(\alpha)}{f^{1/2}} \int_{\theta_A}^{\theta_B} \left(2\left(1 - p^2 \sin^2(\theta)\right)^{1/2} - \frac{1}{\left(1 - p^2 \sin^2(\theta)\right)} \right) \mathrm{d}\theta \\ &+ \frac{2p\sin((\alpha)}{f^{1/2}} \int_{\theta_A}^{\theta_B} \sin(\theta)\,. \end{aligned} \tag{4.32}$$

$$\begin{aligned} x(z) &= \frac{\cos(\alpha)}{(f)^{1/2}} \Big(2E(\theta_B, p) - 2E(\theta_A, p) - F(\theta_B, p) + F(\theta_A, p) \Big) \\ &+ \frac{2p\sin(\alpha)}{f^{1/2}} \left(\cos(\theta_A) - \cos(\theta_B)\right). \end{aligned} \tag{4.33}$$

$$\begin{aligned} y(z) &= \frac{2p\cos(\alpha)}{f^{1/2}} \int_{\theta_A}^{\theta_B} \sin(\theta)\,\mathrm{d}\theta - \frac{\sin(\alpha)}{f^{1/2}} \int_{\theta_A}^{\theta_B} 2\left(1 - p^2\sin^2(\theta)\right)^{1/2} \mathrm{d}\theta \\ &+ \frac{2p\sin(\alpha)}{f^{1/2}} \int_{\theta_A}^{\theta_B} \frac{\mathrm{d}\theta}{\left(1 - p^2\sin^2(\theta)\right)^{1/2}}, \end{aligned} \tag{4.34}$$

$$\begin{aligned} y(z) &= \frac{2p\cos(\alpha)}{f^{1/2}} \left(\cos(\theta_A) - \cos(\theta_B)\right) - \frac{\sin(\alpha)}{f^{1/2}} \big(2E(\theta_B, p) - 2E(\theta_A, p) - F(\theta_B, p) + \\ &+ F(\theta_A, p) \big). \end{aligned} \tag{4.35}$$

The coordinates at $z = 1$ are attained by setting $\theta_B = \pi/2$, as follows:

$$x(1) = \frac{\cos(\alpha)}{f^{1/2}} \Big(2E(p) - 2E(\theta_A, p) - K(p) + F(\theta_A, p) \Big) + \frac{2p\sin(\alpha)\cos(\theta_A)}{f^{1/2}} \tag{4.36}$$

$$y(1) = \frac{2p\cos(\alpha)\cos(\theta_A)}{f^{1/2}} - \frac{\sin(\alpha)}{f^{1/2}} \Big(2E(p) - 2E(\theta_A, p) - K(p) + F(\theta_A, p). \Big) \tag{4.37}$$

The computation of δ involves $y(1)$ and $x(1)$ (see Eqs. 4.2 and 4.3). The force, t and displacement δ_c are computed using elliptic integrals and compared with the numerics, see Table 4.1.

	AUTO		**Elliptic integral**	
α	δ_c	t_c	δ_c	t_c
$89\pi/180$	0.666650	-0.0024702	0.666650	-0.0024702
$5\pi/12$	0.664038	-0.055049	0.664038	-0.055049
$\pi/3$	0.655937	-0.214173	0.655937	-0.214173
$\pi/4$	0.641672	-0.459711	0.641672	-0.459711
$\pi/6$	0.619918	-0.763555	0.619918	-0.763555
0	0.543053	-1.393204	0.543053	-1.393204

Table 4.1: Values of t and δ at the transition point. The resultant load acts at $s = 1$ and $s = 1 - b$ for pre and post line contact solutions respectively. As $\alpha \to \pi/2$, the location of δ_c increases and the magnitude of the axial load approaches zero. We present both the analytical (elliptic integral) and the numerical results (AUTO) and it can be seen that the error is zero.

4.5 Discussion and conclusion

We have shown both the experimental and the theoretical equilibrium shapes and loading diagrams of rod which is deformed as a flat, frictionless, rigid plate is pressed onto the free end. The experimental data points, represented by the blue crosses in Figures 4.10-4.12, follow the theoretical loading paths, represented by the continuous black line in Figures 4.10-4.12 closely. One of the challenges in conducting such experiments is to eliminate the experimental error and achieve closer agreement between the experimental and theoretical results. Inevitably, the experiments (the procedure and instruments), carry unavoidable imperfections. One significant problem which is not reflected in the mathematical model, is the presence of friction. Whilst measures were taken to reduce friction, close inspection of the experimental data reveals stick-slip phenomena. This is more evident for $\delta < \delta_c$, i.e., when the tip of the rod is in point contact with the plate. For $\delta > \delta_c$, when line contact is inaugurated, the rod slides up the surface and the coefficient of friction between the surfaces is kinetic, rather than static. Studies by [72] suggest that friction assists rats in gathering information on surface textures. The steep gradient displayed in the td plots for $\delta > \delta_c$ suggests that the distinction between point and line contact may play a significant role in how animals use whiskers to gather information about their surroundings. Owing to unavailability of rats and appropriate facilities for conducting experiments on whiskers, the experimentation in this study is restricted to nickel-titanium rods. However, reports of experiments on whiskers are given in [15] and [73]. Overall, the good qualitative and quantitative correlation between the data obtained from our experiments with that predicted by the theory shows that the elastica provides a close description of the mechanics of a bent nickel-titanium rod. Of course these engineered rods, unlike biological rods, are manufactured under controlled specifications and closely approximate the assumptions of isotropy, homogeneity and zero initial curvature. However, in the case of real-world biological rods, such as whiskers, those assumptions are no longer valid. Whiskers are generically not only anisotropic, they also have weight, and many whiskers have initial curvature. For example, inspection of the experimental data in Figure 4.10 suggests that no bifurcation occurs for the case $\alpha = 0$. That mismatch can be attributed to both the sagging effect of the rod's weight, which is not included in the mathematical model, and the fact that even a tiny misalignment of the end load causes a correspondingly small deflection. Those can be considered small imperfections and consequently the experimental loading path shows a generic rounding off of the primary bifurcation predicted by the theory. We determine the Eqs. of t, n, f and δ in §4.4 and compare those with results obtained from AUTO, see Table 4.1 where we give the critical values for different values of α.

The work presented here unifies the mechanics of point contact with line contact and additionally covers a wide range of inclinations of the applied load, from the vertical to the horizontal. We also quantify the mechanics in the hope that we shed some light on what information is transduced down to the mechanoreceptors.

Chapter 5

Concluding remarks

This thesis examines loop formation, jump phenomena and contact problems in clamped-free rods that are deformed under rigid and dead loading. The platform for our studies has been *td* (force versus end displacement) loading diagrams and deformed shapes. We have approached the problem from three perspectives: experimental, numerical and analytical.

The mathematical model set out in Chapter 2 is written to reflect the experimental set up as closely as possible. We identified weight and friction as the main source of discrepancy between experimental data and the theory. The mathematical model could have been written to incorporate rods self-weight, see for example [4]. The equations for the heavy rod (a rod with weight) are non-integrable, see [74], and in our work we focus on integrable cases. The effect of friction was difficult to eliminate. In chapter 3 we conduct experiments on uniformly curved rods that are deformed under rigid loading. We identify friction between the slider and the rail, and at the pinned-joint. Also, in our experiments on clamped-free rods that are deformed as a rigid plate is pressed at the tip there is unavoidable friction during contact between the rod and the plate. Although measures were taken to reduce this $-$ for example the surface was fully lubricated before any experiments, we found that it could not be completely eliminated.

In the same way that there exist two solutions (symmetric solutions) in the case of an initially straight rod, there exist two solutions for the uniformly curved rod. In the case of a straight rod those two solutions are symmetric i.e., taking either the positive or negative sign of the curvature equation, yields solutions that lie in the UHP and LHP respectively. In the case of uniformly curved rods that symmetry is lost. We find interior inflection points for rods that are located in the LHP, however there are no interior inflection points for deformed rods that lie in the UHP.

Investigations of large deflections led us to focus on how loops form, both under tension and compression. It is evident from our experiments that loops can form from minimal out-of-plane deformation i.e, a deformation of the thickness of the rod itself. To date, most research appertaining to loop formation in rods are from a 3-d perspective, [4]. This thesis demonstrates very good agreement between the experimental data for loop formation and the 2-d planar elastica. The 2-d model has the advantage of being relatively simpler than its 3-d counterpart and facilitates analytical results that are reasonably straightforward.

Experimental and numerical results indicate that deformed shapes situated in the LHP always have interior inflection points. Experimentally we were not able to follow the loading path (td) as predicted by the theory. Under the dead loading procedure, the rod became unstable at certain critical loads, which correspond to local maxima in td. Those critical points are identified by solving pertinent equations (see §3.4.1). To our knowledge, those results have not been published elsewhere. We propose, for future study, the effect of changing the loading procedure for the study of uniformly curved rods that are located in the LHP, i.e., conduct experiments on rods in the LHP that are deformed under rigid loading. In that way we should be able to obtain experimental data that corresponds to a wider domain of the *td* path, as set out by the theory. We also propose the study of uniformly curved rods in the LHP for higher values of uniform curvature. Owing to stability, the experiments we conducted examined certain values of curvature. Owing to instability issues, the experiments we report on here were restricted to certain values of curvature.

In chapter 5 we present the experimental results of a rod whose ends are clamped-free, with a rigid plate pressed at the free end. The numerics and analysis indicate that a bifurcation occurs for the case when the plate is positioned perpendicular to the length of the rod, i.e., $\alpha = 0$. Experimentally, the effect of weight and friction show a "rounding" of the primary bifurcation for this set-up. With respect to the equilibrium loading diagrams, we provide a comprehensive description of point and line contact for large deformations. This work opens up new avenues for investigation. For example, uniformly (or non-uniformly) curved rods in contact with a flat, rigid surface. This is important in the study of whisker modelling [19], [75].

Every effort has been made to try and ensure that the experimental specifications and procedures are as close to the boundary conditions and loading sequences as possible. The analytical solutions provide a benchmark for the numerical (which is approximate) and the experimental data. However, the analytical solutions are not directly expressed in terms of $t(d)$ or $y(x)$, which are our main forums for displaying and studying results, though we can plot xy and td using the solutions for $x(s)$, $y(s)$, $t(s)$, $\phi(s)$ etc. Also, neither the analytical solutions nor the numerics predict the instabilities that are observed during an experiment. Nevertheless, the critical points at which those instabilities occur can be detected by analysis (they are local maxima on td curve). Whilst, in general, analysis leads to classifications of inflectional and non-inflectional elastica, in the case of intrinsic curvature a difficultly arises in clearly demarcating those types, a difficulty which is reflected in the sensitivity of the elliptic modulus, as depicted in Figure 2.11. Indeed, it is difficult to tell from inspection of the shape of the rod (in the UHP) whether or not it is part of an inflectional or non-inflectional solution. In the case of the LHP, all solutions include an interior inflection point. The combination of the three methodologies that we have adopted has helped in identifying and gaining a better insight intrinsically, uniformly curved rods.

Bibliography

[1] S. S. Antman, *Nonlinear problems of elasticity.* New York NY: Springer Verlag, 1995.

[2] R. Levien, "The elastica: a mathematical history," University of California, Berkeley, Tech. Rep., 2008.

[3] C. Truesdell, "The rational mechanics of flexible or elastic bodies: 1638-1788," *Leonhardi Euleri Opera Omnia, Ser. 2*, 1960.

[4] V. G. A. Goss, "Snap buckling, writhing and loop formation in twisted rods," Ph.D. dissertation, University of London, 2003.

[5] S. P. Timoshenko and J. M. Gere, *Theory of elastic stability.* Courier Corporation, 2009.

[6] R. Frisch-Fay, *Flexible bars.* Butterworths, 1962.

[7] L. Euler, *Methodus inveniendi lineas curvas maximi minimive proprietate gaudentes.* Appendix: De curvis elasticis. Lausanne and Geneva., 1744.

[8] J. M. T. Thompson, "Stability of elastic structures and their loading devices," *Journal of Mechanical Engineering Science*, vol. 3, no. 2, pp. 153–162, 1961.

[9] A. E. H. Love, *A treatise on the mathematical theory of elasticity*. Cambridge University Press, 2013.

[10] W. Snowdon, "The bending of a thin rod having initially uniform curvature," *International Journal of Mechanical Sciences*, vol. 5, no. 3, pp. 213–221, 1963.

[11] H. D. Conway, "The nonlinear bending of thin circular rods," *Journal of Applied Mechanics*, vol. 23, pp. 7–10, 1956.

[12] W. Fichter and M. W. Pinson, "Load-shortening behavior of an initially curved eccentrically loaded columne," *NASA Technical Memorandum*, vol. 42, pp. 1–21, 1989.

[13] C. González and J. LLorca, "Stiffness of a curved beam subjected to axial load and large displacements," *International Journal of Solids and Structures*, vol. 42, no. 5-6, pp. 1537–1545, 2005.

[14] B. W. Quist and M. J. Hartmann, "Mechanical signals at the base of a rat vibrissa: the effect of intrinsic vibrissa curvature and implications for tactile exploration," *Journal of Neurophysiology*, vol. 107, no. 9, pp. 2298–2312, 2012.

[15] J. H. Solomon and M. J. Hartmann, "Extracting object contours with the sweep of a robotic whisker using torque information," *The International Journal of Robotics Research*, vol. 29, no. 9, pp. 1233–1245, 2010.

[16] R. B. Towal, B. W. Quist, V. Gopal, J. H. Solomon, and M. J. Hartmann, "The morphology of the rat vibrissal array: a model for quantifying spa-

tiotemporal patterns of whisker-object contact," *PLoS Computational Biology*, vol. 7, no. 4, p. e1001120, 2011.

[17] M. A. Neimark, M. L. Andermann, J. J. Hopfield, and C. I. Moore, "Vibrissa resonance as a transduction mechanism for tactile encoding," *Journal of Neuroscience*, vol. 23, no. 16, pp. 6499–6509, 2003.

[18] W. Yan, Q. Kan, K. Kergrene, G. Kang, X.-Q. Feng, and R. Rajan, "A truncated conical beam model for analysis of the vibration of rat whiskers," *Journal of Biomechanics*, vol. 46, no. 12, pp. 1987–1995, 2013.

[19] Y. Boubenec, D. E. Shulz, and G. Debrégeas, "Whisker encoding of mechanical events during active tactile exploration," *Frontiers in Behavioral Neuroscience*, vol. 6, p. 74, 2012.

[20] V. Goss, P. Singh, and R. Chaouki, "Large deflections of a clamped-slider-pinned rod with uniform intrinsic curvature," *International Journal of Solids and Structures*, vol. 129, pp. 135–145, 2017.

[21] V. Goss and R. Chaouki, "Loading paths for an elastic rod in contact with a flat inclined surface," *International Journal of Solids and Structures*, vol. 88, pp. 274–282, 2016.

[22] K. Bisshopp and D. Drucker, "Large deflection of cantilever beams," *Quarterly of Applied Mathematics*, vol. 3, no. 3, pp. 272–275, 1945.

[23] R. H. Plaut, S. Suherman, D. A. Dillard, B. E. Williams, and L. T. Watson, "Deflections and buckling of a bent elastica in contact with a flat surface,"

International Journal of Solids and Structures, vol. 36, no. 8, pp. 1209–1229, 1999.

[24] A. K. Nallathambi, C. L. Rao, and S. M. Srinivasan, "Large deflection of constant curvature cantilever beam under follower load," *International Journal of Mechanical Sciences*, vol. 52, no. 3, pp. 440–445, 2010.

[25] M. Born, "Stabilitat der elastischen linie in ebene und raum," Ph.D. dissertation, 1906.

[26] G. Van der Heijden, S. Neukirch, V. Goss, and J. Thompson, "Instability and self-contact phenomena in the writhing of clamped rods," *International Journal of Mechanical Sciences*, vol. 45, no. 1, pp. 161–196, 2003.

[27] C. Wang, "Post-buckling of a clamped-simply supported elastica," *International Journal of Non-Linear Mechanics*, vol. 32, no. 6, pp. 1115–1122, 1997.

[28] M. Mahtabi, N. Shamsaei, and M. Mitchell, "Fatigue of nitinol: the state-of-the-art and ongoing challenges," *Journal of the Mechanical Behavior of Biomedical Materials*, vol. 50, pp. 228–254, 2015.

[29] T. Duerig, A. Pelton, and D. Stöckel, "An overview of nitinol medical applications," *Materials Science and Engineering: A*, vol. 273, pp. 149–160, 1999.

[30] M. d. A. Ferreira, M. A. Luersen, and P. C. Borges, "Nickel-titanium alloys: A systematic review," *Dental Press Journal of Orthodontics*, vol. 17, no. 3, pp. 71–82, 2012.

[31] J. Gere and S. Timoshenko, *Mechanics of materials PWS.* KENT Publishing Company, Elsevier Science BV, Amsterdam, 1990.

[32] E. J. Hearn, *Mechanics of Materials 2: The mechanics of elastic and plastic deformation of solids and structural materials.* Elsevier, 1997.

[33] A. Walker and D. Hall, "An analysis of the large deflections of beams using the rayleigh-ritz finite element method," *The Aeronautical Quarterly*, vol. 19, no. 4, pp. 357–367, 1968.

[34] Y. Tada and G. C. Lee, "Finite element solution to an elastica problem of beams," *International Journal for Numerical Methods in Engineering*, vol. 2, no. 2, pp. 229–241, 1970.

[35] M. Dado and S. Al-Sadder, "A new technique for large deflection analysis of non-prismatic cantilever beams," *Mechanics Research Communications*, vol. 32, no. 6, pp. 692–703, 2005.

[36] E. Riks, "An incremental approach to the solution of snapping and buckling problems," *International journal of solids and structures*, vol. 15, no. 7, pp. 529–551, 1979.

[37] E. J. Doedel and B. E. Oldeman, "Auto-07p: continuation and bifurcation software for ordinary differential equations, Concordia University, Montreal, Canada," 2011.

[38] W. Govaerts, "Numerical bifurcation analysis for odes," *Journal of Computational and Applied Mathematics*, vol. 125, no. 1-2, pp. 57–68, 2000.

[39] H. B. Keller, "Numerical solution of bifurcation and nonlinear eigenvalue problems," *Application of Bifurcation Theory*, pp. 359–384, 1977.

[40] K. Ward, F. Bertails, T.-Y. Kim, S. R. Marschner, M.-P. Cani, and M. C. Lin, "A survey on hair modeling: Styling, simulation, and rendering," *IEEE Transactions on Visualization and Computer Graphics*, vol. 13, no. 2, pp. 213–234, 2007.

[41] F. A. Lucianna, A. L. Albarracín, S. M. Vrech, F. D. Farfán, and C. J. Felice, "The mathematical whisker: A review of numerical models of the rat's vibrissa biomechanics," *Journal of Biomechanics*, vol. 49, no. 10, pp. 2007–2014, 2016.

[42] A. Lazarus, J. T. Miller, M. M. Metlitz, and P. M. Reis, "Contorting a heavy and naturally curved elastic rod," *Soft Matter*, vol. 9, no. 34, pp. 8274–8281, 2013.

[43] J. Coyne, "Analysis of the formation and elimination of loops in twisted cable," *IEEE Journal of Oceanic Engineering*, vol. 15, no. 2, pp. 72–83, 1990.

[44] D. Stöckel, "Nitinol—a material with unusual properties," *Endovascular Update*, vol. 1, no. 1, pp. 1–8, 1998.

[45] F. C. Liu, "Kink formation and rotational response of single and multistrand electromechanical cables." Tech. Rep., 1975.

[46] T. Yabuta, "Submarine cable kink analysis," *Bulletin of JSME*, vol. 27, no. 231, pp. 1821–1828, 1984.

[47] E. Zajac, "Stability of two planar loop elasticas," *Journal of Applied Mechanics*, vol. 29, no. 1, pp. 136–142, 1962.

[48] F. Rosenthal, "The application of greenhill's formula to cable hockling," *Journal of Applied Mechanics*, vol. 43, no. 4, pp. 681–683, 1976.

[49] P. Singh and V. Goss, "Critical points of the clamped–pinned elastica," *Acta Mechanica*, vol. 229, no. 12, pp. 4753–4770, 2018.

[50] I. S. Gradshteyn and I. M. Ryzhik, *Table of integrals, series, and products.* Academic press, 2014.

[51] S. Navaee and R. Elling, "Equilibrium configurations of cantilever beams subjected to inclined end loads," *Journal of Applied Mechanics*, vol. 59, no. 3, pp. 572–579, 1992.

[52] L. Saalschütz, *Der belastete Stab unter Einwirkung einer seitlichen Kraft: Auf Grundlage des strengen Ausdrucks für den Krümmungsradius...* Teubner, 1880.

[53] M. Batista, "Analytical treatment of equilibrium configurations of cantilever under terminal loads using jacobi elliptical functions," *International Journal of Solids and Structures*, vol. 51, no. 13, pp. 2308–2326, 2014.

[54] J. H. Lau, "Large deflections of beams with combined loads," *Journal of the Engineering Mechanics Division*, vol. 108, no. 1, pp. 180–185, 1982.

[55] M. Mutyalarao, D. Bharathi, and B. N. Rao, "Large deflections of a cantilever beam under an inclined end load," *Applied Mathematics and Computation*, vol. 217, no. 7, pp. 3607–3613, 2010.

[56] G. Domokos, P. Holmes, and B. Royce, “Constrained euler buckling,” in *Mechanics: From Theory to Computation*. Springer, 2000, pp. 413–446.

[57] J.-S. Chen and S.-Y. Hung, “Deformation and stability of an elastica constrained by curved surfaces,” *International Journal of Mechanical Sciences*, vol. 82, pp. 1–12, 2014.

[58] S. Rienstra, “Analytical approximations for offshore pipelaying problems,” in *Proceedings of the First International Conference on Industrial and Applied Mathematics ICIAM*, vol. 87, 1987, pp. 99–108.

[59] G. W. Hunt and A. Blackmore, “Homoclinic and heteroclinic solutions of upheaval buckling,” in *Localization And Solitary Waves In Solid Mechanics*. World Scientific, 1999, pp. 321–331.

[60] A. Palmer, J. Baldry *et al.*, “Lateral buckling of axially constrained pipelines,” *Journal of Petroleum Technology*, vol. 26, no. 11, pp. 1–283, 1974.

[61] R. Hobbs, “Pipeline buckling caused by axial loads,” *Journal of Constructional Steel Research*, vol. 1, no. 2, pp. 2–10, 1981.

[62] I. Somervaille, “Quadrature matrices and elastica problems,” *Computer methods in applied mechanics and engineering*, vol. 69, no. 3, pp. 345–354, 1988.

[63] G. Domokos, W. Fraser, and I. Szeberényi, “Symmetry-breaking bifurcations of the uplifted elastic strip,” *Physica D: Nonlinear Phenomena*, vol. 185, no. 2, pp. 67–77, 2003.

[64] G. R. Scholz and C. D. Rahn, "Profile sensing with an actuated whisker," *IEEE Transactions on Robotics and Automation*, vol. 20, no. 1, pp. 124–127, 2004.

[65] T. N. Clements and C. D. Rahn, "Three-dimensional contact imaging with an actuated whisker," *IEEE Transactions on Robotics*, vol. 22, no. 4, pp. 844–848, 2006.

[66] J. H. Solomon and M. J. Hartmann, "Biomechanics: robotic whiskers used to sense features," *Nature*, vol. 443, no. 7111, p. 525, 2006.

[67] B. Mitchinson and T. J. Prescott, "Whisker movements reveal spatial attention: a unified computational model of active sensing control in the rat," *PLoS Computational Biology*, vol. 9, no. 9, p. e1003236, 2013.

[68] J. A. Birdwell, J. H. Solomon, M. Thajchayapong, M. A. Taylor, M. Cheely, R. B. Towal, J. Conradt, and M. J. Hartmann, "Biomechanical models for radial distance determination by the rat vibrissal system," *Journal of Neurophysiology*, vol. 98, no. 4, pp. 2439–2455, 2007.

[69] G. Dehnhardt, "Tactile size discrimination by a california sea lion (zalophus californianus) using its mystacial vibrissae," *Journal of Comparative Physiology A*, vol. 175, no. 6, pp. 791–800, 1994.

[70] H. Dankowicz and A. B. Nordmark, "On the origin and bifurcations of stick-slip oscillations," *Physica D: Nonlinear Phenomena*, vol. 136, no. 3-4, pp. 280–302, 2000.

[71] M. Di Bernardo, C. Budd, and A. Champneys, "Normal form maps for grazing bifurcations in n-dimensional piecewise-smooth dynamical systems," *Physica D: Nonlinear Phenomena*, vol. 160, no. 3-4, pp. 222–254, 2001.

[72] A. E. Schultz, J. H. Solomon, M. A. Peshkin, and M. J. Hartmann, "Multi-functional whisker arrays for distance detection, terrain mapping, and object feature extraction," in *Robotics and Automation, 2005. ICRA 2005. Proceedings of the 2005 IEEE International Conference on.* IEEE, 2005, pp. 2588–2593.

[73] S. A. Hires, L. Pammer, K. Svoboda, and D. Golomb, "Tapered whiskers are required for active tactile sensation," *Elife*, vol. 2, p. e01350, 2013.

[74] C. Wang, "A critical review of the heavy elastica," *International Journal of Mechanical Sciences*, vol. 28, no. 8, pp. 549–559, 1986.

[75] M. J. Hartmann, "Active sensing capabilities of the rat whisker system," *Autonomous Robots*, vol. 11, no. 3, pp. 249–254, 2001.